ANALYSIS OF MEASUREMENTS FOR SOLID STATE LIDAR DEVELOPMENT

CONTRACT No. NAS8-38609

Delivery Order No. 118

Contract Period:
August 8, 1994 - December 7, 1995

Submitted To:

NASA/MSFC
Marshall Space Flight Center, AL 35812

Prepared By:
Farzin Amzajerdian
Center For Applied Optics
University Of Alabama In Huntsville
Huntsville, Al 35899
(205) 890-6030 ext. 452

August 13, 1996

FOREWORD

This report describes the work performed under NASA contract NAS8-38609, Delivery Order number 118, over the period of August 8, 1994 through December 7, 1995.

ACKNOWLEDGMENTS

The author wishes to acknowledge Drs. Anees Ahmad, Chen Feng and Mr. Ye Li for significantly contributing to this work by designing and analyzing the lidar optical subsystem. The other members of the University of Alabama Center for Applied Optics who have contributed to this work are Lamar Hawkins and Jeffrey T. Meier.

CONTENTS

1.0 INTRODUCTION

Over past few years, considerable advances have been made in the areas of the diode-pumped, eye-safe, solid state lasers and room temperature, wide bandwidth, semiconductor detectors operating in the near-infrared region. These advances have created new possibilities for the development of reliable and compact coherent lidar systems for a wide range of applications. This research effort is aimed at further developing solid state coherent lidar technology for remote sensing of atmospheric processes such as wind, turbulence and aerosol concentration.

The work performed by the UAH personnel under this Delivery Order concentrated on design and analyses of laboratory experiments and measurements, and development of advanced lidar optical subsystem and receiver technologies in support of solid state laser radar remote sensing systems which are to be designed, deployed, and used to measure atmospheric processes and constituents. UAH personnel developed a Detector Characterization Facility at NASA/MSFC and established a series of measurement procedures for characterizing candidate detectors suitable for 2-micron solid state lidar systems. Then a wideband 2-micron detector was fully characterized using the Detector Characterization Facility. A set of analytical formulations for accurately determining this optimum design parameters of heterodyne receivers were derived and then used to specify the design of a 2-micron heterodyne receiver and analyze its performance. UAH personnel also performed a thorough investigation on a number of advanced technologies for the development of low-mass and compact telescopes, scanners, lag angle compensators and signal beam de-rotators. A novel lidar telescope and a monolithic signal beam de-rotator were then designed and their fabrication and alignment tolerances were specified. A preliminary study was performed to determine the feasibility of using holographic and diffractive optical elements as a lightweight alternative to the optical wedges or prisms for scanning the lidar transmitter beam, and an advanced holographic polymer material was characterized at 2 microns wavelength. A preliminary solid state coherent lidar system design for demonstrating the technology readiness for global wind measurements from space was developed and the key technology areas needed to enable such missions were identified with the support of the MSFC Electro-Optics Branch personnel. A set of specifications for this demonstrator system was developed and the requirements for interfacing major lidar components and subsystems were established to serve as the basis for an integrated plan for the solid state coherent lidar technology development efforts at different NASA centers. The coherent lidar data base, developed earlier by the UAH personnel at NASA/MSFC, was upgraded and its content was further expanded by adding more lidar related materials. A World Wide Web server was also developed to familiarize the industry, academic and other government agencies and laboratories with the coherent lidar activities at the NASA/MSFC Electro-Optics Branch and to provide them with an efficient means of accessing the Electro-Optics information base through computer networks.

2.0 DETECTOR CHARACTERIZATION

2.1 INTRODUCTION

A Detector Characterization Facility (DCF), capable of measuring 2-micron detection devices and evaluating heterodyne receivers, was developed at the Marshall Space Flight Center. The DCF is capable of providing all the necessary detection parameters for design, development and calibration of coherent and incoherent solid state laser radar (lidar) systems. The coherent lidars in particular require an accurate knowledge of detector heterodyne quantum efficiency[1-3], nonlinearity properties[4-7] and voltage-current relationship[7-9], as a function of applied optical power. At present no detector manufacturer provides these quantities or adequately characterizes their detectors for heterodyne detection operation. In addition, the detector characterization facility measures the detectors DC and AC quantum efficiencies noise equivalent power and frequency response up to several GHz. The DCF is also capable of evaluating various heterodyne detection schemes such as balanced detectors and fiber optic interferometers. The design and analyses of measurements for the DCF was performed over the previous year and a detail description of its design and its capabilities was provided in the NASA report NAS8-38609/DO77[7]. It should also be noted that the DCF design was further improved to allow for characterization of diffractive and holographic optical elements and other critical optical components of coherent lidar systems.

2.2 DETECTOR CHARACTERIZATION FACILITY

The detector characterization optical design and measurement technique are illustrated in figures 1 and 2. The measurements have been based on using two diode-pumped, single mode, continuous wave, Tm, Ho:YLF (Thulium, Holmium:YLF) lasers operating at 2 microns wavelength. Both lasers can be tuned using an intracavity etalon over a wide range of about 22 nm or 1500 GHz centered at 2060 nm. The frequency of one of the lasers can be further controlled by adjusting its resonator length using a piezoelectric (PZT) translation stage. This laser can be continuously tuned over a frequency range of about 0.5 GHz by applying a voltage to the PZT stage. By adjusting the diode laser pump current, the continuous tuning range can be extended to several GHz. The continuously tunable laser produces up to 100 mW power at a single frequency and the other laser produces about 60 mW.

Two variable attenuators, utilizing a combination of a half-wave plate and a polarizer, are placed on the paths of each laser beams to allow for controlling the laser beams powers incident on the detector. The optical filters immediately in front of each laser block the 790 nm radiation, generated by the diode lasers pumping the laser gain media, from illuminating the detector under-the-test and the InAs monitor detectors. These filters transmit the 2-micron radiation, while considerably attenuating longer and shorter wavelengths. Both laser beams are passed through a single polarizer before illuminating the detector to ensure complete polarization match between the two beams on the detector.

In the optical system of figure 1, the Acousto-Optic Modulator (AOM) is used as an intensity modulator for noise equivalent power measurement. The AOM is driven by a fixed RF frequency

signal modulated by an adjustable amplitude and frequency signal. The AOM in turn modulates the laser beam intensity eliminating the need for using a mechanical chopper which can degrade the measurement accuracy. The chopper transmission function is highly variant depending on the position of the beam on the chopper wheel and its rotation frequency. Therefore, using a mechanical chopper would require frequent calibration that are tedious to perform and can affect the measurements repeatability.

The DCF can operate in both direct and heterodyne detection modes. In heterodyne detection mode, both lasers are used to illuminate the detector under-the-test and for the direct detection measurements, the output of one of the lasers is blocked. For direct detection measurements, the output of the continuously tunable laser is first measured by a precision power meter and thereafter is monitored by an InAs detector. The InAs detector has a 200 KHz bandwidth, which is more than sufficient for measuring any variation in the laser output power that may occur during the measurement procedure. For these measurements, a short focal length lens (25 mm) is placed in front of the detector being characterized. The short focal length lens will focus the beam to a spot size considerably smaller than the detector effective area to avoid introducing any truncation error in the measurements. The detector output is then amplified by an electronic receiver to be measured. The receiver also operates in two different modes, accordingly with direct and heterodyne detection measurement modes, using a manual switch and an on-line relay (figure 2). For the direct detection measurements, the receiver relay directs the detector signal towards an amplifier. The amplified signal is then measured by a precision digital voltmeter. For heterodyne detection measurements, the relay directs the signal directly through a transmission line, terminated at both ends by 50 ohms, to a wideband (21 GHz) spectrum analyzer.

The detector frequency response and heterodyne quantum efficiency are measured in heterodyne detection mode. For these measurements, the outputs of the lasers are focused by two long focal length (75 cm) lenses and then combined by a beam splitter at the detector. By mixing the two laser beams, the detector generates a current at the difference frequency between the two lasers. By varying the frequency of the continuously tunable laser and measuring the detector signal amplitude, the detector frequency response can be determined. The amplitude of the detector signal at the difference frequency is directly related to the product of the DC currents due to the individual beams and the detector's heterodyne quantum efficiency. Therefore by normalizing the detector IF signal power by the amplitudes of the detector DC components, the detector heterodyne quantum efficiency can be obtained as a function of signal frequency. Since the detector frequency response is related to the bias voltage, these measurements are repeated for different applied reverse-biased voltages.

The electronic receiver performs three functions: amplifying detector output current, interfacing the detector and the measurement instrument, and providing bias voltage to the detector. The operation of the receiver is shown in figure 2. The receiver uses an adjustable constant voltage source for providing the bias voltage to the detector, a high frequency relay for directing the detector output current, a DC-coupled transimpedance amplifier for direct detection measurements, and a 2 ft long high frequency transmission line for carrying the IF signal to the spectrum analyzer for heterodyne detection measurements. The transimpedance amplifier has a moderate gain (V_{out}/I_{in}) of about 600 and a bandwidth of about 70 MHz. The amplifier is a

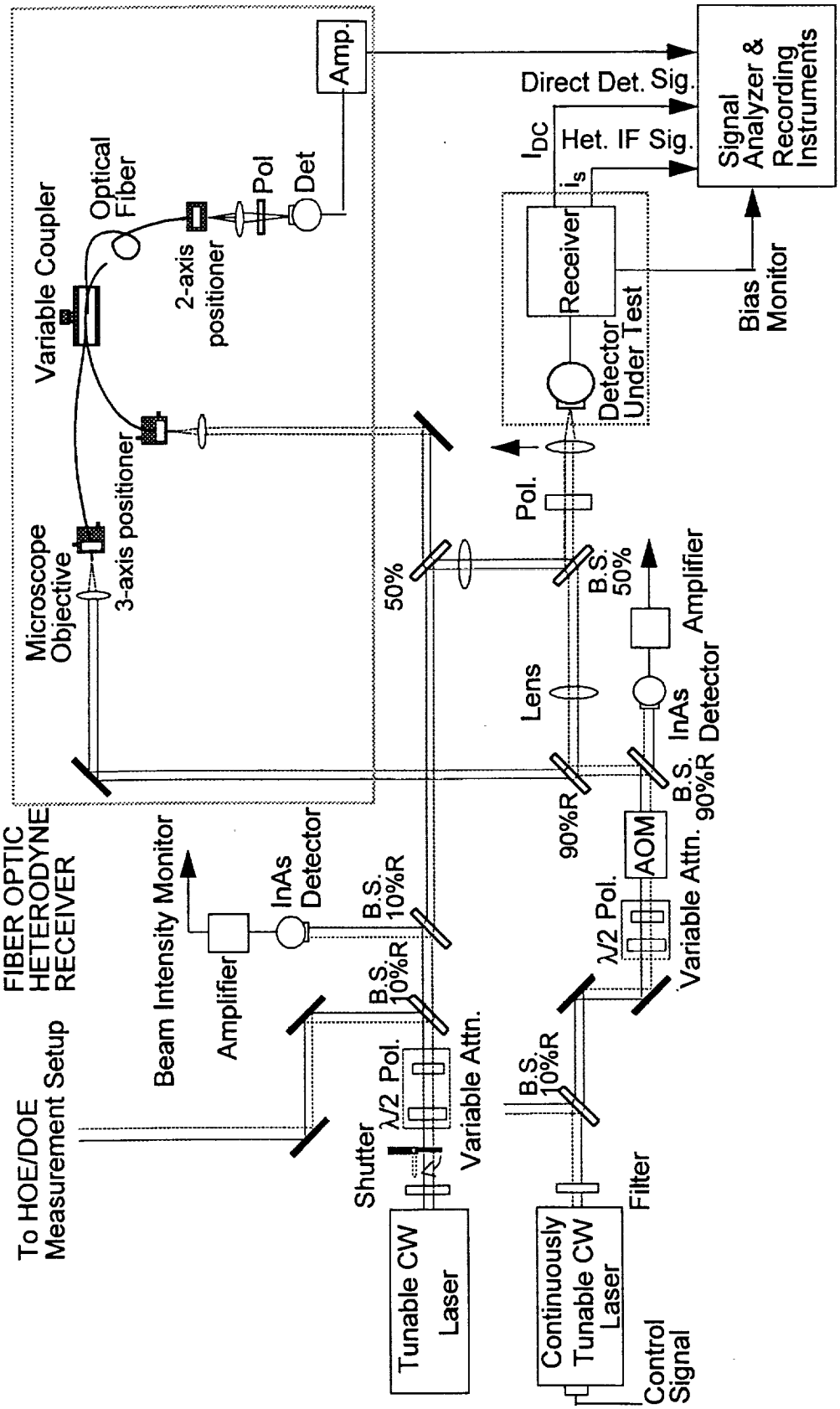

Figure 1. Detector Characterization Optical System.

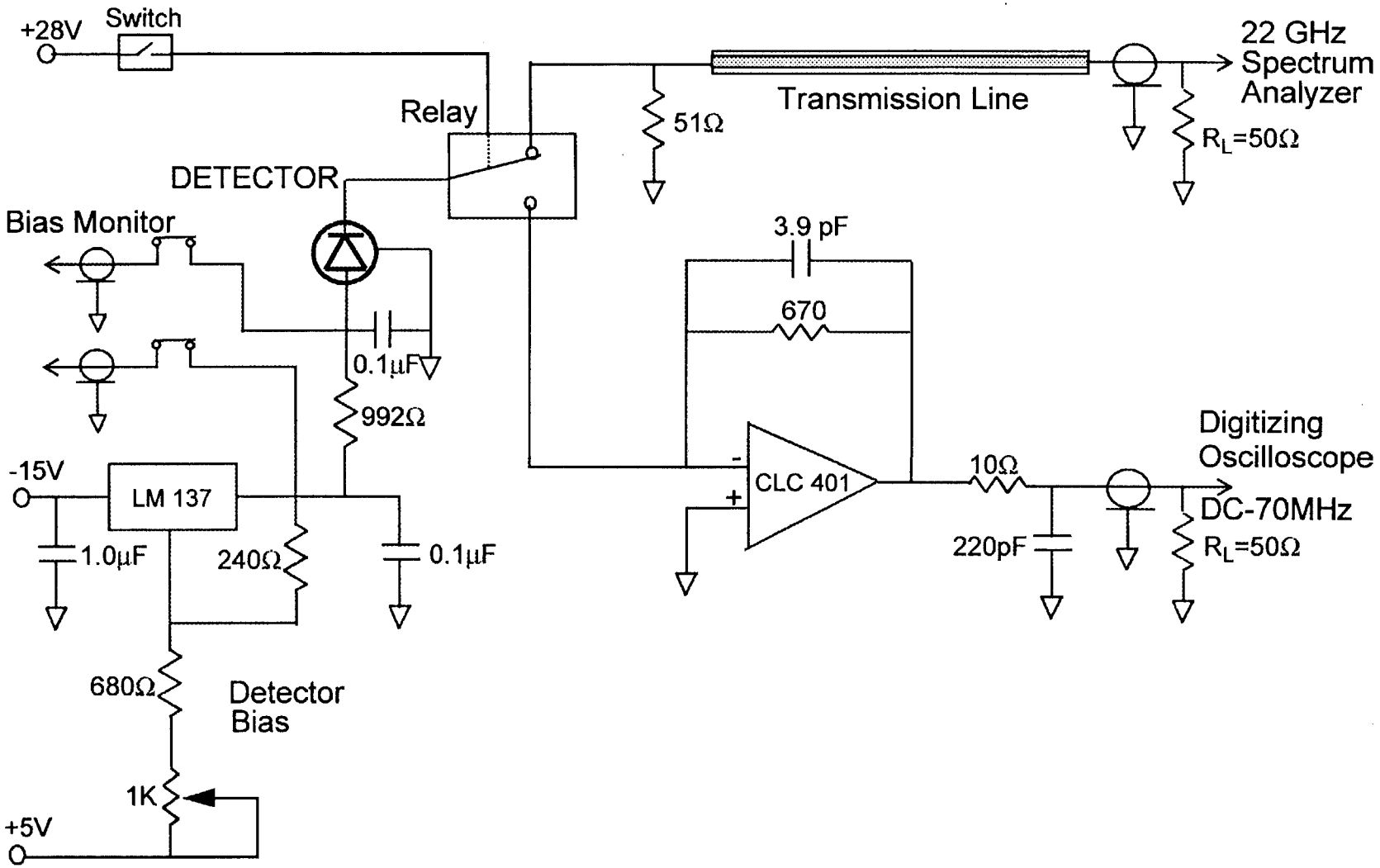

Figure 2. Detector Electronic Receiver

Current Feedback (CF) operational amplifier with an input impedance of about 50 ohms. The low input impedance ensures that virtually all the detector current will flow into the amplifier, since the internal resistance of the InGaAs detectors are typically of the order of hundreds of kilo ohms.

The receiver uses an adjustable voltage regulator as a constant voltage source for providing bias for the detector under-the-test. The detector bias voltage can be varied from +0.2 V to -5.0 V. The receiver provides output ports for measuring the applied bias voltage and monitoring the current flowing through the detector. By varying the applied bias voltage and measuring the detector current, a family of V-I curves for different applied optical power can be obtained. These curves along with the detector linearity and frequency response properties are necessary for determining the detector optimum local oscillator power and bias voltage for operation in a coherent lidar system.

As shown in figure 1, part of each laser beam is split and directed toward a fiber optic assembly that allows the evaluation of fiber optic heterodyne receivers. The two laser beams are coupled into two optical fibers to be mixed by a variable fiber optic coupler. The output of the coupler is then directed through another optical fiber toward a detector. This fiber optic interferometer assembly is capable of characterizing the optical fiber transmission properties and the coherent mixing efficiencies of fiber optic couplers. The variable coupler used in the fiber optic interferometer assembly will also allow the optimum mixing ratio of the signal and local oscillator to be determined experimentally. The same setup can also be used for evaluating balanced detectors receivers by using the second coupler output pigtail fiber to illuminate another detector simultaneously.

Also shown in figure 1 is a combination of a beamsplitter and two mirrors that splits a portion of the one of the lasers output and directs it towards a measurement setup for characterizing Holographic and Diffractive Optical Elements (HOE/DOE). HOE and DOE technologies have been studied as alternatives to optical wedge for scanning the lidar beam. The holographic and diffractive optical elements have the potential of substantially reducing the mass of the lidar systems and allowing for a much easier spacecraft accommodation design.

2.3 PRINCIPLES OF DETECTOR MEASUREMENTS

The DCF is capable of measuring all the necessary parameters for design, analysis and calibration of laser radar systems. Most of the detector parameters are measured directly and the remaining are deduced from measured quantities through simple mathematical manipulations. The primary detector parameters that are measured are listed in table 1.

The primary parameters that are measured direct detection measurements are listed in table 1.The detector parameters that will be measured by using a single laser beam (direct detection) are summarized in table 1. All the direct detection measurements are performed by the continuously tunable laser without having to readjust the mirrors or beam splitters for each measurement. It is particularly undesirable to readjust the angular position of the beam splitters, since their transmission to reflection ratios have a angular dependency. The variable attenuator utilizes a

combination of a half-wave plate and a polarizer to allow for controlling the laser beam power without causing the beam to deflect or translate as would be the case if neutral density filters are used. By placing or removing neutral density filters or any other form of substrates with a finite thickness during the characterization procedure, the laser beam will deviate from its original path introducing additional error in the measurements.

Table 1: Primary Detector Measurements

Measurement Mode	Parameter	Measurement
Direct Detection	Small Signal Responsivity	$\rho_0 = \frac{I_d}{P_{in}}$
	Detector Responsivity and Nonlinearity	$I_d = \rho P_{in} - \rho\alpha P_{in}^2$
	V-I Curves	$I_B = \frac{V_B}{R_B}$
Heterodyne Detection	Frequency Response	$H(f, V_B) = \left(\frac{\overline{i_h^2(f, V_B)}}{2 I_{DC1} I_{DC2}} \right)^{1/2}$

The direct detection measurements of the detectors are based on the following simple expression relating the detector output current to the applied optical power.

$$I_d (V_B) = \rho(V_B) P_{in} \tag{1}$$

where P_{in} is the incident optical power, I_d is the detector output current, ρ is the detector responsivity and V_B is the applied bias voltage. Therefore by accurately measuring the laser power incident on the detector and the detector output current, the detector responsivity can be determined. Since there are fundamental differences between heterodyne and direct detections, some of the detector parameters are defined and measured in less conventional manner. One of these parameters is the detector responsivity. As opposed to the direct detection lidars, for which the return signal power is usually well below the detector saturation level, the coherent lidars require a relatively high power local oscillator beam that may force the detectors to be operated in their nonlinear regions. Therefore, the knowledge of the detector responsivity as well as its nonlinearity behavior are essential for optimizing the heterodyne detection performance. For this reason, the detector responsivity is really needed to be specified by three different parameters: responsivity and nonlinearity coefficients ρ and α, and small signal responsivity ρ_0. These parameters relate the detector output current to the applied optical power as:

$$I_d = \rho_0 P_{in} \tag{2}$$

$$I_d = \rho P_{in} - \rho\alpha P_{in}^2 \tag{3}$$

To determine these parameters, the detector output current is measured as a function of applied optical power. The small signal responsivity is obtained by making a least-squares fit to Eq. (1) at low optical powers, and the responsivity and nonlinearity are determined by making a least-squares fit to Eq. (3). The measurement of the detector responsivities and nonlinearity coefficient are then performed at different bias voltage levels. Section 2.5 includes the results of these measurements for a 75 microns diameter InGaAs detector.

Eq. (1) can be written as:

$$I_d(V_B) = \left(\frac{e}{h\nu}\right)\eta_{DC}(V_B)\,P_{in} \tag{4}$$

where η_{DC} is the detector DC quantum efficiency, e is electron charge, h is Planck's constant, ν is the laser frequency. By comparing Eq. (2) and Eq. (4), the detector DC quantum efficiency can be written as:

$$\eta_{DC}(V_B) = \left(\frac{h\nu}{e}\right)\rho_0(V_B) \tag{5}$$

Another detector primary parameter is the detector voltage-current relationship for different optical power levels. The V-I curves are obtained by measuring the current flowing through the detector as a function of applied voltage across the detector for different applied optical power levels. The V-I curves are required for specifying the detector optimum bias voltage and bias resistor value in a heterodyne receiver, and for estimating the detector dark current noise. In addition, the V-I curves provide the data for estimating the detector series and shunt resistances. As discussed in section 3.1, the detector series resistance can play significant role in the performance of wideband heterodyne receivers. The detector shunt resistance at the operating reverse bias voltage V_B is equal to

$$R_d = \frac{\partial V_B}{\partial I_B} \tag{6}$$

The shunt resistance can be simply estimated by using two sets of points on the measured V-I curve and make a linear estimation of its slope (see section 2.5). The series resistance is determined by first making a least-squares fit to the detector diode model using the measured data at forward bias voltages. The detector diode model is given by:

$$I_d = I_0 e^{\left(\frac{e}{mKT}\right)Vd} \tag{7}$$

where I_0 is the detector saturation current and m is a empirical constant between 1 and 2. The detector forward resistance is equal to

$$R_f = \frac{dV_d}{dI_d} = \frac{mKT}{eI_0} e^{-\left(\frac{e}{mKT}\right)V_d} \tag{8}$$

The series resistance is estimated by evaluating R_f at relatively large forward bias currents and then is linearly interpolated at zero bias current. On page 26, this procedure has been shown graphically for an actual set of measured data.

The primary parameter measured in heterodyne detection mode is the detector frequency response function. For the heterodyne detection measurements, the short focal length lens immediately in front of the detector is removed from the optical path. First, the detector DC currents due to each beam are measured individually. At this stage, the receiver is set to operate in the direct detection mode, i.e., with the relay switched to the amplifier. Then, the receiver is switched to the heterodyne detection mode and both beams are allowed to illuminate the detector. The two laser beams are combined by a 50% beamsplitter and directed toward the detector. The detector in turn generate a signal with a frequency equal to the frequency difference between the two beams. The amplitude of this signal is directly related to the product of the DC currents due to the individual beams. The detector frequency response can then be determined by measuring the heterodyne signal power and normalizing it by the product of the DC currents due to the individual beams while varying the frequency of the continuously tunable laser. The expression below shows the relationship between the detector frequency response and the measured detector output currents.

$$H(f, V_B) = \left(\frac{\overline{i_h^2(f, V_B)}}{2 I_{DC1} I_{DC2}} \right)^{1/2} \tag{9}$$

The heterodyne detection measurements can be best described by the heterodyne detection equation below that relates the detector heterodyne signal current (i_h) to the laser beams powers, P_1 and P_2, incident on the detector.

$$i_h(f) = 2\left(\frac{e}{h\nu}\right)\eta_{AC}(f) F_0^{1/2} \sqrt{P_1 P_2} \cos(\omega_1 - \omega_2) t \tag{10}$$

Where ω_1 and ω_2 are the corresponding laser frequencies, η_{AC} is the detector AC quantum efficiency at frequency $f=2\pi(\omega_1-\omega_2)$, and F_0 is the signal power reduction factor that accounts for the loss of signal power due to imperfect wavefronts matching and optical misalignment. Taking the mean-square of the heterodyne current, we obtain the heterodyne signal power.

$$\overline{i_h^2(f)} = 2\left(\frac{e}{h\nu}\right)^2 \eta_{AC}^2(f) F_0 P_1 P_2 \tag{11}$$

Normalizing Eq. (11) by the individual DC currents due to P1 and P2 given by Eq. (4), we can write

$$\frac{\overline{i_h^2(f)}}{I_{DC1}I_{DC2}} = \frac{2\eta_{AC}^2(f)}{\eta_{DC}^2}F_0 \tag{12}$$

Rewriting the expression above as

$$\eta_{AC}(f) = \left(\frac{\overline{i_h^2(f)}}{2I_{DC1}I_{DC2}}(\eta_{DC}^2/F_0)\right)^{1/2} \tag{13}$$

By comparing Eq. (13) with eq. (9), the AC heterodyne quantum efficiency can be written in terms of the detector frequency response function, as following

$$\eta_{AC}(f) = \eta_{DC}H(f) \tag{14}$$

where the signal reduction factor F_0 is set equal to 1. It has been shown previously[7] that any reduction in the heterodyne signal power due to the optical misalignment and beams wavefronts mismatch for the measurement system of figure 1 will be negligible and F_0 will be essentially unity for the DCF heterodyne detection measurements. Therefore by quantifying the detector DC quantum efficiency as described earlier and measuring the heterodyne signal power and the direct detection DC currents due to the individual beams, the detector frequency response and AC quantum efficiency can be determined. The heterodyne signal power and the DC currents are related to the receiver output voltages as:

$$\overline{i_h^2} = \frac{\overline{v_{out}^2}}{g_1^2(f)} \tag{15}$$

$$I_{DC} = \frac{V_{out}}{g_2} \tag{16}$$

where g_1 and g_2 are the receiver gains corresponding to each channel. g_1 is equal to the equivalent impedance of the transmission line terminating resistors, that is 25; and g_2 is equal to the product of the transimpedance amplifier gain and the low-pass filter transmission (see figure 2). The values of g_1 and g_2 for the receiver of figure 2 are 25 and 518, respectively.

For an ideal shot noise-limited coherent lidar, the signal to noise ratio (SNR) is equal to

$$\frac{S}{N} = \frac{\eta_{AC}^2\eta_H P_s}{\eta_{DC}h\nu B_{IF}} \tag{17}$$

where η_H is the heterodyne mixing efficiency and P_s is the return signal power. The coherent lidar SNR is often expressed as

$$\frac{S}{N} = \frac{\eta_{HQE}\eta_H P_s}{h\nu B_{IF}} \tag{18}$$

where the quantity η_{HQE}, referred to as the "detector heterodyne quantum efficiency", and is equal to

$$\eta_{HQE} = \frac{\eta_{AC}^2}{\eta_{DC}} \tag{19}$$

In Eq. (19), η_H is a system parameter that quantifies the lidar optical heterodyne efficiency while η_{HQE} is a detector parameter that quantifies the efficiency of the detector in generating an AC electrical current at the difference frequency between the local oscillator and signal beams frequencies. Substituting Eq. (13) in Eq. (19), the detector heterodyne quantum efficiency can be written in terms of the measured detector output currents.

$$\eta_{HQE}(f) = \frac{\overline{i_h^2(f)}}{2I_{DC1}I_{DC2}}(\eta_{DC}/F_0) \tag{20}$$

The heterodyne quantum efficiency may also be written in terms of the detector frequency response, specifies as a primary measured parameter.

$$\eta_{HQE}(f) = \eta_{DC}H^2(f) \tag{21}$$

It should be noted that in Eqs. (10)-(21), the detector frequency response function H, AC quantum efficiency η_{AC} and heterodyne quantum efficiency η_{HQE} are functions of applied bias voltage V_B. However for clarity reason, the bias voltage dependance has not been shown.

Another detector parameter that can be extracted from the frequency response function is the detector junction capacitance. As explained in next chapter, the detector junction capacitance is one of the critical parameters for optimizing the heterodyne receiver performance and is usually the limiting factor for the receiver bandwidth. For determining the detector junction capacitance, the detector RC model is used without ignoring the detector series resistance (see section 3.1). Using the detector model, the detector/receiver transfer function is obtained and least-squared fitted to the measured frequency response function to determine the detector junction capacitance. The detector RC model is shown in figure 3, where R_L and C_{in} are the input resistance and capacitance of the DCF receiver, respectively.

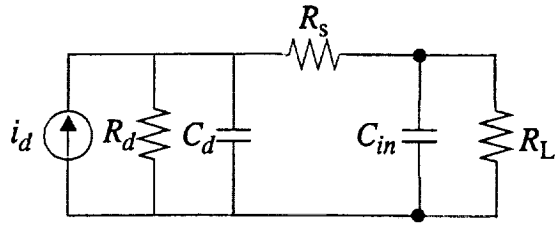

Figure 3. Detector RC model including series resistance.

Using figure 3, the detector/receiver transfer function can be obtained to be equal to

$$H(\omega) = \frac{v_{out}(\omega)}{i_d(\omega)} = \frac{R_L}{1 + j\omega(R_L(C_d + C_{in}) + R_s C_d) + (j\omega)^2 R_L R_s C_d C_{in}} \quad (22)$$

The value of C_d is estimated by minimizing the mean squared of the difference between the Eq. (22) and measured detector frequency response function (see section 2.4).

The DCF is capable of measuring all the parameters described above with a great degree of accuracy. The DCF optical system has been designed such that most measurements are insensitive to the optical misalignments. Reference [7] provides a detail error analysis for the measurements described above and the measurement system described in section 2.2. It has been shown that the measurement error due to the laser beam truncation and misalignment was estimated to be less than 1% for direct detection measurements with the 25 mm focal length lens. For heterodyne detection measurements, the signal power reduction factor F_0, that accounts for any reduction in the detector signal power due to the laser beams misalignment and displacement of reflective and focusing optics, has been shown to greater than 0.99. The heterodyne detection measurements are most sensitive to the relative transverse position of the beams in the detector plane and the beams pointing angles. The beams transverse position and angular misalignment tolerances are 1 mm and 1 mrad that are easy achieve using conventional alignment procedures.

2.4 DCF CALIBRATION

Once the DCF optical system was aligned a calibration procedure was performed. The DCF calibration procedure is relatively simple and it is recommended that the InAs monitor detectors to be re-calibrated before measuring each detector. The following summarizes the results of the this calibration procedure and the calibration constant required for determining the parameters of the detectors under-the-test.

Wavelengths

Laser #1 = 2066.811 nm at 2.30 A diode laser current
Laser #2 = 2066.814 nm at 3.30A diode laser current

Transmission Line

$R_L = 25.35\ \Omega$

$C_{in} = 0.4$ pF

Amplifier

$V_B = 0$

	No Optical Power	Beam #1	Beam #2
Transmission Line	0	8.04	1.04
Amplifier	-2	180.6	21.6
Ratio (Amp/Trans. Line)		22.71	22.79

Conversion factor (Amplifier to Transmission Line) = 1/22.75

Monitor Detector

Calibration result for the InAs monitor detector for laser number 1 is given in figure 4. The absolute calibration of the second monitor detector for laser number 2 is not necessary for the detector measurements. The second monitor detector is mainly for monitoring any laser power fluctuations or any gradual laser power level changes that may occur during the detector measurements.

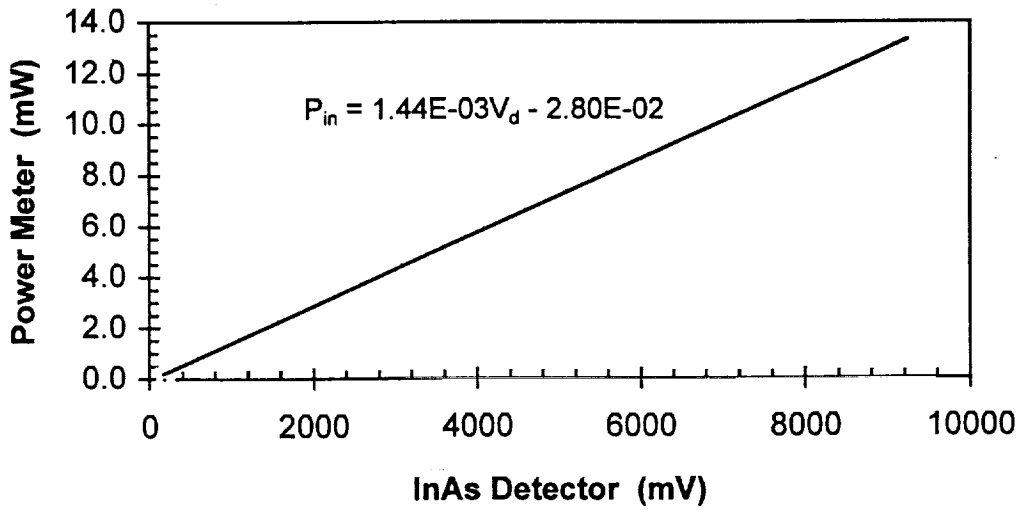

Figure 4. Calibration of InAs Monitor Detector.

2.5 CHARACTERIZATION OF A 2-MICRON InGaAs DETECTOR

A 75 microns diameter InGaAs detector with a cutoff wavelength of 2.5 microns, acquired from Sensors Unlimited, Inc., was fully characterized in the NASA/MSFC Detector Characterization Facility. The results of the measurements are provided in this section. These results were then used to determine the optimum design parameters of a heterodyne receiver as a function of operating bandwidth. The heterodyne design analysis and the receiver design are described in the next chapter.

The following data are the results of the detector measurements performed in the DCF. The detector model number is SU75-2.5-TO and its serial number is 8364-PIN.

RESPONSIVITY AND LINEARITY MEASUREMENTS

V_B=0.00 V

Notes: Detector anode terminated by 50 ohms
With laser beam blocked, InAs laser power monitor detector reads 19.2 mV and detector direct output is 0.0 mV.

InAs Power Monitor (mV)	Detector Output (mV)	Incident Power P_{in} (mW)	Detector current I_d (mA)
154	11.1	0.194	0.2160
203	15.0	0.264	0.2918
306	23.0	0.413	0.4475
410	30.4	0.562	0.5914
508	36.4	0.704	0.7082
609	41.5	0.849	0.8074
750	47.0	1.052	0.9144
902	52.4	1.271	1.0195
1108	58.2	1.568	1.1323
1300	62.3	1.844	1.2121
1504	66.1	2.138	1.2860
1756	70.1	2.501	1.3638
2025	73.6	2.888	1.4319
2260	76.2	3.226	1.4825
2512	78.7	3.589	1.5311
2745	80.7	3.925	1.5700
3003	82.6	4.296	1.6070
3258	84.2	4.664	1.6381
3520	85.8	5.041	1.6693

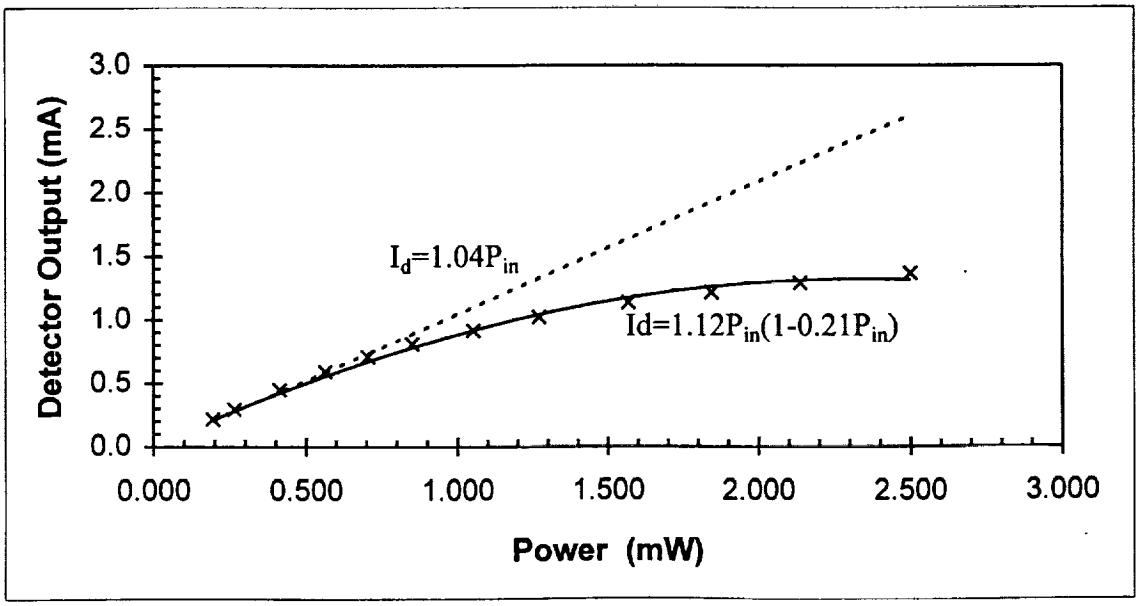

V_B=1.000 V

V_{Bi}=1.008 V

Notes:

With laser beam blocked, InAs laser power monitor detector reads 19.7 mV and detector direct output is 0.4 mV.

InAs Power Monitor (mV)	Detector Output (mV)	Incident Power P_{in} (mW)	Detector current I_d (mA)
143	10.2	0.178	0.1907
204	14.8	0.266	0.2802
302	22.2	0.407	0.4241
407	30.2	0.558	0.5798
507	37.7	0.702	0.7257
603	41.6	0.840	0.8016
750	50.6	1.052	0.9767
910	53.7	1.282	1.0370
1120	55.1	1.585	1.0642
1316	55.9	1.867	1.0798
1504	56.4	2.138	1.0895
1753	57.0	2.496	1.1012
2012	57.4	2.869	1.1089
2250	57.6	3.212	1.1128
2530	57.9	3.615	1.1187
2760	58.1	3.946	1.1226
3000	58.2	4.292	1.1245
3290	58.4	4.710	1.1284
3505	58.5	5.019	1.1304

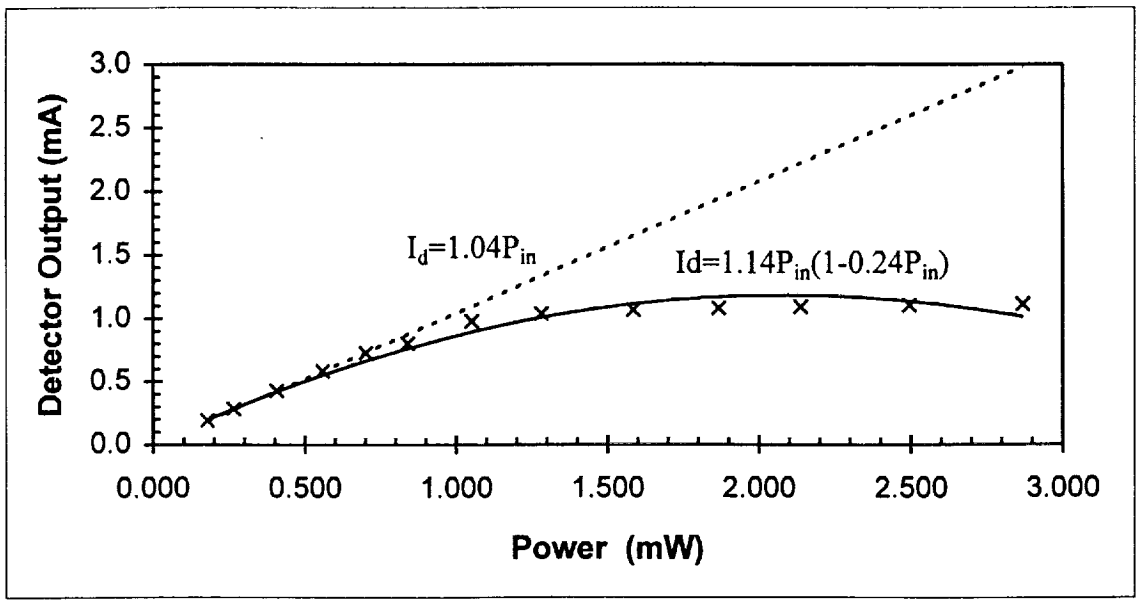

V_B=1.505 V

V_{Bi}=1.514 V

Notes:

With laser beam blocked, InAs laser power monitor detector reads 19.4 mV and detector direct output is 0.4 mV.

InAs Power Monitor (mV)	Detector Output (mV)	Incident Power P_{in} (mW)	Detector current I_d (mA)
150	11.7	0.188	0.2198
205	16.2	0.267	0.3074
302	23.7	0.407	0.4533
404	31.1	0.554	0.5973
508	38.4	0.704	0.7393
600	45.0	0.836	0.8677
768	57.6	1.078	1.1128
922	69.1	1.300	1.3366
1114	74.2	1.576	1.4358
1350	77.3	1.916	1.4961
1513	78.2	2.151	1.5136
1740	79.1	2.478	1.5311
2067	80.0	2.948	1.5486
2247	80.3	3.208	1.5545
2490	80.7	3.558	1.5623
2792	81.1	3.992	1.5700
3020	81.3	4.321	1.5739
3280	81.6	4.695	1.5798
3554	81.8	5.090	1.5837

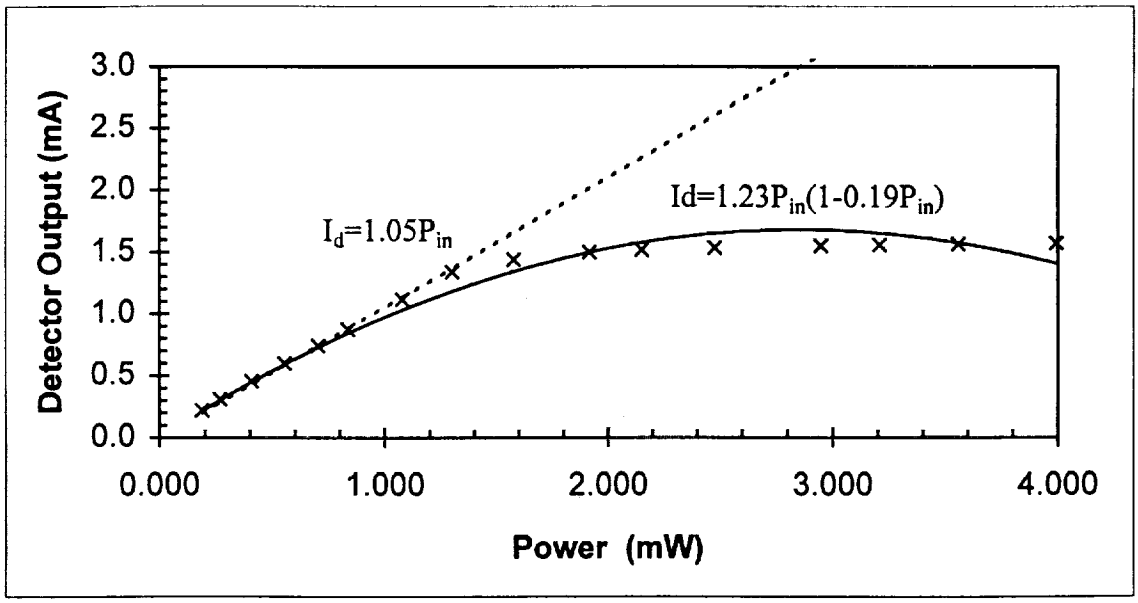

V_B=2.003 V

V_{Bi}=2.013 V

Notes:

With laser beam blocked, InAs laser power monitor detector reads 19.3 mV and detector direct output is 0.5 mV.

InAs Power Monitor (mV)	Detector Output (mV)	Incident Power P_{in} (mW)	Detector current I_d (mA)
144	11.9	0.179	0.2218
208	17.5	0.272	0.3307
300	25.3	0.404	0.4825
410	34.1	0.562	0.6537
506	41.3	0.701	0.7938
606	48.4	0.845	0.9319
750	57.9	1.052	1.1167
920	69.1	1.297	1.3346
1105	83.5	1.563	1.6148
1309	94.9	1.857	1.8366
1500	98.8	2.132	1.9125
1774	100.9	2.527	1.9533
2024	101.9	2.887	1.9728
2240	103.0	3.198	1.9942
2530	103.9	3.615	2.0117
2750	104.4	3.932	2.0214
3015	104.9	4.314	2.0311
3290	105.3	4.710	2.0389
3530	105.6	5.055	2.0447

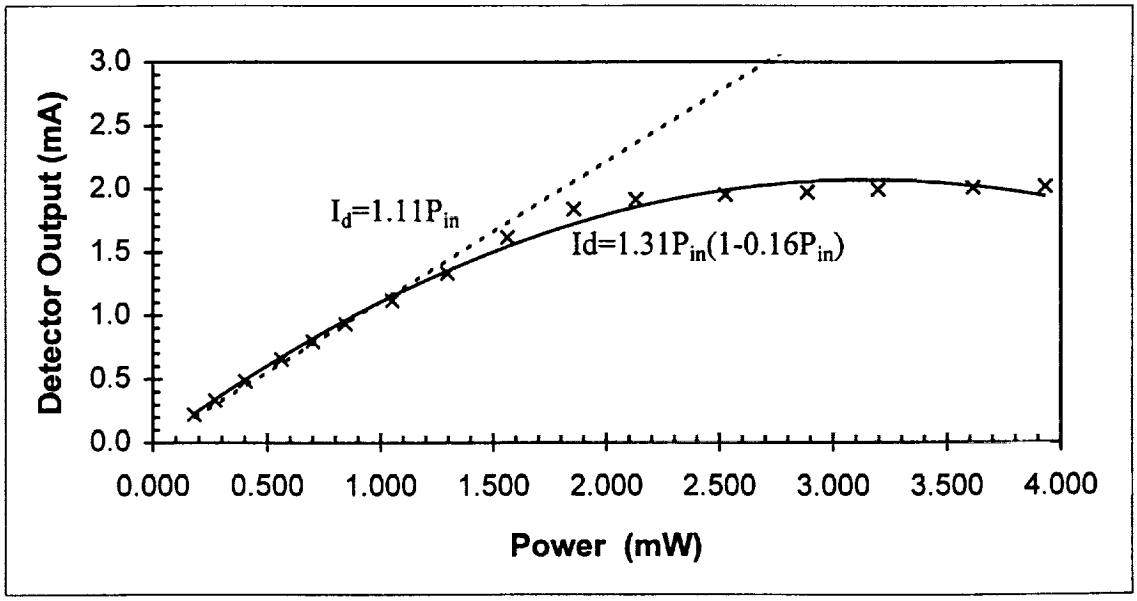

V_B=2.502 V

V_{Bi}=2.513 V

Notes:

With laser beam blocked, InAs laser power monitor detector reads 19.7 mV and detector direct output is 0.6 mV.

InAs Power Monitor (mV)	Detector Output (mV)	Incident Power P_{in} (mW)	Detector current I_d (mA)
140	12.3	0.174	0.2276
204	18.3	0.266	0.3444
303	27.3	0.408	0.5195
408	36.2	0.560	0.6926
498	43.7	0.689	0.8385
758	62.9	1.064	1.2121
900	72.2	1.268	1.3930
1123	86.1	1.589	1.6634
1300	99.0	1.844	1.9144
1500	113.8	2.132	2.2023
1750	120.9	2.492	2.3405
2017	123.2	2.876	2.3852
2245	124.3	3.205	2.4066
2500	125.2	3.572	2.4241
2760	126.6	3.946	2.4514
2964	127.1	4.240	2.4611
3255	127.9	4.659	2.4767
3510	128.4	5.026	2.4864

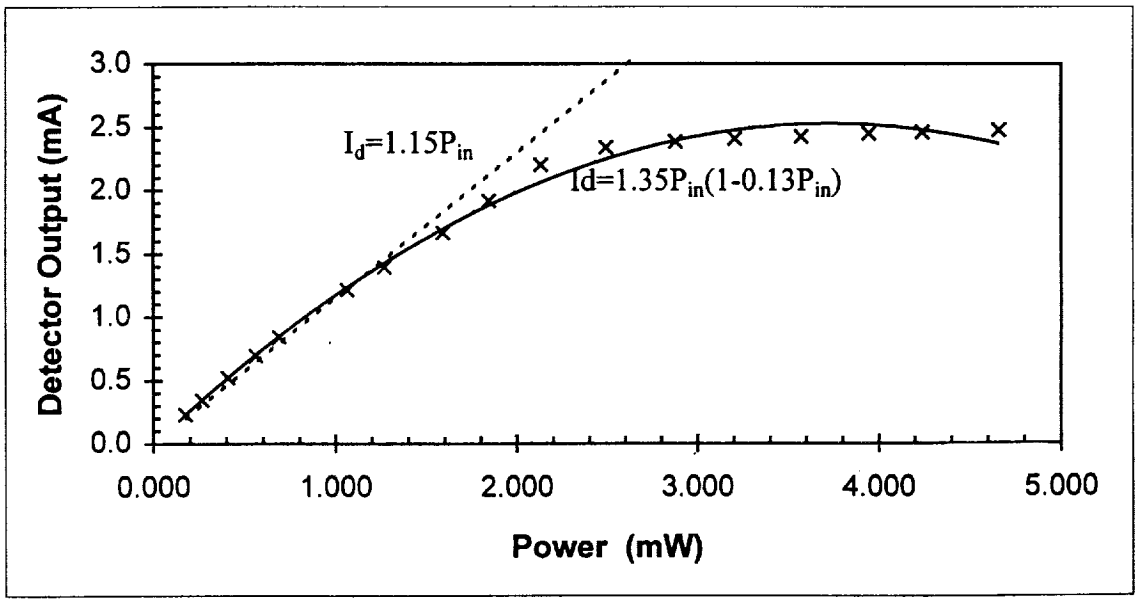

V_B=3.001 V

V_{Bi}=3.014 V

Notes:

With laser beam blocked, InAs laser power monitor detector reads 19.1 mV and detector direct output is 0.6 mV.

InAs Power Monitor (mV)	Detector Output (mV)	Incident Power P_{in} (mW)	Detector current I_d (mA)
144	13.5	0.179	0.2510
206	19.6	0.269	0.3696
307	29.3	0.414	0.5584
407	38.3	0.558	0.7335
510	47.2	0.706	0.9066
745	65.9	1.045	1.2704
920	78.5	1.297	1.5156
1110	90.8	1.570	1.7549
1310	102.4	1.858	1.9805
1500	115.1	2.132	2.2276
1760	134.4	2.506	2.6031
2048	143.6	2.921	2.7821
2260	145.4	3.226	2.8171
2492	146.5	3.560	2.8385
2714	147.3	3.880	2.8541
3005	149.4	4.299	2.8949
3234	150.1	4.629	2.9086
3595	151.1	5.149	2.9280

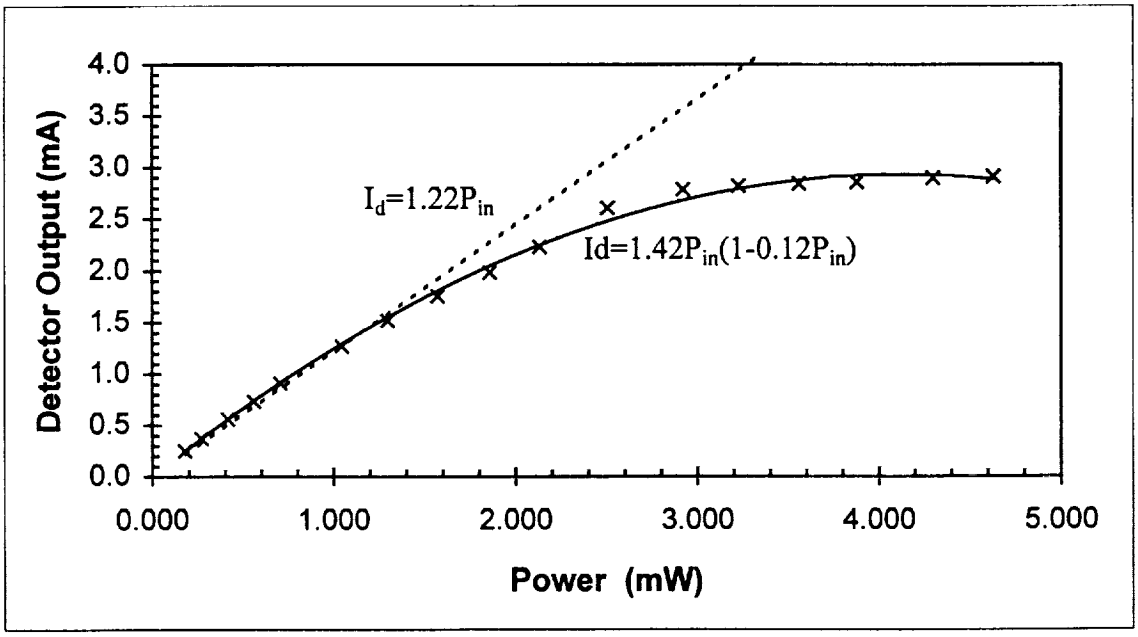

V_B=3.500 V

V_{Bi}=3.514 V

Notes:

With laser beam blocked, InAs laser power monitor detector reads 19.1 mV and detector direct output is 0.7 mV.

InAs Power Monitor (mV)	Detector Output (mV)	Incident Power P_{in} (mW)	Detector current I_d (mA)
144	14.2	0.179	0.2626
207	20.7	0.270	0.3891
310	31.0	0.418	0.5895
401	39.7	0.549	0.7588
510	49.6	0.706	0.9514
740	69.3	1.038	1.3346
920	83.3	1.297	1.6070
1100	96.2	1.556	1.8580
1314	109.8	1.864	2.1226
1512	120.8	2.149	2.3366
1760	135.9	2.506	2.6304
2080	159.0	2.967	3.0798
2250	163.0	3.212	3.1576
2528	167.8	3.612	3.2510
2756	169.2	3.941	3.2782
3045	170.8	4.357	3.3093
3250	171.6	4.652	3.3249
3520	172.4	5.041	3.3405

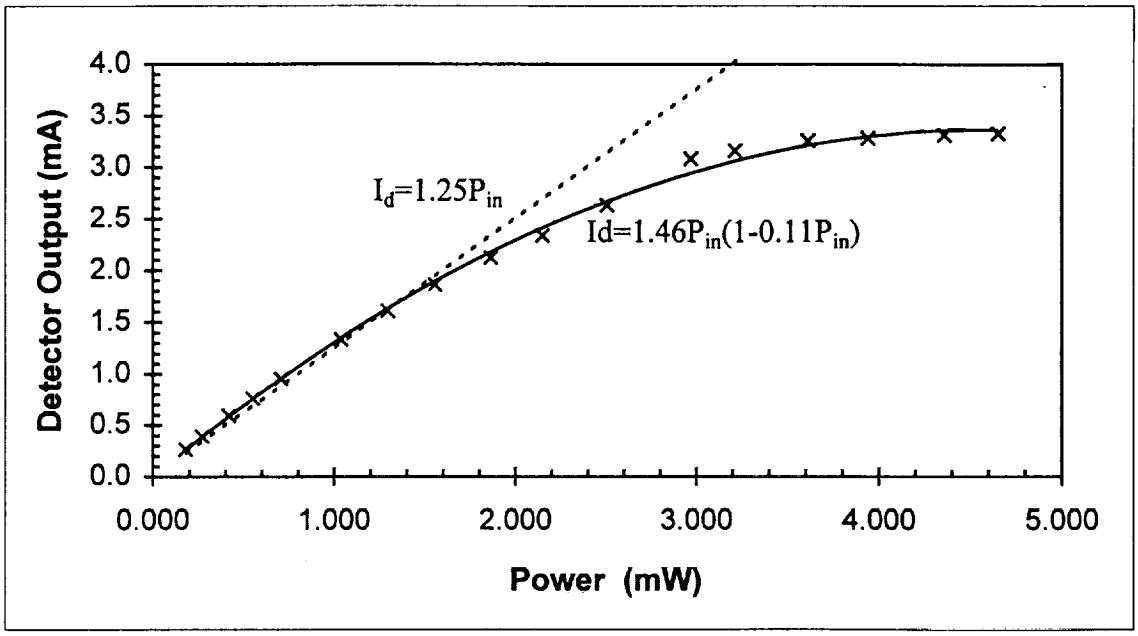

V_B=4.000 V

V_{Bi}=4.016 V

Notes:

With laser beam blocked, InAs laser power monitor detector reads 19.0 mV and detector direct output is 0.8 mV.

InAs Power Monitor (mV)	Detector Output (mV)	Incident Power P_{in} (mW)	Detector current I_d (mA)
147	15.3	0.184	0.2821
210	22.3	0.274	0.4183
304	32.1	0.410	0.6089
404	42.1	0.554	0.8035
505	52.0	0.699	0.9961
600	60.8	0.836	1.1673
741	73.2	1.039	1.4086
925	88.0	1.304	1.6965
1110	101.9	1.570	1.9669
1290	114.6	1.830	2.2140
1520	128.7	2.161	2.4883
1747	140.9	2.488	2.7257
2010	155.7	2.866	3.0136
2253	173.8	3.216	3.3658
2520	184.5	3.601	3.5739
2720	189.6	3.889	3.6732
3010	191.5	4.306	3.7101
3270	192.8	4.681	3.7354
3510	193.6	5.026	3.7510

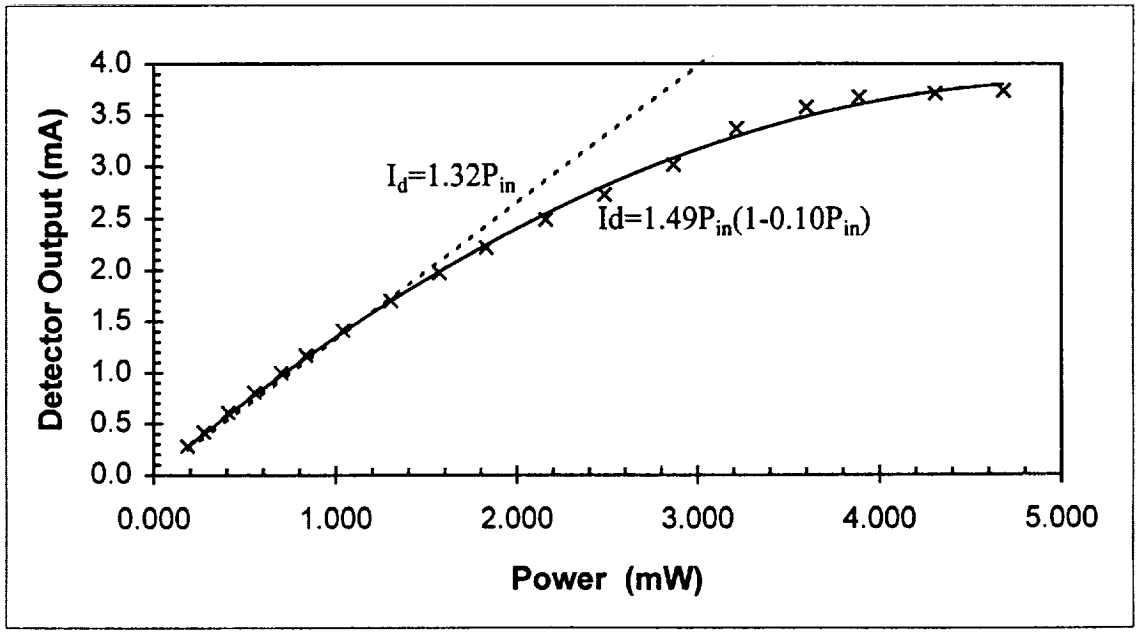

V_B=4.47 V

V_{Bi}=4.49 V

Notes:

With laser beam blocked, InAs laser power monitor detector reads 19.3 mV and detector direct output is 0.8 mV.

InAs Power Monitor (mV)	Detector Output (mV)	Incident Power P_{in} (mW)	Detector current I_d (mA)
143	15.5	0.178	0.2860
203	22.5	0.264	0.4222
307	33.9	0.414	0.6440
403	44.1	0.552	0.8424
502	54.2	0.695	1.0389
602	63.9	0.839	1.2276
751	77.5	1.053	1.4922
908	90.9	1.280	1.7529
1105	106.8	1.563	2.0623
1319	122.3	1.871	2.3638
1502	134.6	2.135	2.6031
1760	149.6	2.506	2.8949
2008	162.4	2.864	3.1440
2252	174.8	3.215	3.3852
2570	198.0	3.673	3.8366
2757	205.1	3.942	3.9747
3048	207.4	4.361	4.0195
3280	213.2	4.695	4.1323
3508	214.4	5.024	4.1556

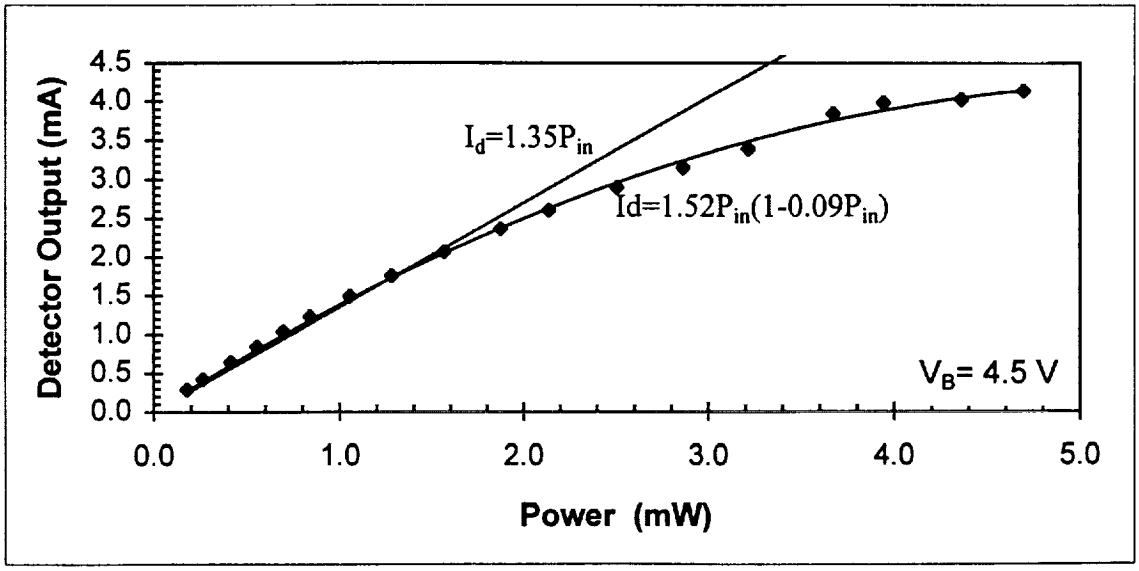

Detector Responsivity and Linearity
Summary Of Results

V_B (V)	Linear Responsivity		Non-Linear Responsivity	
	$_0$ (A/W)	DC	(mA/mW)	(1/mW)
0.0	1.04	0.6244	1.12	0.21
1.0	1.04	0.6244	1.14	0.24
1.5	1.05	0.6304	1.23	0.19
2.0	1.11	0.6664	1.31	0.16
2.5	1.15	0.6904	1.35	0.13
3.0	1.22	0.7324	1.42	0.12
3.5	1.25	0.7505	1.46	0.11
4.0	1.32	0.7925	1.49	0.10
4.5	1.35	0.8105	1.52	0.09

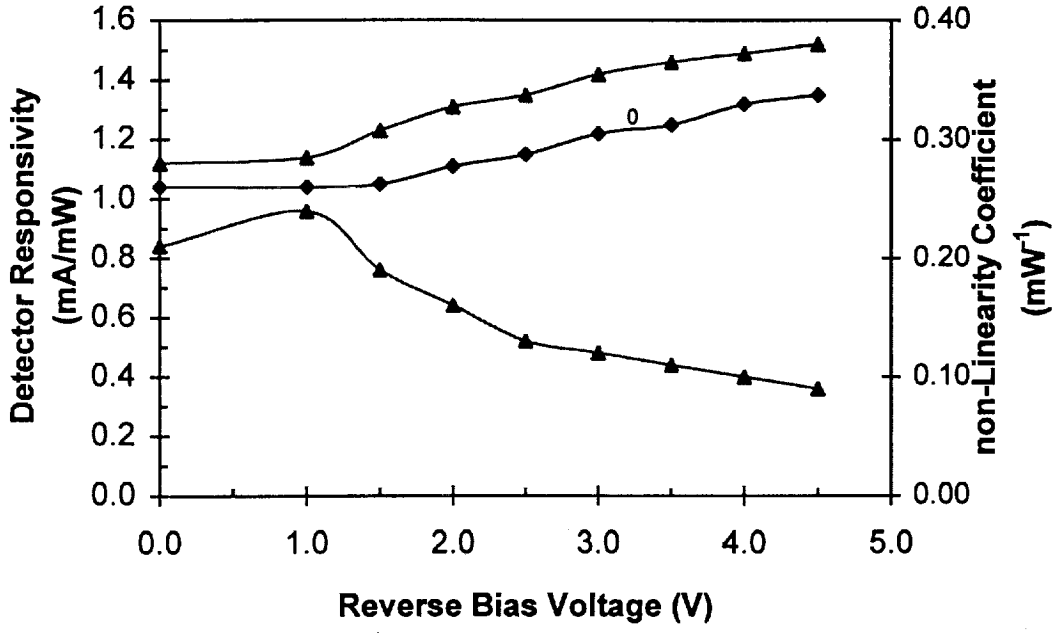

Voltage-Current Characteristics

Optical Power=0.0

Bias Current Monitor V_{Bi} (mV)	Bias Voltage Monitor V_B (mV)	Detector Voltage V_d (V)	Detector Current I_d (A)	Detector Resistance R_d ( )
1790.0	289.9	0.212173	1512.198	
1709.0	284.3	0.210480	1436.190	22.8
1622.0	278.2	0.208572	1354.637	23.9
1543.0	272.6	0.206775	1280.645	26.2
1517.0	270.7	0.206124	1256.351	26.8
1476.0	267.7	0.205093	1218.044	27.6
711.0	203.0	0.176678	512.097	67.8
550.0	185.0	0.166088	367.944	91.3
398.0	164.0	0.151875	235.887	147.5
295.5	145.1	0.137307	151.613	238.1
271.2	139.4	0.132571	132.863	243.8
267.7	138.6	0.131911	130.141	246.5
243.0	132.5	0.126774	111.391	310.3
144.5	99.9	0.097589	44.960	1078.9
54.8	46.2	0.045754	8.669	4535.5
0.0	0.0	0.000000	0.000	9807.2
-24.0	-22.0	-0.021896	-2.016	14550.3
-101.8	-96.3	-0.096015	-5.544	84718.0
-258.8	-251.9	-0.251542	-6.956	321895.1
-509.0	-501.5	-0.501111	-7.560	456449.0
-758.0	-750.0	-0.749585	-8.065	491980.6
-1006.0	-997.5	-0.997060	-8.569	492972.6
-1256.0	-1247.0	-1.246534	-9.073	494956.6
-1506.0	-1496.5	-1.496008	-9.577	496940.6
-1758.0	-1748.0	-1.747482	-10.081	500908.6
-2012.0	-2001.5	-2.000956	-10.585	497932.6
-2261.0	-2250.0	-2.249430	-11.089	469825.9
-2529.0	-2517.4	-2.516799	-11.694	455757.6
-2765.0	-2752.9	-2.752273	-12.198	434715.1
-3005.0	-2992.3	-2.991642	-12.802	383329.3
-3266.0	-3252.6	-3.251906	-13.508	345518.9
-3524.0	-3509.8	-3.509064	-14.315	308336.6
-3765.0	-3750.0	-3.749223	-15.121	294366.2
-4015.0	-3999.2	-3.998329	-15.978	283719.0
-4253.0	-4236.3	-4.235435	-16.835	276716.6
-4477.0	-4459.5	-4.458593	-17.641	

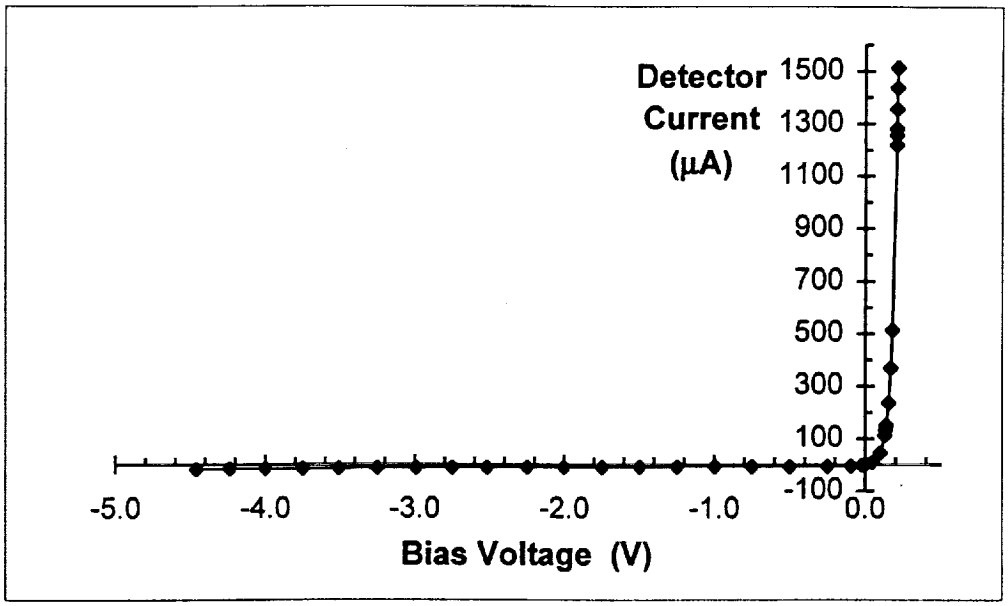
Detector Current (μA)
1500
1300
1100
900
700
500
300
100
-100
-5.0
-4.0
-3.0
-2.0
-1.0
0.0
Bias Voltage (V)

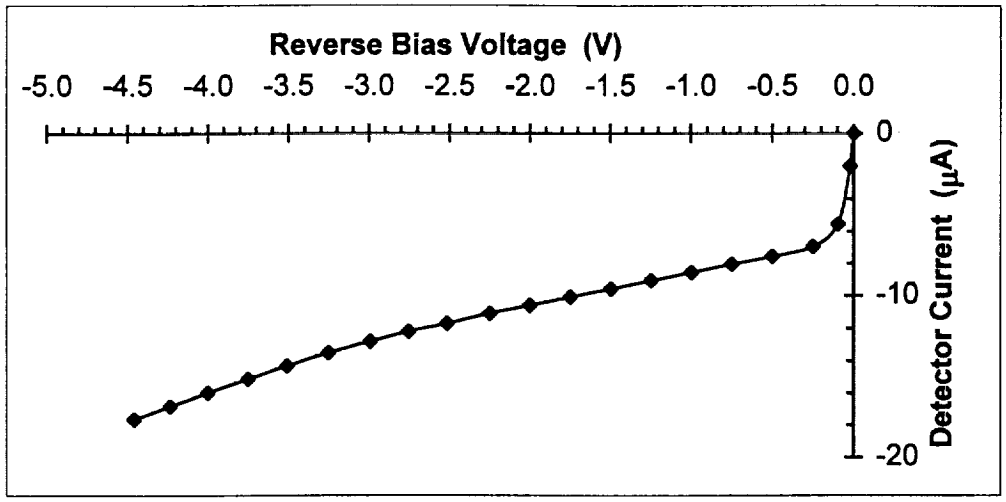
Reverse Bias Voltage (V)
-5.0 -4.5 -4.0 -3.5 -3.0 -2.5 -2.0 -1.5 -1.0 -0.5 0.0
0
-10
-20
Detector Current (μA)

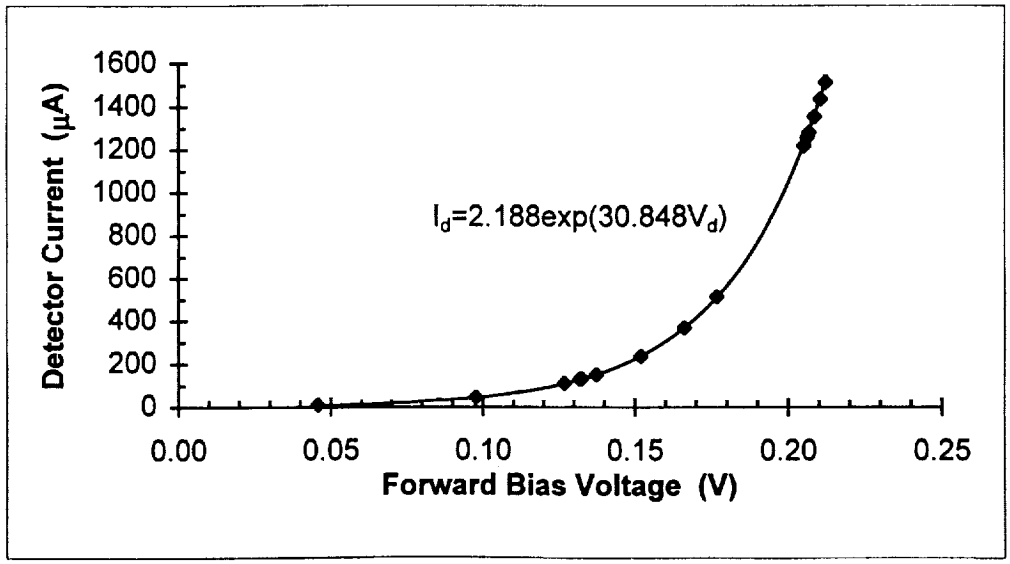
Detector Current (μA)
1600
1400
1200
1000
800
600
400
200
0
I_d=2.188exp(30.848V_d)
0.00
0.05
0.10
0.15
0.20
0.25
Forward Bias Voltage (V)

V-I Characteristic equation:

$I_d=2.19X10^{-6}exp(30.85V_d)$ $V_d>50mV$

$I_d=7.4X10^{-6}(exp(21.78V_d)-1)$ $V_d<50mV$

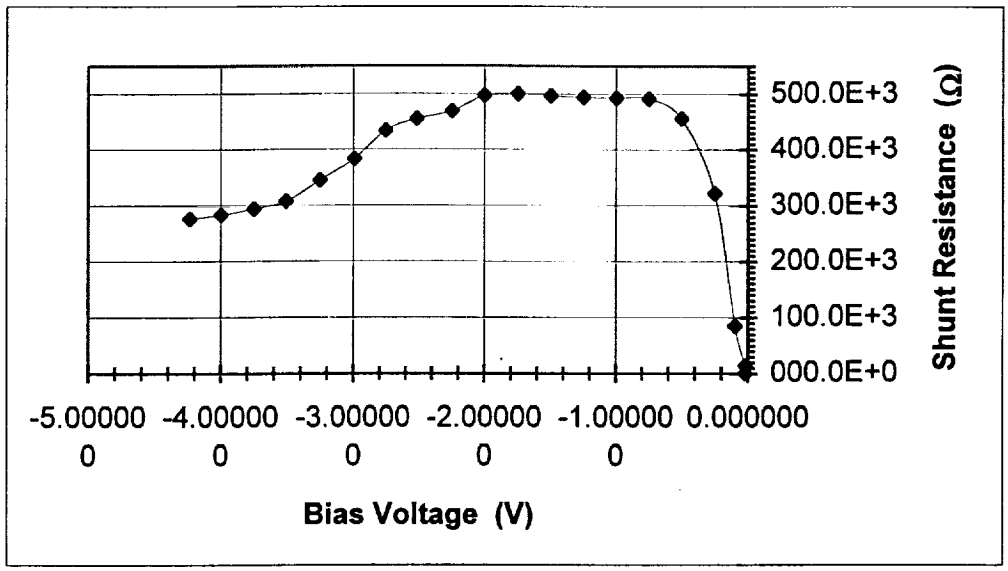

$1/R_f=dI_d/dV_d$

$R_f=1.48X10^4exp(-30.85V_d)$

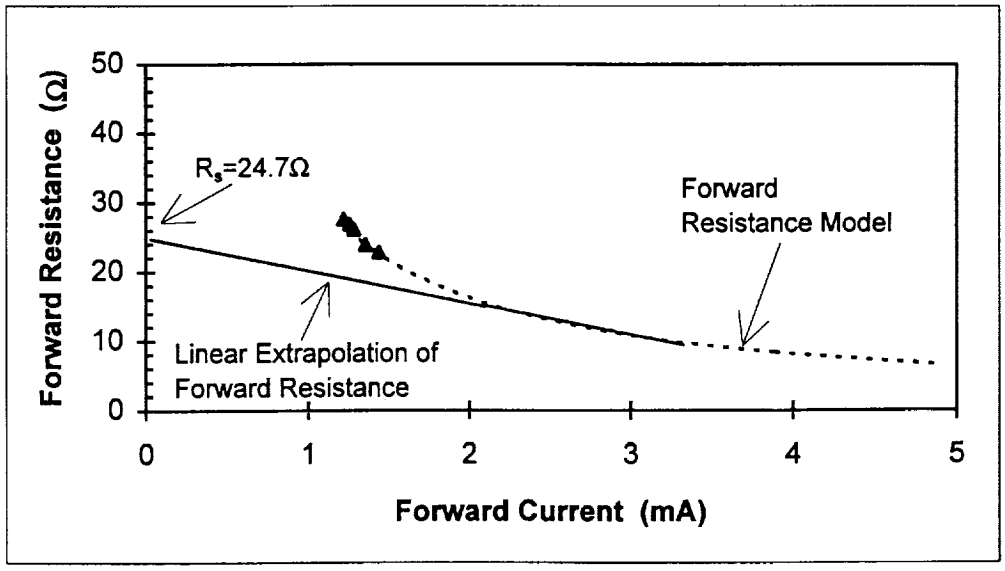

Optical Power=0.25mW

InAs Monitor=196mV

Bias Current Monitor V_{Bi} (mV)	Bias Voltage Monitor V_B (mV)	Detector Voltage V_d (V)	Detector Current I_d (A)	Detector Resistance R_d ( )
304.7	167.1	0.15997	138.710	
144.0	144.3	0.14432	-0.302	152.0
17.2	120.2	0.12554	-103.831	132.4
-11.9	115.9	0.12252	-128.831	198.7
-105.7	86.5	0.09646	-193.750	706.0
-204.9	36.9	0.04943	-243.750	3379.7
-253.9	-2.2	0.01084	-253.730	9774.3
-363.6	-104.7	-0.09129	-260.988	36477.3
-511.0	-249.0	-0.23542	-264.113	44812.8
-773.0	-505.0	-0.49111	-270.161	39483.3
-1036.0	-761.0	-0.74675	-277.218	35448.0
-1288.0	-1006.0	-0.99139	-284.274	31437.7
-1545.0	-1254.0	-1.23892	-293.347	24567.5
-1811.0	-1508.0	-1.49230	-305.444	21441.9
-2089.0	-1774.0	-1.75768	-317.540	29172.8
-2332.0	-2010.0	-1.99332	-324.597	28604.9
-2604.0	-2269.0	-2.25164	-337.702	20437.5
-2849.0	-2503.0	-2.48507	-348.790	21435.7
-3126.0	-2768.0	-2.74945	-360.887	29142.4
-3369.0	-3004.0	-2.98509	-367.944	30720.3
-3626.0	-3252.0	-3.23262	-377.016	25655.9
-3900.0	-3515.0	-3.49505	-388.105	29783.8
-4145.0	-3753.0	-3.73269	-395.161	29877.8
-4402.0	-4000.0	-3.97917	-405.242	23045.7
-4450.0	-4046.0	-4.02507	-407.258	

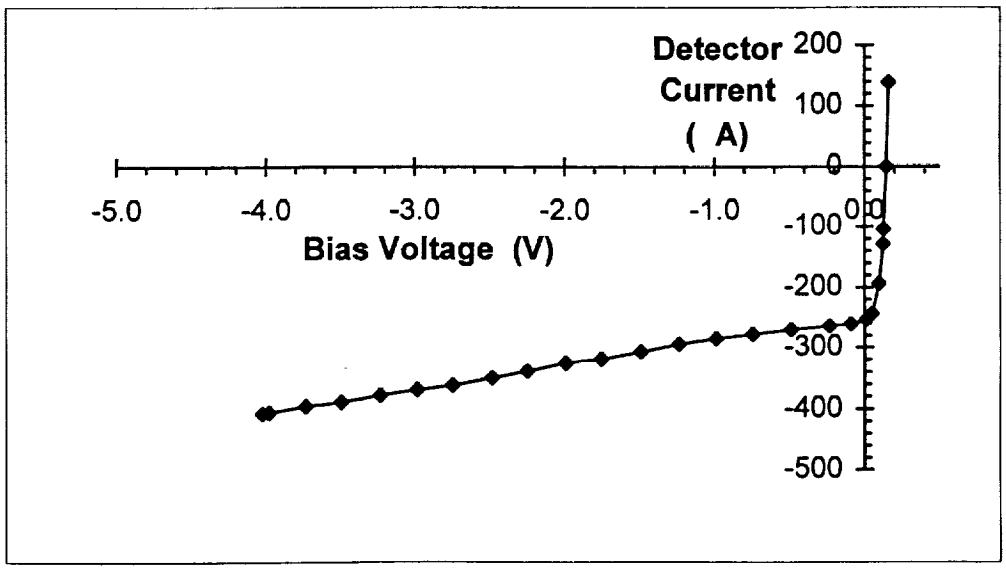

Optical Power=0.5mW

InAs Monitor=387mV

Bias Current Monitor V_{Bi} (mV)	Bias Voltage Monitor V_B (mV)	Detector Voltage V_d (V)	Detector Current I_d (A)	Detector Resistance R_d ( )
313.2	177.0	0.169943	137.298	
161.7	160.3	0.160227	1.411	82.6
0.0	139.6	0.146833	-140.726	114.9
-94.6	125.2	0.136589	-221.573	144.8
-238.6	98.8	0.116282	-340.121	316.5
-506.0	0.5	0.026744	-510.585	6433.0
-678.0	-150.7	-0.123378	-531.552	141808.0
-782.0	-254.0	-0.226642	-532.258	140405.8
-1033.0	-503.0	-0.475538	-534.274	110264.3
-1301.0	-757.0	-0.728813	-548.387	14985.6
-1577.0	-1007.0	-0.977466	-574.597	10399.0
-1861.0	-1268.0	-1.237274	-597.782	11568.5
-2135.0	-1521.0	-1.489186	-618.952	12319.5
-2384.0	-1752.0	-1.719253	-637.097	12384.9
-2661.0	-2008.0	-1.974165	-658.266	13517.3
-2931.0	-2261.0	-2.226284	-675.403	14367.1
-3204.0	-2516.0	-2.480352	-693.548	11411.7
-3468.0	-2744.0	-2.706486	-729.839	9776.3
-3756.0	-3010.0	-2.971346	-752.016	11785.0
-4037.0	-3269.0	-3.229206	-774.194	11198.8
-4299.0	-3509.0	-3.468067	-796.371	12167.9
-4498.0	-3694.0	-3.652341	-810.484	

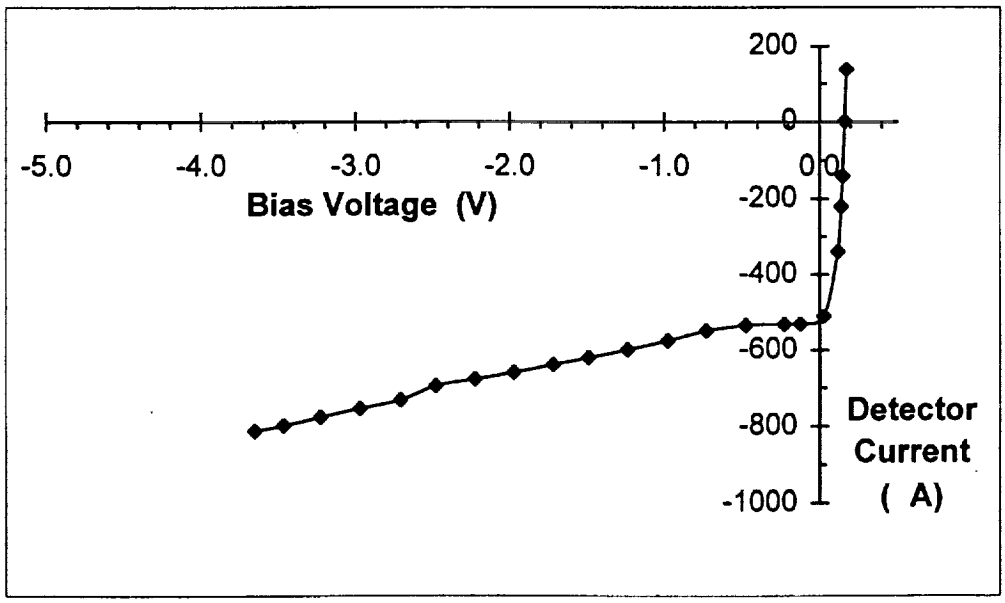

Optical Power=0.75mW

InAs Monitor=573mV

Bias Current Monitor V_{Bi} (mV)	Bias Voltage Monitor V_B (mV)	Detector Voltage V_d (V)	Detector Current I_d (A)	Detector Resistance R_d ( )
492	199	0.183818	295.363	
170	169	0.168948	1.008	64.1
0	150.3	0.158088	-151.512	88.6
-603	50	0.083835	-658.266	414.2
-749	0	0.038809	-755.040	1484.8
-896	-99	-0.057704	-803.427	14751.4
-1061	-255	-0.213238	-812.500	65999.3
-1313	-504	-0.462082	-815.524	69375.7
-1569	-749	-0.706512	-826.613	18515.1
-1863	-1008	-0.963699	-861.895	6699.2
-2148	-1253	-1.206626	-902.218	7539.1
-2431	-1507	-1.459123	-931.452	8273.4
-2710	-1755	-1.705517	-962.702	7321.4
-3011	-2017	-1.965496	-1002.016	7275.6
-3278	-2254	-2.200942	-1032.258	8313.2
-3556	-2504	-2.449491	-1060.484	8935.3
-3831	-2752	-2.696092	-1087.702	9115.4
-4109	-3003	-2.945693	-1114.919	6587.9
-4124	-3016	-2.958590	-1116.935	

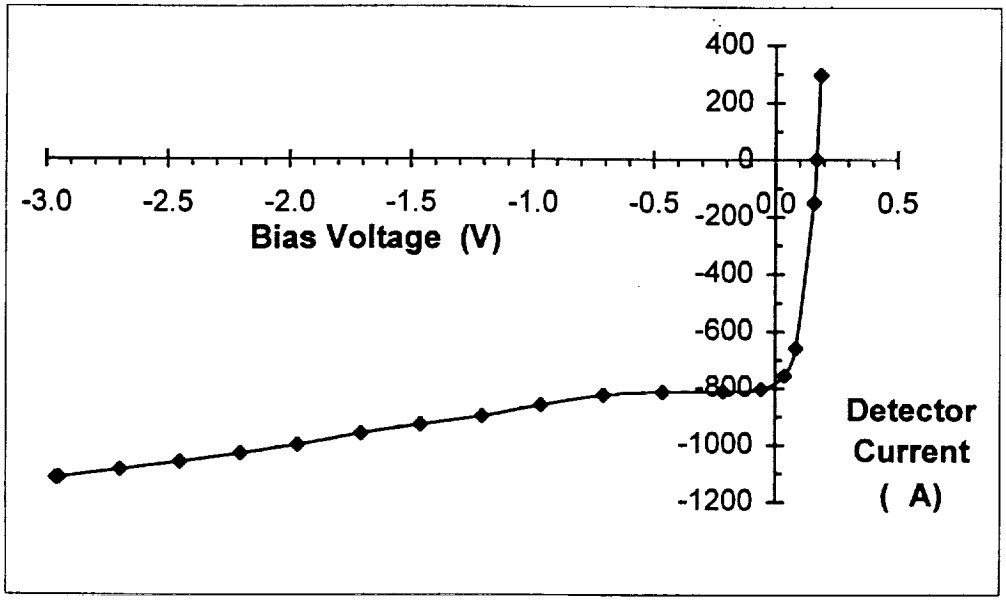

Optical Power=1.0mW

InAs Monitor=748mV

Bias Current Monitor V_{Bi} (mV)	Bias Voltage Monitor V_B (mV)	Detector Voltage V_d (V)	Detector Current I_d (A)	Detector Resistance R_d ( )
363	192	0.18314	172.379	
179	175	0.17479	4.032	51.2
0	158	0.16619	-159.274	63.0
-470	99.7	0.12922	-574.294	150.0
-953	0	0.04938	-960.685	845.9
-1144	-98.3	-0.04412	-1054.133	9975.7
-1309	-250	-0.19513	-1067.540	43041.9
-1464	-402	-0.34697	-1070.565	53458.7
-1766	-699	-0.64371	-1075.605	45109.4
-1942	-864	-0.80814	-1086.694	12040.0
-2112	-1009	-0.95185	-1111.895	5422.8
-2388	-1239	-1.17947	-1158.266	4969.5
-2713	-1511	-1.44872	-1211.694	5388.6
-2990	-1747	-1.68259	-1253.024	5883.2
-3293	-2008	-1.94142	-1295.363	6105.9
-3581	-2256	-2.18735	-1335.685	6318.6
-3871	-2508	-2.43738	-1373.992	6553.2
-4163	-2762	-2.68941	-1412.298	4986.1
-4272	-2850	-2.77632	-1433.468	

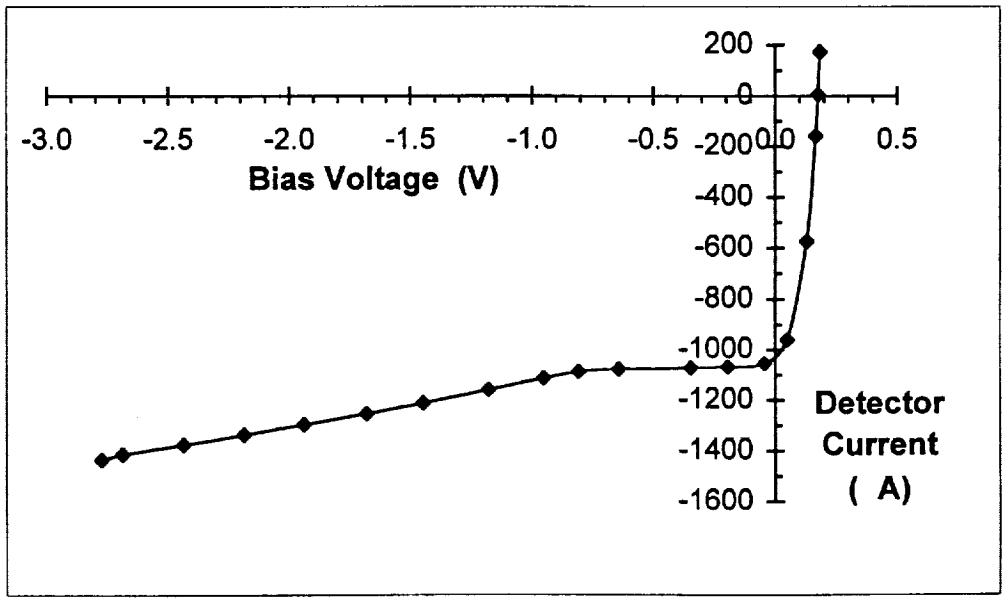

Optical Power=1.1mW

InAs Monitor=940mV

Bias Current Monitor V_{Bi} (mV)	Bias Voltage Monitor V_B (mV)	Detector Voltage V_d (V)	Detector Current I_d (A)	Detector Resistance R_d ( )
137	180	0.182228	-43.347	
1	168.3	0.176969	-168.649	47.7
-599	101.7	0.138006	-706.351	155.5
-1084	-1	0.055115	-1091.734	1317.6
-1240	-96	-0.036724	-1153.226	37747.3
-1406	-258	-0.198517	-1157.258	61948.6
-1646	-495	-0.435361	-1160.282	67471.4
-1928	-764	-0.703688	-1173.387	17143.7
-2219	-1008	-0.945253	-1220.766	4942.2
-2518	-1256	-1.190610	-1272.177	5146.7
-2800	-1495	-1.427382	-1315.524	5817.8
-3090	-1745	-1.675309	-1355.847	5851.2
-3375	-1987	-1.915081	-1399.194	5686.7
-3631	-2206	-2.132164	-1436.492	5687.1
-3974	-2497	-2.420470	-1488.911	5593.0
-4265	-2745	-2.666242	-1532.258	6299.8
-4435	-2893	-2.813102	-1554.435	6201.2
-4513	-2960	-2.879532	-1565.524	

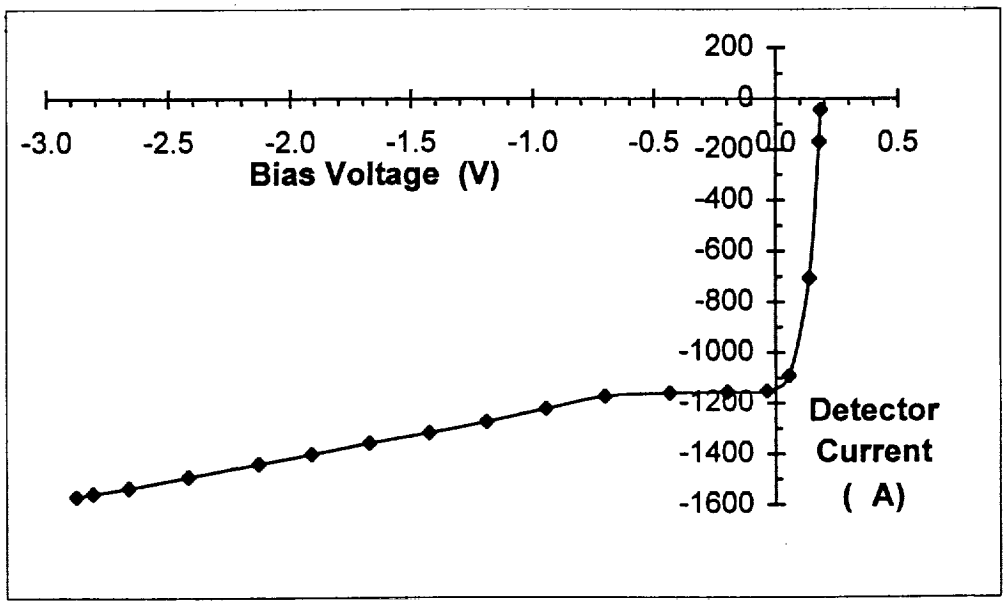

Optical Power=1.50mW

InAs Monitor=720mV

2/20/96

Bias Current Monitor V_{Bi} (mV)	Bias Voltage Monitor V_B (mV)	Detector Voltage V_d (V)	Detector Current I_d (A)	Detector Resistance R_d ( )
405	197	0.186223	209.677	
-17	161	0.170223	-179.435	55.0
-577	98.6	0.133606	-681.048	100.3
-1215	0	0.062955	-1224.798	190.9
-1687	-105	-0.023029	-1594.758	1533.6
-1953	-280	-0.193314	-1686.492	16352.8
-2064	-385	-0.298003	-1692.540	14710.3
-2207	-508	-0.419967	-1712.702	89783.2
-2407	-706	-0.617864	-1714.718	85874.7
-2567	-854	-0.765242	-1726.815	10496.9
-2743	-1010	-0.920205	-1746.976	6583.7
-3002	-1211	-1.118200	-1805.444	2927.8
-3263	-1395	-1.298210	-1883.065	4500.0
-3486	-1584	-1.485449	-1917.339	5039.9
-3680	-1744	-1.643687	-1951.613	4141.7
-4002	-1988	-1.883646	-2030.242	12366.9
-4058	-2040	-1.935438	-2034.274	

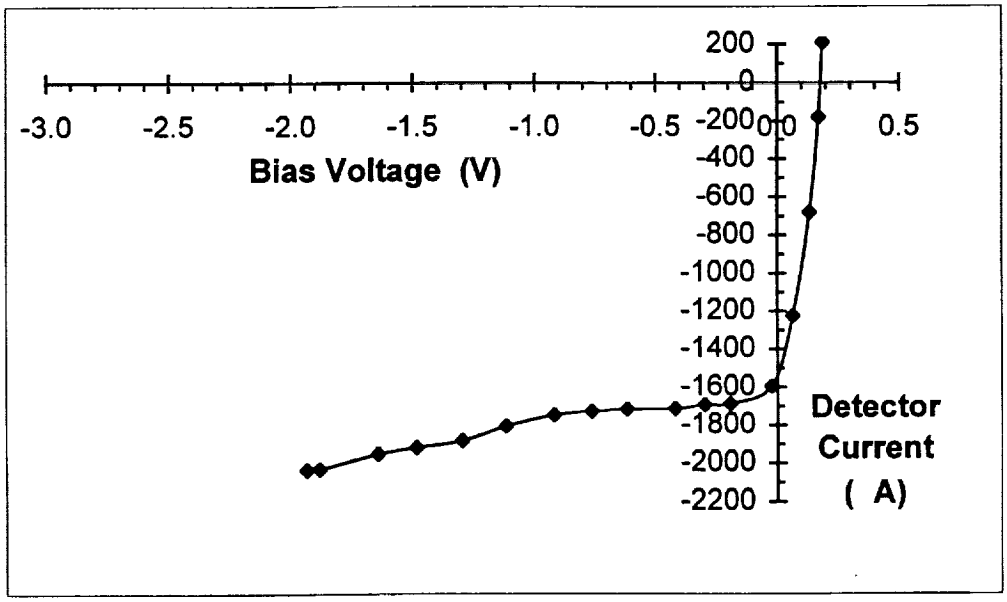

FAMILY OF V-I CURVES

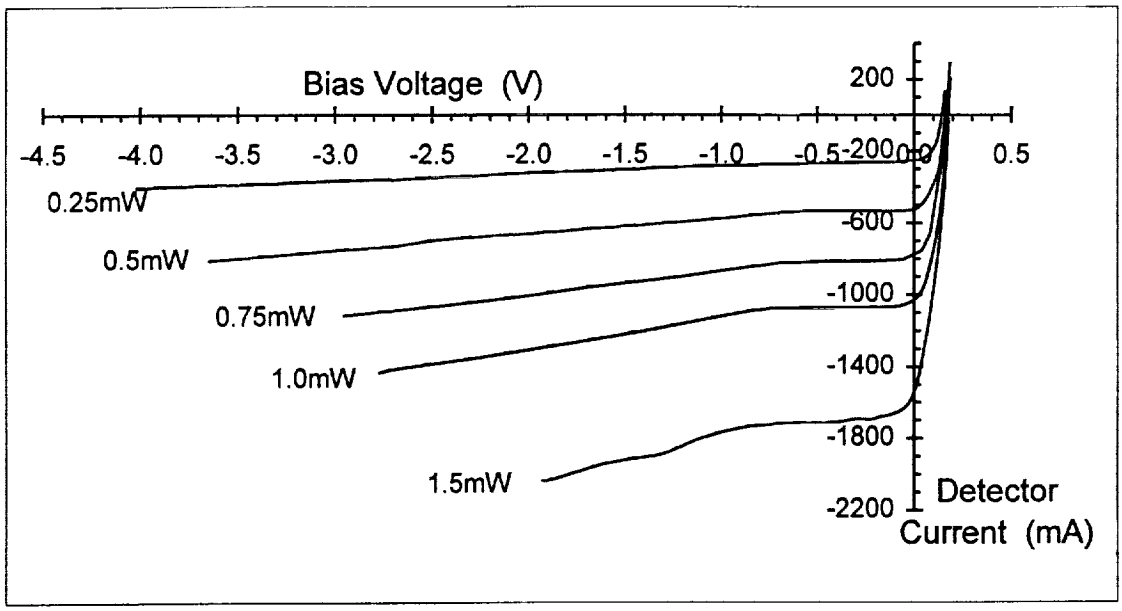

FREQUENCY RESPONSE MEASUREMENTS

VB=0.0

amplifier bias= -2.0mV

Frequency (MHz)	Beam #1 (mV)	Beam #2 (mV)	Het. Sig. (RMS mV)	Frequency Response	Detector RC Model	Het. Qum. Efficiency	RC Model MS Error
0					1.00		
20	138.0	25.3	3.84	1.00	0.978043	0.623401	0.000448
50	138.6	25.6	4.11	1.06	0.895702	0.703372	0.027441
70	138.8	25.6	4.12	1.06	0.823051	0.705795	0.057663
100	139.2	25.3	4.02	1.04	0.713476	0.677408	0.107654
120	139.5	25.4	3.05	0.79	0.64743	0.387693	0.019753
140	138.4	25.4	1.78	0.46	0.588896	0.133082	0.016187
200	138.2	25.6	1.32	0.34	0.454703	0.072759	0.012847
250	135.2	25.6	1.02	0.27	0.378209	0.044395	0.012446
300	135	25.6	0.95	0.25	0.322342	0.038567	0.005449
350	135.6	25.3	0.85	0.22	0.280204	0.031078	0.003261
400	135.6	25.5	0.73	0.19	0.247476	0.022756	0.0032
450	178	14.6	0.6	0.18	0.22141	0.019468	0.00201
500	177	14.9	0.48	0.14	0.200203	0.012307	0.003578
550	247	12	0.43	0.12	0.182636	0.00857	0.004287
600	244.7	12	0.33	0.09	0.16786	0.005095	0.006011
650	277	6.2	0.26	0.09	0.155267	0.004774	0.0046
700	276	6.2	0.23	0.08	0.144411	0.00375	0.004478
750	332	6.2	0.19	0.06	0.134959	0.00213	0.005861
800	331	6.2	0.12	0.04	0.126658	0.000852	0.008049
						MS Error	0.016064

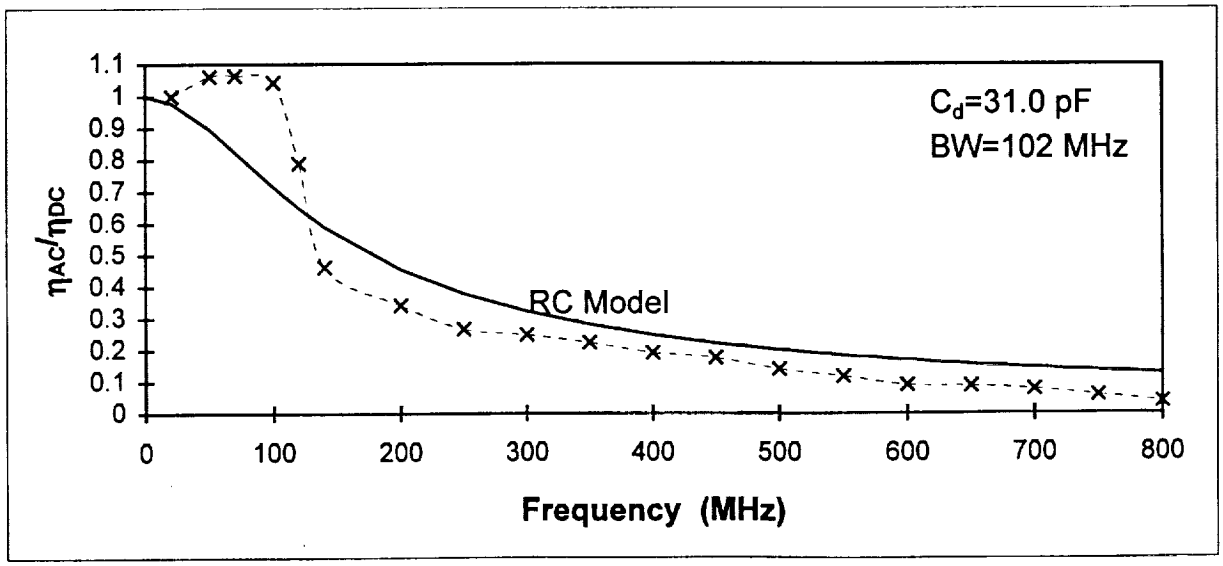

VB=-0.5V

amplifier bias=10.8mV

Frequency (MHz)	Beam #1 (mV)	Beam #2 (mV)	Het. Sig. (RMS mV)	Frequency Response	Detector RC Model	Het. Qum. Efficiency	
0					1.00		
20	154.8	37.4	3.84	1.00	0.991468	0.622034	4.4E-05
50	154.8	37.7	4.26	1.10	0.959152	0.757007	0.020143
70	154.8	37.7	4.3	1.11	0.925827	0.77129	0.034444
145	155.4	37.7	3.93	1.01	0.766539	0.641594	0.061076
150	154.8	38	2.62	0.67	0.755745	0.283183	0.006773
180	154.8	38	2.18	0.56	0.693462	0.196055	0.01772
250	153.7	38	2.21	0.57	0.569923	0.203039	1.01E-07
300	154.6	37.8	2.26	0.58	0.50052	0.212564	0.00688
350	153.7	38	1.84	0.47	0.444082	0.140744	0.000942
400	154	37.8	1.72	0.44	0.397904	0.123636	0.002216
450	197.4	29.7	1.78	0.48	0.359735	0.145165	0.01499
500	194	29.8	1.56	0.43	0.327822	0.112971	0.009513
550	235	24.6	1.1	0.32	0.30084	0.063193	0.000299
600	262	24.8	0.76	0.21	0.277782	0.026538	0.00513
650	256	24.8	0.38	0.10	0.257884	0.006797	0.023578
700	278	22.2	0.2	0.06	0.240561	0.002122	0.033221
750	282	22.2	0.17	0.05	0.225358	0.00151	0.031037
800	311	19.5	0.11	0.03	0.211916	0.000749	0.031432
						MS Error	0.016635

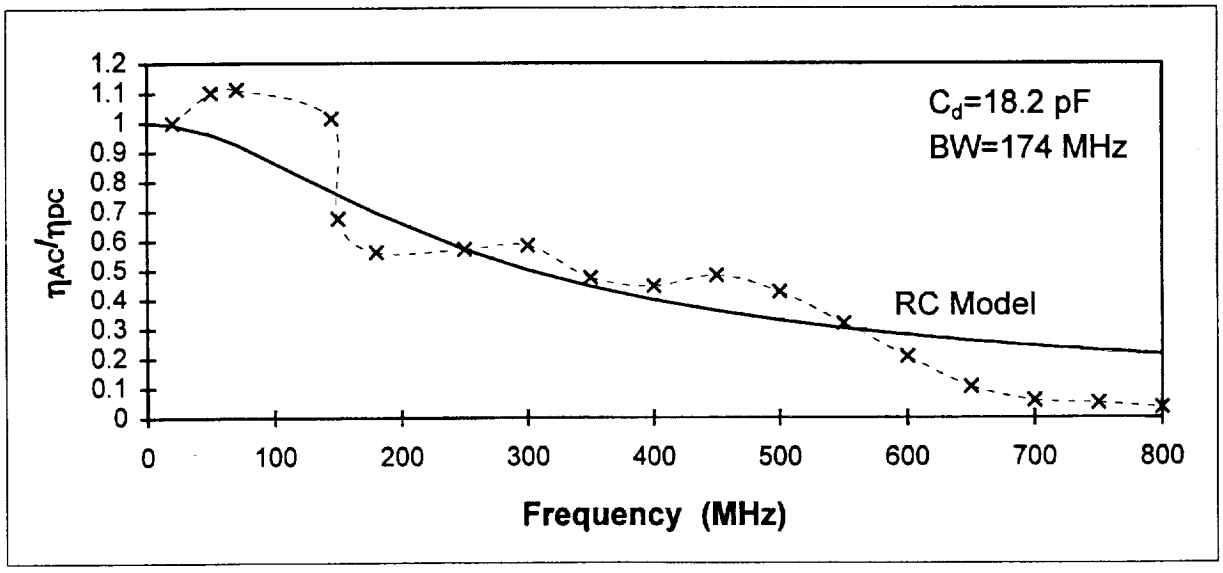

VB=-1.0V

amplifier bias=12.6mV

Frequency (MHz)	Beam #1 (mV)	Beam #2 (mV)	Het. Sig. (RMS mV)	Frequency Response	Detector RC Model	Het. Qum. Efficiency	
0					1.00		
20	205.0	32.3	3.75	0.98	0.996508	0.599497	0.000277
50	206	32.6	4.02	1.04	0.988774	0.675089	0.002604
150	208	32.6	4.01	1.03	0.923135	0.66486	0.011828
250	207	32.6	2.78	0.72	0.823459	0.321188	0.011288
300	254	24.4	2.29	0.69	0.771082	0.297473	0.006537
350	253	24.4	2.2	0.66	0.720426	0.275692	0.00313
400	250	24.4	2.1	0.64	0.672785	0.254373	0.001191
450	246	24.6	2.1	0.64	0.628756	0.254421	9.17E-05
650	332	24.7	2.14	0.55	0.488655	0.191471	0.004238
700	330	24.7	1.8	0.47	0.461416	0.136316	3.4E-05
750	326	24.7	1.6	0.42	0.436694	0.109082	0.000351
800	383	22.8	1.3	0.34	0.414211	0.072279	0.005473
886	384	24.3	1.18	0.29	0.380066	0.051776	0.008483
985	353	24.3	1.12	0.29	0.346658	0.050893	0.003741
1000	354	24.3	1.17	0.30	0.342066	0.055376	0.001959
1050	355	24.3	1.17	0.30	0.327548	0.055214	0.000911
1100	359	24.3	1.33	0.34	0.314144	0.070524	0.000481
1150	356	24.3	1.17	0.30	0.301737	0.055053	2.31E-05
1200	355	24.3	1.3	0.33	0.290226	0.068165	0.001615
1400	161	35	1.07	0.30	0.251512	0.055652	0.002212
1500	165	35	0.96	0.26	0.235663	0.043622	0.000821
1550	164	35	1.07	0.30	0.228441	0.054549	0.004507
1600	165	35	0.9	0.25	0.221635	0.03834	0.000684
1700	166	34.8	0.91	0.25	0.209138	0.039292	0.00174
1750	52	69	0.82	0.28	0.20339	0.048893	0.005843
1850	125	79.6	1.6	0.30	0.192768	0.054928	0.01078
1900	43.8	80.5	0.71	0.25	0.187852	0.038449	0.003636
						MS Error	0.001974

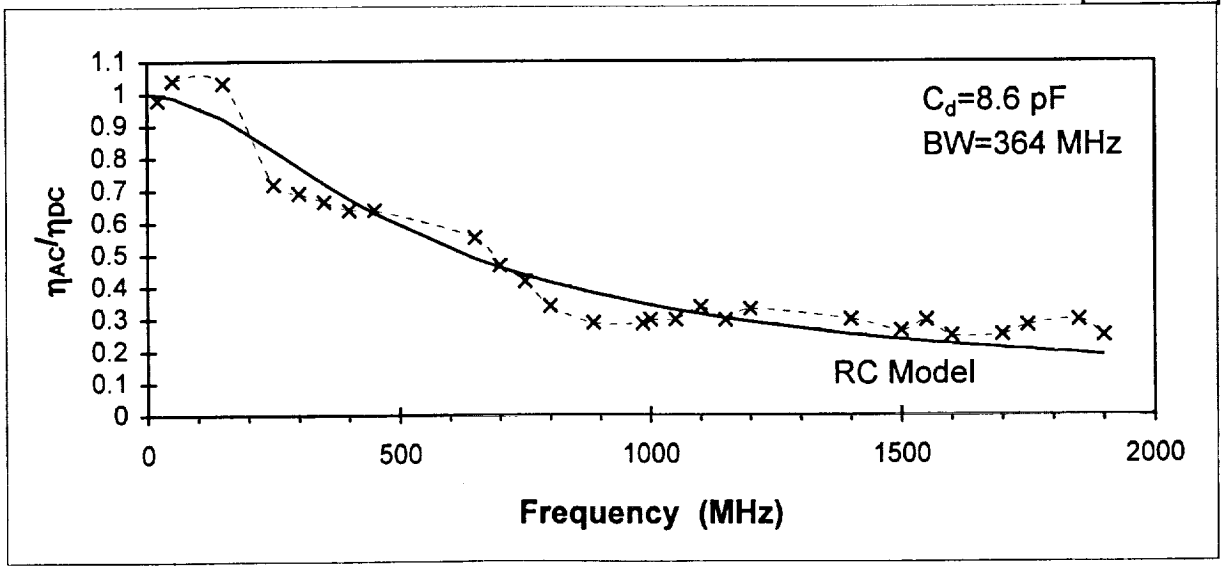

VB=-1.5V

amplifier bias=12.6mV

Frequency (MHz)	Beam #1 (mV)	Beam #2 (mV)	Het. Sig. (RMS mV)	Frequency Response	Detector RC Model	Het. Qum. Efficiency	
0					1		
20	116.3	23.7	2.04	0.97	0.997379	0.589804	0.000907
50	117.2	23.4	2.15	1.03	0.99413	0.66753	0.001218
150	117	23.8	2.14	1.01	0.964696	0.638937	0.001768
190	119.3	23	2.06	0.99	0.946111	0.623858	0.00237
240	119.3	22.8	2.02	0.98	0.918803	0.611628	0.004382
300	120.2	23.2	1.68	0.80	0.881776	0.403691	0.006649
350	118.7	23	1.38	0.67	0.848793	0.281552	0.032578
400	118.7	23.4	1.32	0.63	0.814976	0.248061	0.035225
750	185.8	19.9	1.35	0.61	0.601007	0.23515	9.5E-05
800	185.8	19.5	1.30	0.60	0.576217	0.230695	0.000825
1080	184	32.8	2.00	0.55	0.46294	0.188472	0.00703
1150	186	33.2	1.80	0.48	0.440349	0.147971	0.001948
1350	107	70.8	1.72	0.37	0.385429	0.087844	0.000147
1400	107.4	70.2	1.72	0.37	0.373592	0.088384	7.16E-07
1500	107.2	69.7	1.53	0.33	0.351812	0.070698	0.000287
1600	107.6	69.5	1.56	0.34	0.332267	0.073445	8.21E-05
1700	43.9	83	1.03	0.35	0.314651	0.078543	0.001469
1800	46.2	83	1.03	0.34	0.298709	0.073166	0.001762
1900	46.2	83	1.00	0.33	0.284225	0.068966	0.002165
						MS Error	0.005263

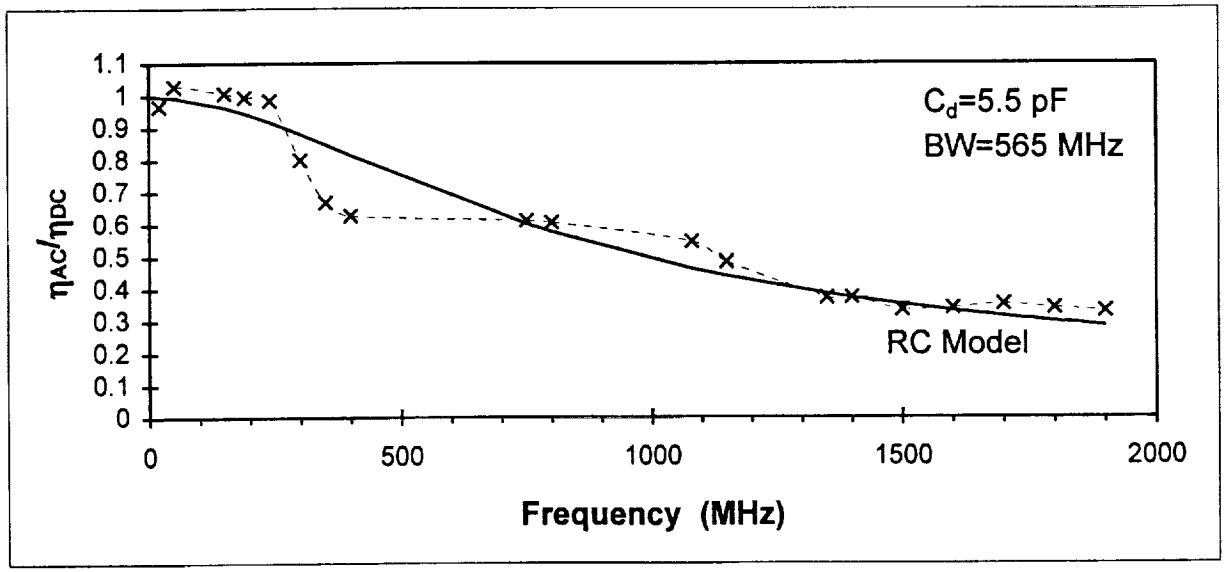

VB=-2.0V
amplifier bias=14.1mV

Frequency (MHz)	Beam #1 (mV)	Beam #2 (mV)	Het. Sig. (RMS mV)	Frequency Response	Detector RC Model	Het. Qum. Efficiency	
0					1		
20	54.0	31.7	1.64	1.00	0.997616	0.660496	4.23E-06
50	54	31.7	1.7	1.03	0.995598	0.709709	0.001324
150	55	32.3	1.77	1.04	0.976968	0.725804	0.004442
300	55	32.2	1.43	0.85	0.921038	0.476363	0.00571
450	54.2	32.2	1.28	0.76	0.845946	0.389282	0.006666
700	47.4	25.5	0.91	0.75	0.714966	0.376185	0.001323
800	47.1	25.1	0.85	0.72	0.666955	0.343241	0.002573
1000	47.4	24.4	0.72	0.63	0.582337	0.260646	0.001854
1100	47.2	24.4	0.69	0.60	0.545709	0.240825	0.003074
1300	47	23.8	0.41	0.37	0.482576	0.090838	0.012853
1400	47.7	90.6	1.3	0.41	0.455431	0.113385	0.001844
1600	25.9	88.7	0.74	0.40	0.408451	0.107278	5.22E-05
1700	25.8	88.7	0.74	0.40	0.388076	0.108195	0.000221
1800	19	89	0.46	0.39	0.369466	0.099427	0.000282
1900	19	89	0.44	0.37	0.352423	0.090969	0.000291
						MS Error	0.002834

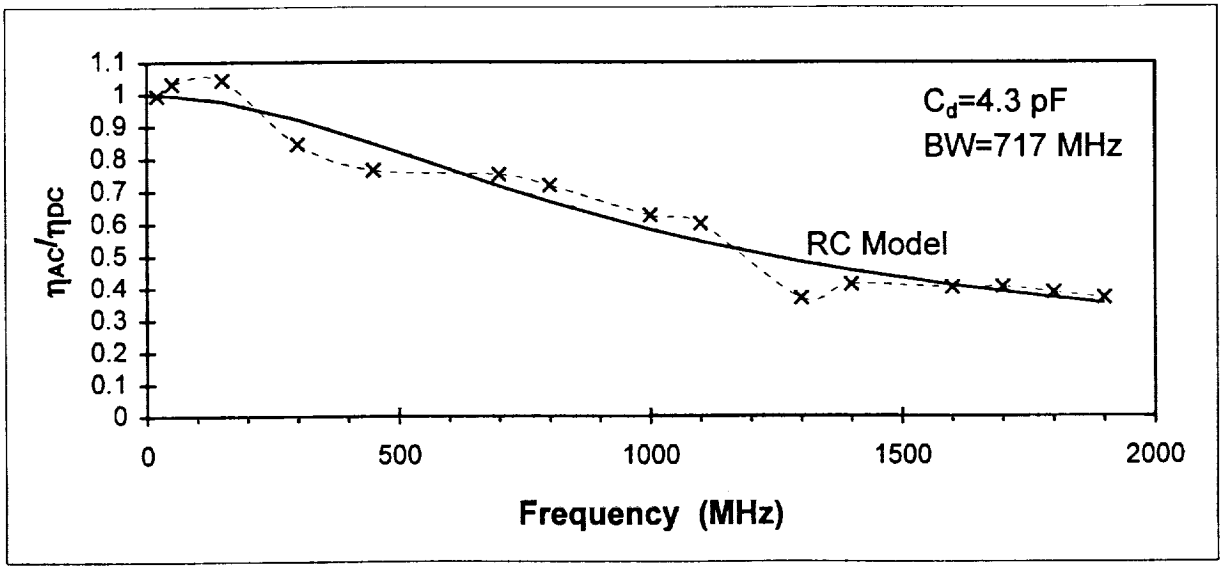

VB=-2.5V

amplifier bias=15.2mV

Frequency (MHz)	Beam #1 (mV)	Beam #2 (mV)	Het. Sig. (RMS mV)	Frequency Response	Detector RC Model	Het. Qum. Efficiency	
0					1		
20	39.9	42.8	1.60	0.99	0.997683	0.647592	0.000141
70	39.8	42.8	1.7	1.05	0.994109	0.734043	0.003071
250	40.6	42	1.42	0.88	0.951515	0.51083	0.005774
300	40.4	42	1.39	0.86	0.933019	0.493358	0.00527
450	40.2	42.8	1.23	0.75	0.867211	0.378119	0.012984
700	49.4	26	0.9	0.75	0.746934	0.378184	4.09E-05
800	56.2	26	0.94	0.72	0.701177	0.344125	0.000304
1000	61.4	19.6	0.62	0.70	0.618491	0.326104	0.006568
1100	61.4	19.8	0.59	0.65	0.581938	0.28247	0.004777
1300	61.4	82.4	1.7	0.49	0.517928	0.160529	0.000736
1400	61.4	81.8	1.6	0.46	0.490039	0.14348	0.000677
1550	38.2	93.2	1.23	0.47	0.452669	0.145431	0.00021
1600	38.5	93	1.2	0.45	0.441284	0.136992	0.000147
1700	38.5	92.7	1.15	0.44	0.41996	0.126301	0.000237
1900	61.5	93.2	1.35	0.36	0.382401	0.087028	0.000442
						MS Error	0.002759

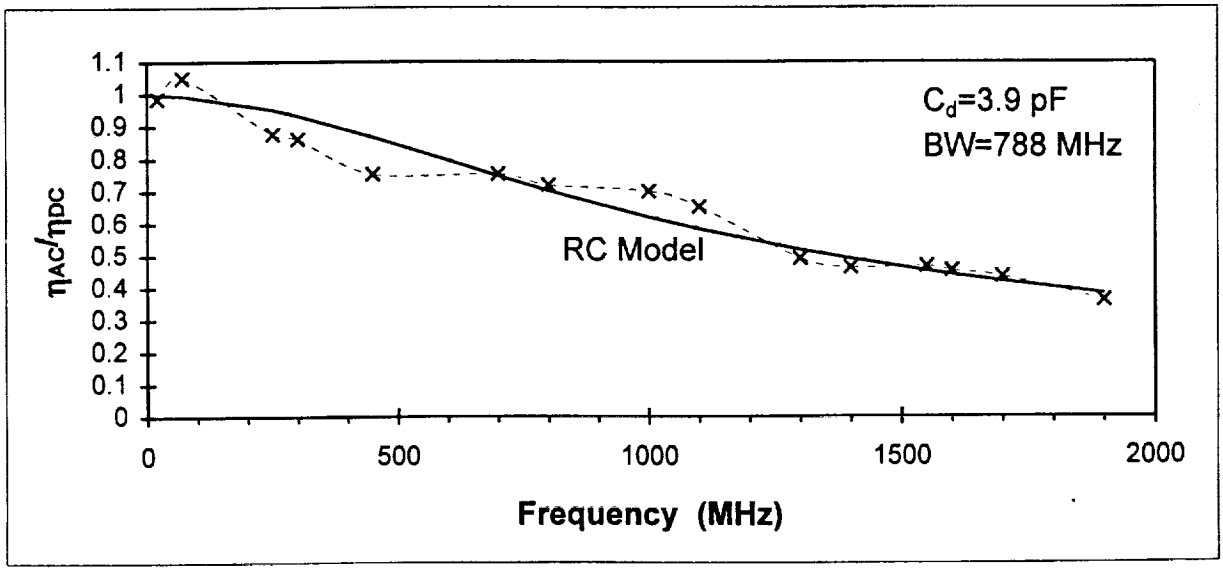

VB=-3.0V

amplifier bias=15.2mV

Frequency (MHz)	Beam #1 (mV)	Beam #2 (mV)	Het. Sig. (RMS mV)	Frequency Response	Detector RC Model	Het. Qum. Efficiency	
0					1		
20	47.4	36.0	1.56	0.97	0.997757	0.68867	0.000788
50	47.9	36	1.72	1.06	0.996472	0.824379	0.004156
150	48.8	35.7	1.66	1.02	0.984476	0.758236	0.00109
250	48.5	36	1.44	0.88	0.961727	0.567412	0.006649
300	49	36	1.44	0.87	0.946971	0.559018	0.005376
700	65	25.8	1.13	0.79	0.788265	0.458461	8.52E-06
750	64.6	25.3	1.08	0.78	0.767188	0.443078	0.000113
800	66.7	24.6	1.02	0.75	0.746424	0.40733	4.41E-07
1050	66.5	23.7	0.86	0.66	0.649945	0.321471	0.000158
1100	66.7	23.7	0.84	0.65	0.632403	0.305502	0.000181
1150	66.7	24	0.84	0.63	0.61548	0.295087	0.000371
1350	67.7	78.4	1.8	0.50	0.55386	0.185076	0.002618
1400	67.7	78	1.78	0.50	0.539907	0.182139	0.001699
1600	57.5	93	1.68	0.47	0.489347	0.162547	0.000333
1700	58.2	93	1.7	0.47	0.466931	0.163731	3.46E-05
1800	41.5	92.7	1.32	0.47	0.44621	0.162021	0.000582
1900	43.4	93	1.33	0.46	0.427032	0.152811	0.000885
						MS Error	0.001473

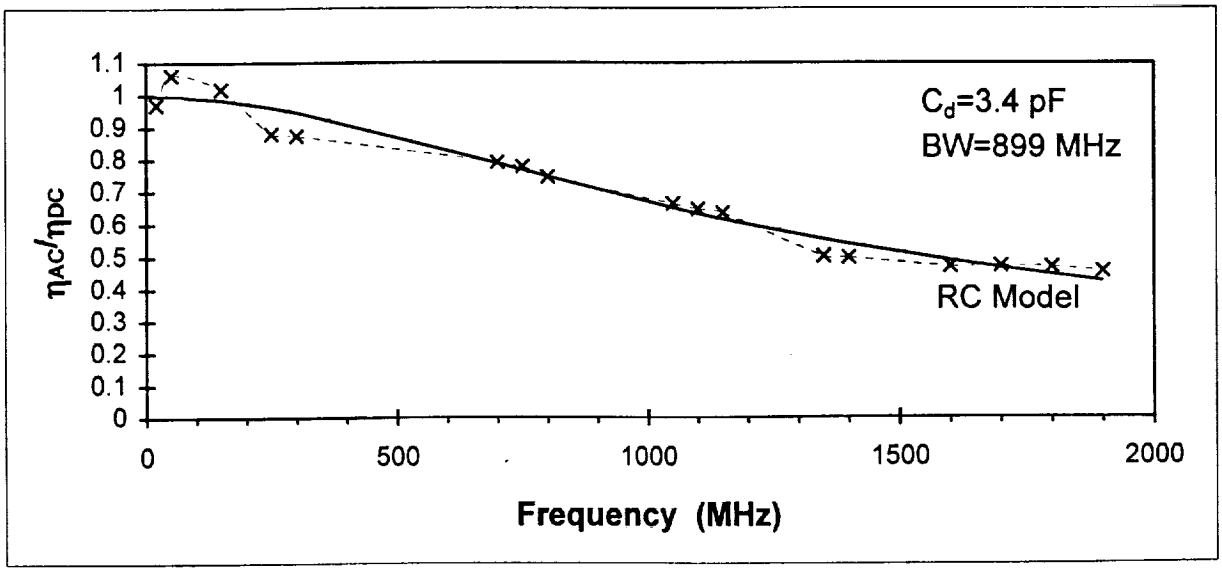

VB=-3.5V

amplifier bias=16.0mV

Frequency (MHz)	Beam #1 (mV)	Beam #2 (mV)	Het. Sig. (RMS mV)	Frequency Response	Detector RC Model	Het. Qum. Efficiency	
0					1		
20	38.9	56.0	1.84	0.98	0.997809	0.717738	0.000393
50	38.9	56.6	2.01	1.06	0.996797	0.843832	0.004049
150	39.3	56.7	2	1.04	0.987312	0.819097	0.003302
250	39.6	56.5	1.72	0.89	0.969124	0.601057	0.005498
300	40	56.5	1.72	0.89	0.957187	0.591039	0.004858
700	47.9	34.5	1.1	0.73	0.821889	0.398152	0.008738
800	60.6	29.5	1.15	0.75	0.784141	0.426533	0.000913
1050	82.2	32	1.49	0.74	0.693913	0.407024	0.001812
1100	82.2	32.2	1.48	0.73	0.677044	0.396621	0.002497
1400	64.7	100	2.02	0.51	0.585862	0.193696	0.006053
1550	64.2	99	2.02	0.51	0.546684	0.198063	0.001084
1600	64.3	99	1.98	0.50	0.534515	0.189903	0.00099
1700	40.4	99	1.54	0.55	0.511433	0.227405	0.001526
1800	41	99	1.55	0.55	0.489929	0.224839	0.003301
1900	40	99	1.54	0.56	0.469889	0.231195	0.007255
						MS Error	0.003485

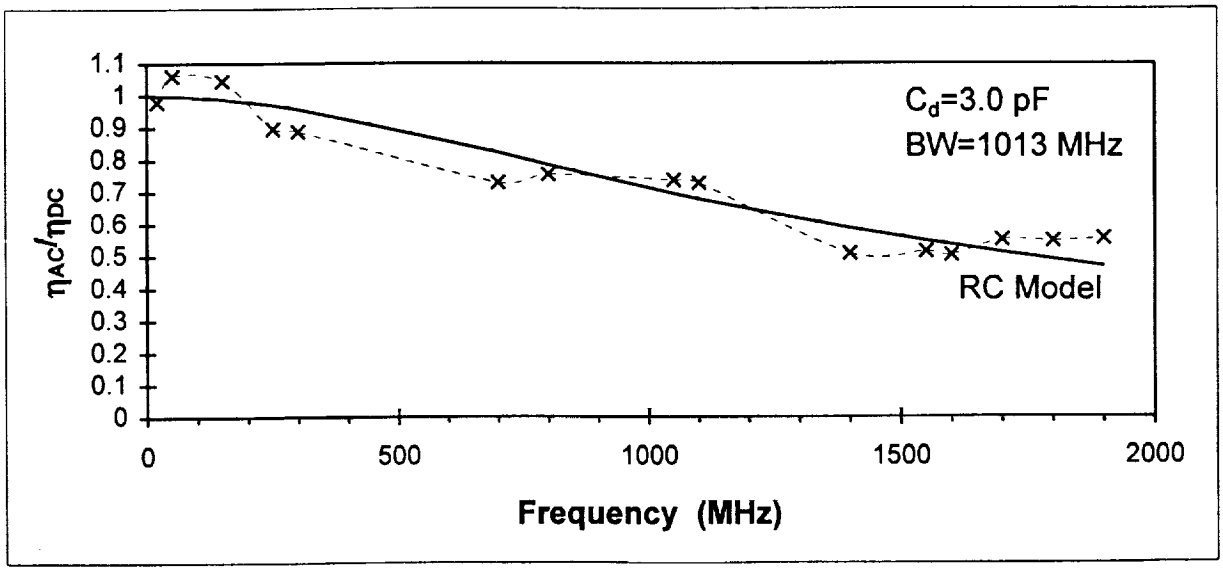

VB=-4.0V

amplifier bias=17.2mV

Frequency (MHz)	Beam #1 (mV)	Beam #2 (mV)	Het. Sig. (RMS mV)	Frequency Response	Detector RC Model	Het. Qum. Efficiency	
0					1		
20	59.7	43.1	2.02	0.98	0.997821	0.760232	0.000338
50	59.9	43.2	2.2	1.06	0.996872	0.89408	0.004262
150	60.3	43	2.1	1.01	0.987971	0.813343	0.00063
200	60.3	43	2.02	0.97	0.980374	0.752554	3.48E-05
300	60.5	43.3	1.84	0.88	0.959597	0.614383	0.006259
450	59.7	43.8	1.78	0.85	0.917286	0.57478	0.004311
700	63	32	1.35	0.83	0.830295	0.551407	1.47E-05
820	62.4	32.8	1.35	0.82	0.786417	0.530074	0.000987
1080	53.8	26.8	0.93	0.80	0.695386	0.504831	0.010556
1250	51.5	24.7	0.64	0.64	0.641487	0.32654	1.72E-07
1330	53.7	55.5	1.36	0.59	0.617926	0.271343	0.001075
1350	51.7	24.7	0.58	0.58	0.612218	0.266629	0.001036
1400	63.5	24.7	0.65	0.56	0.598266	0.249526	0.00138
1500	64.3	24.7	0.61	0.52	0.571702	0.216028	0.00246
1600	65.2	24.9	0.61	0.51	0.546865	0.206471	0.001328
1700	66.7	25	0.62	0.51	0.523666	0.204181	0.000259
1880	37.1	104.5	1.41	0.54	0.485712	0.234695	0.00342
						MS Error	0.002256

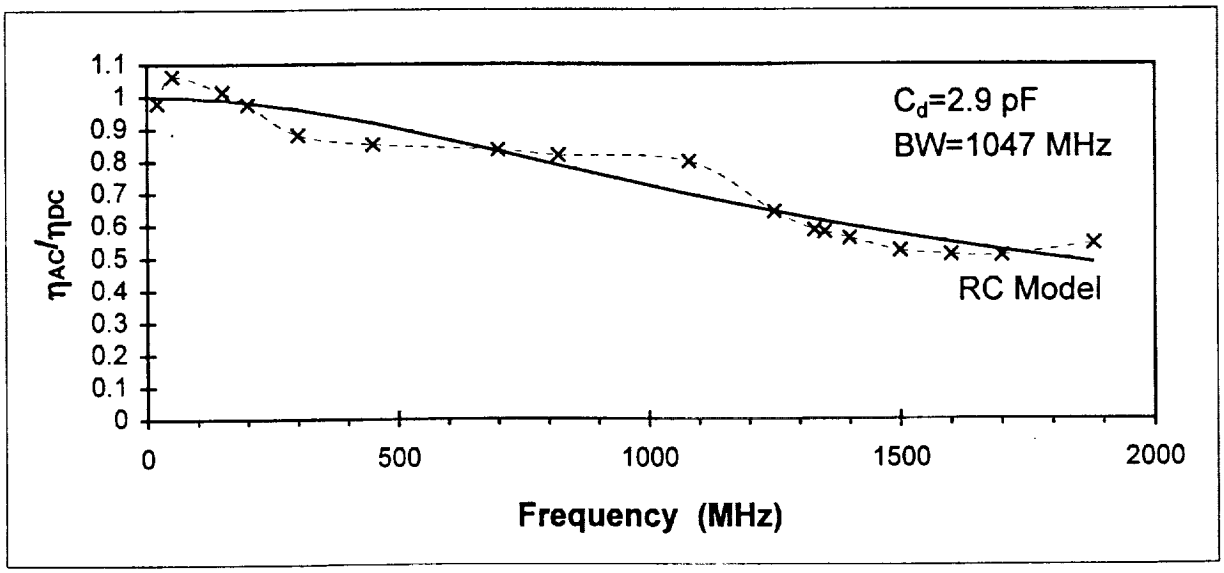

VB=-4.46V

amplifier bias=18.9mV

Frequency (MHz)	Beam #1 (mV)	Beam #2 (mV)	Het. Sig. (RMS mV)	Frequency Response	Detector RC Model	Het. Qum. Efficiency	
0					1		
20	87.8	39.4	2.21	0.95	0.997862	0.725266	0.002694
50	87.6	39.6	2.45	1.05	0.99713	0.885301	0.002304
150	87.8	39.9	2.2	0.93	0.990234	0.701605	0.00358
250	88.6	40	2.06	0.86	0.976859	0.605209	0.012709
300	88.6	40	2.08	0.87	0.967972	0.617017	0.009112
700	60	30	1.15	0.87	0.8611	0.608018	2.53E-05
800	60	30	1.12	0.84	0.829248	0.576709	0.000204
850	59.4	30	1.08	0.82	0.813165	0.544196	3.9E-05
900	59.4	30	1.04	0.79	0.797086	0.504632	6.44E-05
1000	151.2	22.1	1	0.78	0.765207	0.495423	0.000276
1100	59.9	75.8	2.32	0.77	0.734052	0.483911	0.001493
1330	36.6	56.2	1.1	0.66	0.666621	0.357186	7.67E-06
1400	100.9	52.6	1.92	0.59	0.647481	0.279798	0.003592
1550	103.2	52.6	1.86	0.56	0.608783	0.25542	0.002248
1600	103.5	52.8	1.95	0.59	0.596586	0.27809	0.000117
1700	104.3	53.4	2.02	0.60	0.573224	0.290477	0.000647
1850	76.8	108.5	2.7	0.60	0.540668	0.294732	0.003889
1900	76.2	107.5	2.34	0.53	0.530449	0.226219	4.58E-06
						MS Error	0.002389

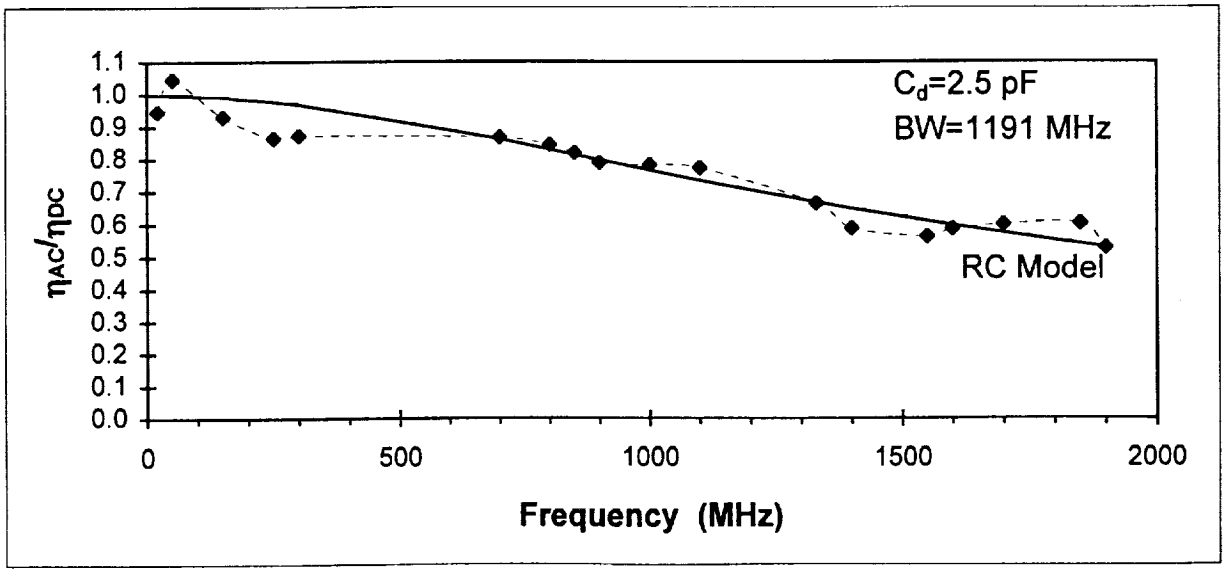

Detector Capacitance

V_B (V)	C_d (pF)
0.0	31.0
0.5	18.2
1.0	8.6
1.5	5.5
2.0	4.3
2.5	3.9
3.0	3.4
3.5	3.0
4.0	2.9
4.5	2.5

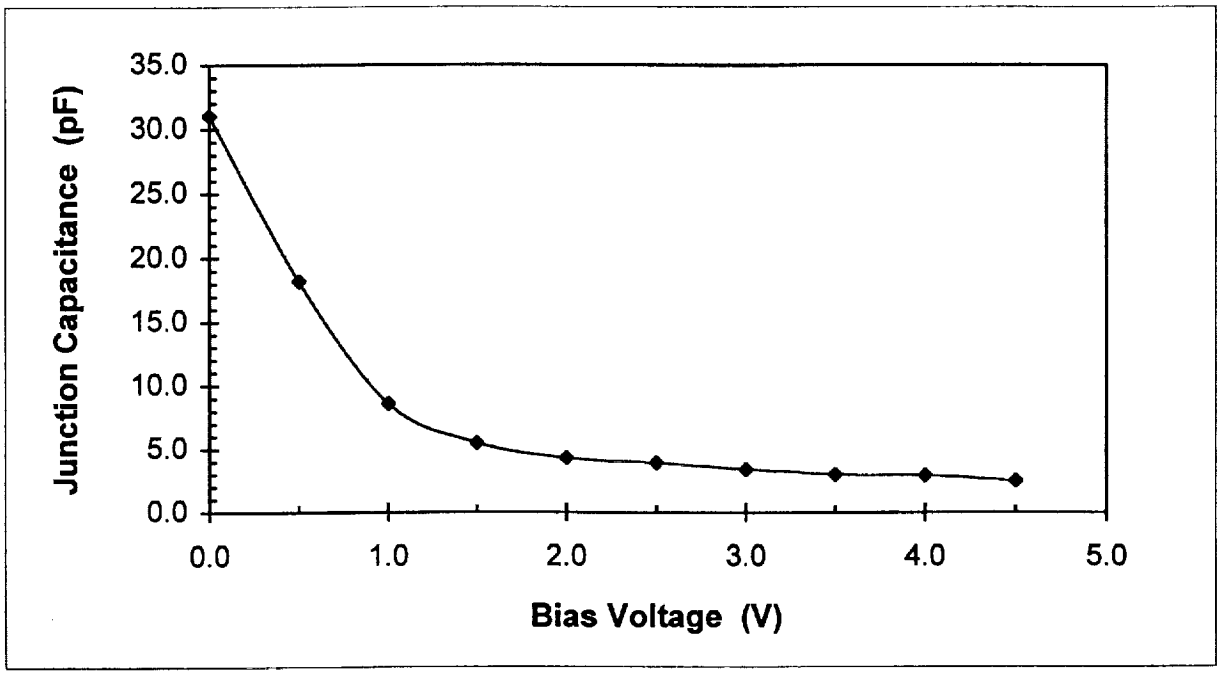

2.6 FIBER OPTIC AND BALANCED DETECTORS HETERODYNE RECEIVERS

The fiber optic and balanced detectors techniques have the potential of improving the robustness of heterodyne receivers and decrease the lidar power consumption. Compared with more conventional technique of coherent mixing of the signal and local oscillator beams using dichroic optical elements, fiber optic technology allows for a less alignment sensitive receiver design. The other advantage of the "fiber optic heterodyne receivers" is their modular design that can provide considerable flexibility in positioning the lidar receiver assembly independently from of the rest of the lidar system (see figure 5). The trade-offs are attenuation in the optical fiber, coupler insertion loss and the signal beam to fiber coupling loss. Maintaining the signal and local oscillator polarizations through the fiber and matching them with each other at the coupler are the main challenges in deigning fiber optic heterodyne receivers.

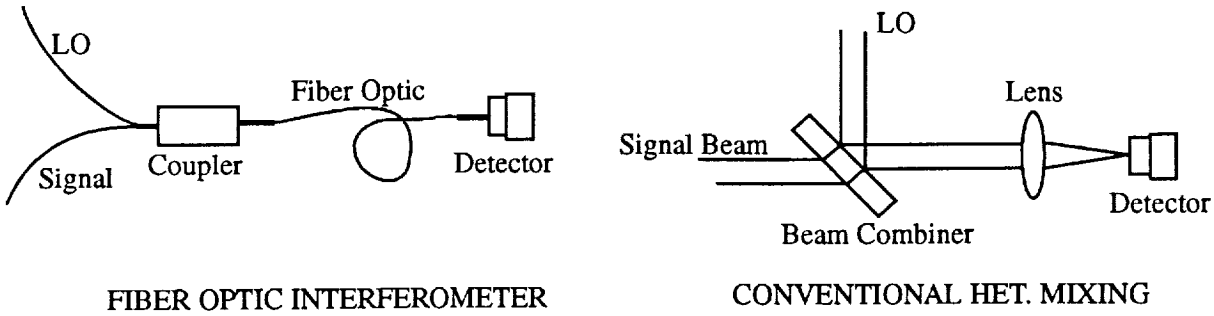

Figure 5. Fiber optic and conventional heterodyne receivers.

A fiber optic receiver measurement assembly has been developed in the detector characterization facility as shown in figure 1. The fiber optic receiver assembly is capable of characterizing the optical fiber transmission properties and the heterodyne mixing efficiencies of fiber optic couplers. A variable coupler has been used to allow the optimum mixing ratio of the signal and local oscillator to be determined experimentally for different detection parameters.

As shown in figure 1, part of each laser beam in the DCF has been split and directed toward the ends of the two optical fibers. The fibers are single mode and polarization maintaining with a core diameter of about 10 μm. The optical fibers direct the beams to a coupler where they are coherently mixed. The output of the coupler is transmitted through another fiber to a InGaAs detector. The detector output is then amplified by a wide bandwidth (1 GHz), DC-coupled amplifier to be measured by a 1GHz digital oscilloscope.

To characterize the fiber optic receivers, first the detector output due to each beam is measured individually. Then the amplitude of the heterodyne signal resulting from mixing of both beams is measured. The measured detector DC signals due to the individual beams are used to specify the optical fibers transmission, the coupler insertion losses and the losses associated with the coupling of the laser beams into the fibers. The measured heterodyne signal then allows to quantify the heterodyne mixing efficiency h_{Hf} of the fiber optic receiver. The receiver heterodyne mixing

efficiency is related to the measured detector output currents by

$$\eta_{Hf} = \frac{\overline{i_h^2}}{2I_{DC1}I_{DC2}} (\eta_{DC}/\eta_{AC})^2 \qquad (23)$$

As can be seen from Eq. (23), these fiber optic receiver measurements require prior knowledge of the detector AC and DC quantum efficiencies and the amplifier gain. The detector AC and DC quantum efficiencies are measured in the DCF as described before. In addition to characterization of fiber optic receivers, this setup allows the optimum mixing ratio of signal and local oscillator beams to be determined experimentally. This will be achieved by changing the mixing ratio, by the variable coupler used in this setup, and measuring the corresponding heterodyne signal. It is planned to initially characterize the standard Silica optical fibers and couplers manufactured for 1.55 μm wavelength, and then the use of fluoride glass fiber materials will be considered if their cost drop to a more reasonable and affordable level for coherent lidar applications.

Using the DCF, balanced detectors receivers will be evaluated in the DCF for use in coherent lidar systems. Figure 6 illustrates the balanced detectors receiver principles. Balanced detectors receivers can improve the lidar SNR by 1.5 dB and reduce the required local oscillator power for optimum heterodyne detection by a factor of 5. However, the balanced detectors can only operate efficiently if the frequency responses of the detectors are well matched and the optical radiation incident on the detectors are 180° out of phase with respect to each other. The beam combiner (splitter), that mixes the local oscillator and signal beams, introduces this 180° phase difference between the optical signals illuminating the detectors. Then by using a single amplifier for amplifying and adding the detectors output currents, the frequency responses of the detectors will be matched if the detectors have identical series resistances and shunt capacitances. An electronic receiver for implementing the balanced detectors technique and characterizing its performance was designed by the UAH personnel and then built be a MSFC engineer. This receiver has two independent bias circuits to provide some adjustment for the detectors frequency responses for matching the phases of the detectors outputs.

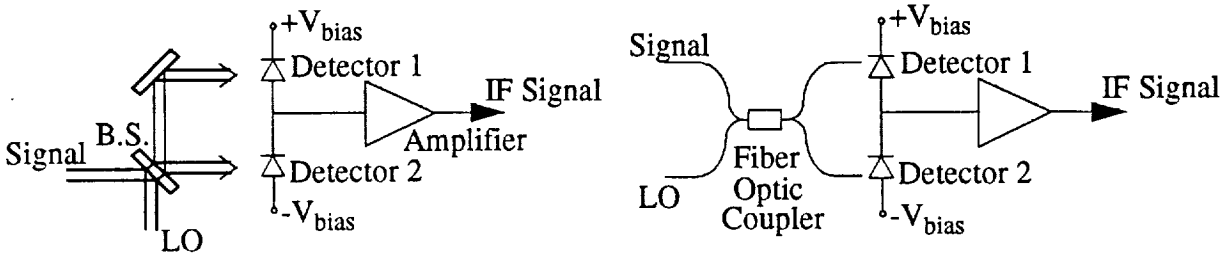

Figure 6. Balanced Detectors heterodyne Receiver.

3.0 HETERODYNE RECEIVER NOISE AND BANDWIDTH

The performance of any heterodyne photoreceiver is established by the operating and intrinsic parameters of the detection device and its interfacing pre-amplifier. Figure 1 shows a typical heterodyne receiver topology where the detector output current is amplified by a transimpedance amplifier. The detector is operated in reverse-biased mode for increased frequency response. The standard transimpedance transfer function of the receiver, that relates the receiver output voltage to the detector generator current, is given by:

$$H_T(\omega) = \frac{v_{out}}{i_{in}} = \frac{-\left(\frac{A_v}{1+A_v}\right)R_f}{1+j\omega R_f\left(C_f+\frac{C_{in}}{1+A_v}\right)} \qquad (1)$$

where A_v the amplifier open-loop gain, R_f and C_f are the feedback resistance and capacitance, and C_{in} is the combined amplifier input capacitance and the detector junction capacitance.

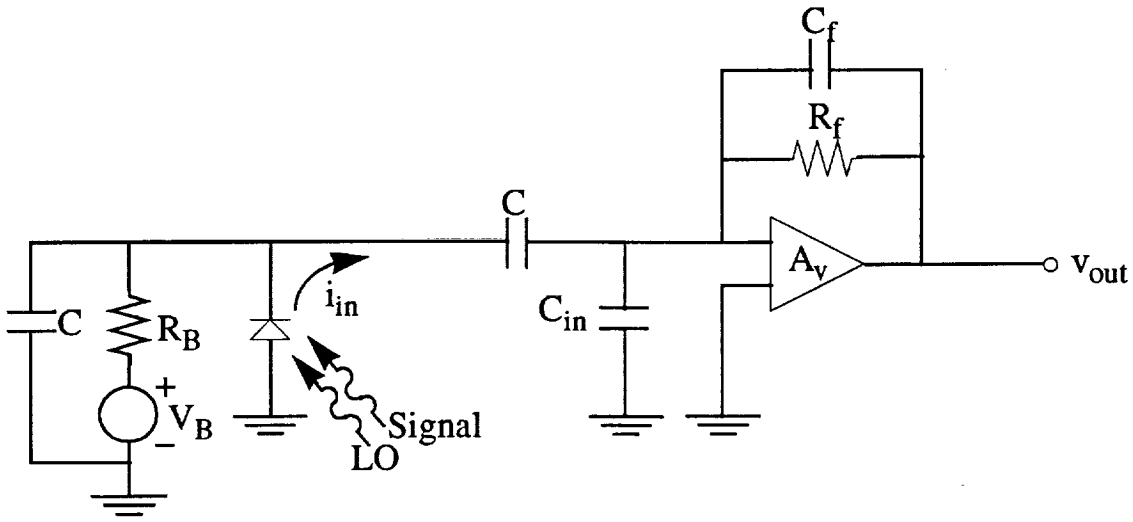

Figure 1. The Optical Heterodyne Receiver Topology.

In the past, several critical detector and preamplifier parameters have been neglected that can play very important role in performance of heterodyne photoreceivers particularly for wider bandwidth. These parameters include the detector nonlinearity and series resistance and the preamplifier feedback loading. In this section, the analytical formulations defining the performance of heterodyne receivers are derived and described by including all the noise sources that can influence the optimum design of a heterodyne receiver. Then the optimum operating parameters of 2-micron heterodyne receivers are determined using the actual detector parameters measured in the DCF for different types of preamplifiers.

3.1 TRANSIMPEDANCE TRANSFER FUNCTION

The performance of photoreceivers are best described by their Transimpedance Transfer Function (TTF). The TTF simply relates the output voltage of the detector preamplifier to the current generated by the detector upon illumination of an optical radiation (Eq. (1)).

An equivalent circuit representation of the detector/preamplifier utilizing a FET front end transimpedance amplifier is shown in figure 2(a). In many real world applications conventional operational amplifiers are used in a transimpedance mode as the detector preamplifier. In figures 2(b) and 2(c) the two types of operational amplifiers, i.e., voltage feedback and current feedback amplifiers, are depicted. For most PIN detectors, including InGaAs detectors, the detector shunt resistance R_d can be neglected since $R_d >> R_s, R_f, R_{in}, R_o$.

The transimpedance transfer functions for all three amplifiers are very similar. Let us first consider the model of figure 2(a). The current flowing into the amplifier feedback is given by:

$$i_f = \frac{(v_i - v_{out})}{R_f / (1 + j\omega R_f C_f)} \tag{2}$$

The amplifier output voltage is equal to

$$v_{out} = -(g_m v_i - i_f) \frac{R_o}{1 + j\omega R_o C_{out}} \tag{3}$$

Substituting Eq. (1) in Eq. (2), the amplifier input voltage can be written as

$$v_i = \frac{[R_o (1 + j\omega R_f C_f) + R_f (1 + j\omega R_o C_{out})]\, v_{out}}{-g_m R_o R_f + R_o (1 + j\omega R_f C_f)} \tag{4}$$

Using the basic Kirchhoff's current law, we can write

$$i_{in} = i_f + v_i (j\omega C_{in}) + ((i_f + v_i (j\omega C_{in}))\, R_s + v_i)\, (j\omega C_d) \tag{5}$$

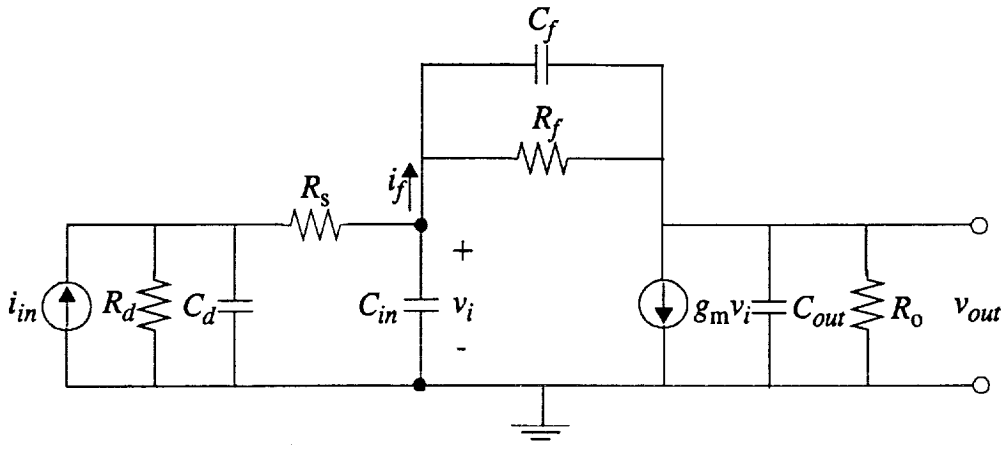

(a) Transimpedance Amplifier Model.

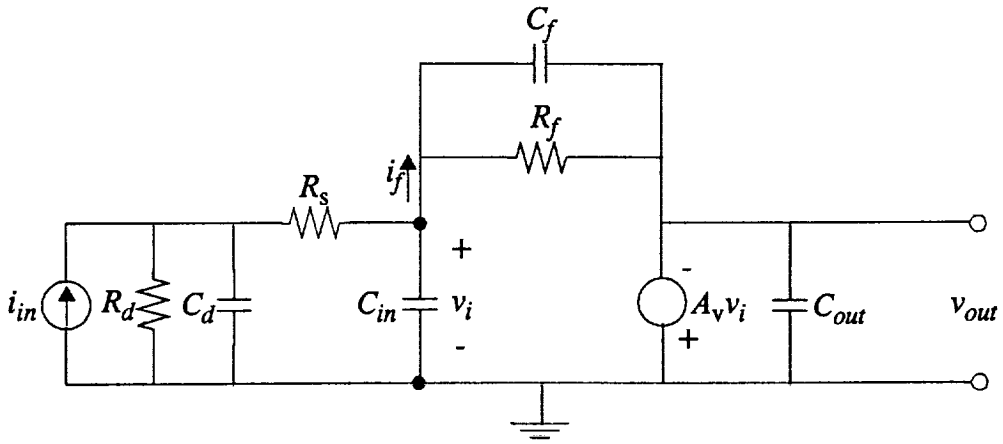

(b) Voltage Feedback Operational Amplifier.

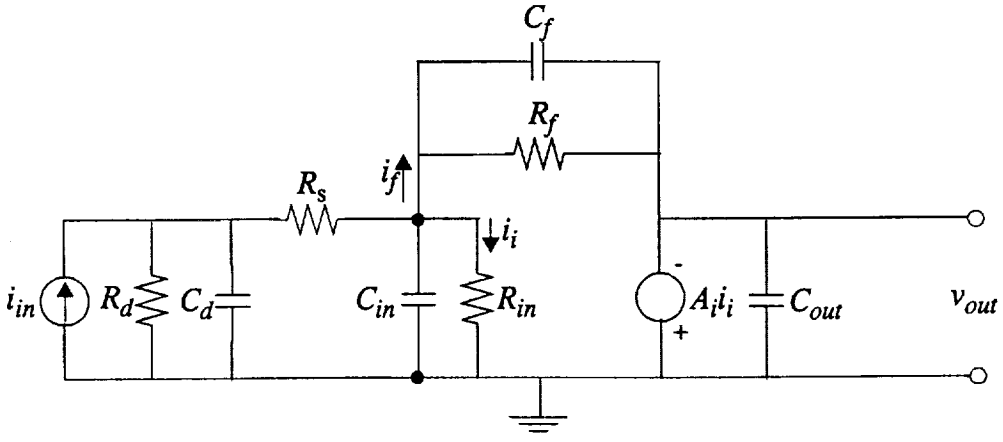

(c) Current Feedback Operational Amplifier.

Figure 2. Equivalent circuit representations of detector/preamplifier.

Substituting Eq. (1) and Eq. (3) in Eq. (4), the amplifier input current can be written in terms of the amplifier output voltage.

$$i_{in} = -\frac{(1+j\omega R_f C_f)\,(1+j\omega R_s C_d)\,v_{out}}{R_f} + \frac{[R_o(1+j\omega R_f C_f) + R_f(1+j\omega R_o C_{out})]}{-g_m R_o R_f + R_o(1+j\omega R_f C_f)} \left[\frac{(1+j\omega R_f C_f)\,(1+j\omega R_s C_d)}{R_f} + j\omega(C_{in}+C_d) + (j\omega)^2 R_s C_{in} C_d\right] v_{out} \tag{6}$$

Since the amplifier transconductance is greater than the feedback network transmission, that is

$$g_m \gg \frac{1+j\omega R_f C_f}{R_f} \tag{7}$$

the expression above can be greatly simplified and the Transimpedance Transfer Function (TTF) can be written in as:

$$H_T(\omega) = \frac{-A_0 R_f}{B + j\omega C + (j\omega)^2 D + (j\omega)^3 E} \tag{8}$$

where:

$$B = 1 + A_0$$

$$C = R_f(C_{in} + C_d + (1+A_0)C_f) + R_s C_d + 1/\omega_0$$

$$D = R_f R_s C_d (C_{in} + (1+A_0)C_f) + R_f(C_{in} + C_d + C_f)/\omega_0 + R_s C_d/\omega_0$$

$$E = R_f R_s C_d (C_{in} + C_f)/\omega_0$$

and

$$A_0 = g_m\left(\frac{R_o R_f}{R_o + R_f}\right)$$

$$\omega_0 = \frac{R_o + R_f}{R_o R_f (C_{out} + C_f)}$$

A_0 and ω_0 define the amplifier open-loop gain given by

$$A_v = \frac{A_0}{1 + j\omega/\omega_0} \tag{9}$$

where A_0 is the amplifier DC open-loop gain and ω_0 is its open-loop 3dB frequency response. Eq. (8) is a complete form of the TTF which includes the effect of the feedback loading[10] and the effect of the detector series resistance.

Similarly, the TTF can be obtained for voltage and current feedback operational amplifiers operating in transimpedance mode. For the Voltage Feedback (VF) operational amplifier, shown in figure 1(b), the TTF is basically identical to Eq. (8). The only differences are the expressions for the open-loop gain and 3 dB frequency response (A_0 and ω_0). For the VF operational amplifier, A_0 and ω_0 are usually provided by the manufacturer.

The TTF for CF operational amplifier is also similar to Eq.(8). Using figure 1(c) and the Kirchhoff's current law, the detector current can be written as

$$i_{in} = (i_f + i_i + j\omega C_{in} i_i)(1 + j\omega R_s C_d) + j\omega C_d R_{in} i_i \qquad (10)$$

Using the equality $v_{out}=-Z_i i_i$ and after some simple algebraic manipulations, the TTF for CF operational amplifier can be written in the same form as Eq.(8) but with different coefficients in the denominator. For CF operational amplifier, the coefficients in the denominator are given by:

$$\begin{aligned} B &= 1 + A_0 + R_f/R_{in} \\ C &= R_f(C_{in} + C_d + (1 + A_0)C_f) + R_s C_d(1 + A_0 + R_f/R_{in}) + (1 + R_f/R_{in})/\omega_0 \\ D &= R_f R_s C_d(C_{in} + (1 + A_0)C_f) + R_f(C_{in} + C_d + C_f)/\omega_0 + R_s C_d(1 + R_f/R_{in})/\omega_0 \\ E &= R_f R_s C_d(C_{in} + C_f)/\omega_0 \end{aligned} \qquad (10)$$

where $A_0 = \dfrac{Z_0}{R_{in}}$, and Z0 is the amplifier open-loop gain.

It should be noted that Z_0 is the open-loop current gain for a current-controlled voltage source while for VF operational amplifiers, A_0 refers to the open-loop voltage gain. For all three types of amplifiers A_0 is unit-less. As can be seen for the expressions of Eq.(10), the TTF for the CF operational amplifier is identical to those of transimpedance and VF operational amplifiers when $R_f >> R_{in}$.

Figure 3 shows the normalized magnitude squared of TTF's for each of the amplifier types using measured data of a 75 micron diameter detector (see section 2.5) and actual parameters of a VF operational amplifier, a CF operational amplifier, and a 2 GHz MESFET transimpedance amplifier (see section 3.5). The effect of the series resistance on the TTF's is clear for wider bandwidths, or smaller feedback resistances. As shown in figure 3, the detector series resistance causes the receiver gain to peak and then drop faster with frequency. Figure 3 also illustrates that the last quantity in the denominator of Eq.(8) has a small effect on the TTF and may be neglected. This fact is illustrated by setting the quantity E equal to zero in the TTF expression. Neglecting the third power of frequency in the TTF expression will greatly simplify the receiver noise and bandwidth analyses.

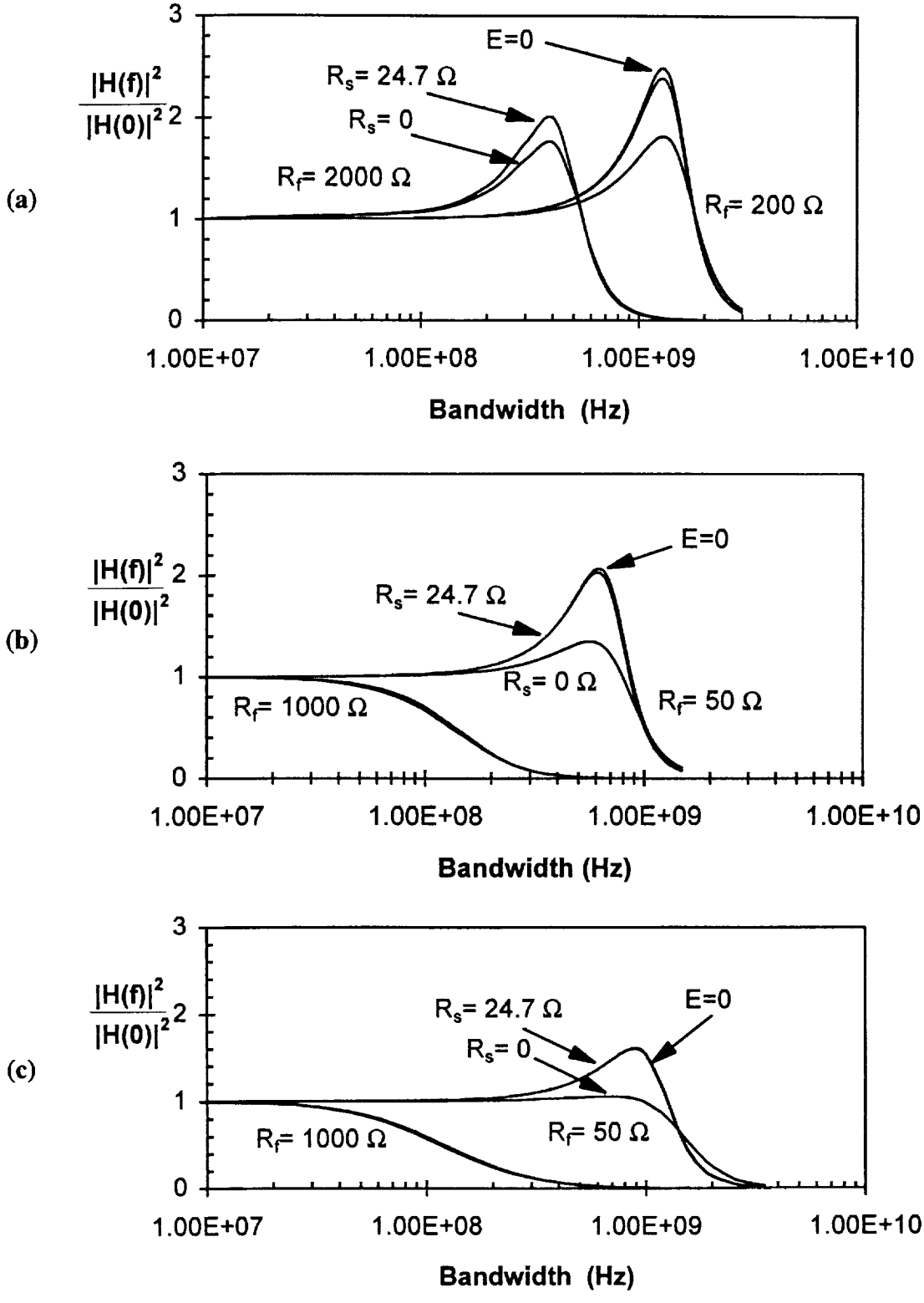

Figure 3. Transimpedance Transfer Function. (a) MESFET 2 GHz Transimpedance Amp. (b) VF Operational Amp. CLC 425 (c) CF Operational Amp. CLC 449.

The 3 dB bandwidth of the receiver can be found by solving the following equation:

$$\frac{\left|H_T(\omega_{3dB})\right|^2}{\left|H_T(0)\right|^2} = \frac{1}{2} \tag{11}$$

Then substituting Eq. (8) in the equation above gives:

$$D^2\omega_{3dB}^4 + (C^2 - 2BD)\,\omega_{3dB}^2 - B^2 = 0 \tag{12}$$

Solving for ω_{3dB}, the receiver bandwidth can be expressed as:

$$f_{3dB} = \left(\frac{1}{2\pi}\right)\left[\frac{-(C^2 - 2BD) + \sqrt{C^4 - 4BC^2D + 8B^2D^2}}{2D^2}\right]^{\frac{1}{2}} \tag{13}$$

For a given detector and an amplifier, the receiver bandwidth is set by the amplifier feedback resistance. Figure 4 shows the bandwidth as a function of feedback resistance for the same amplifiers and the detector of figure 3.

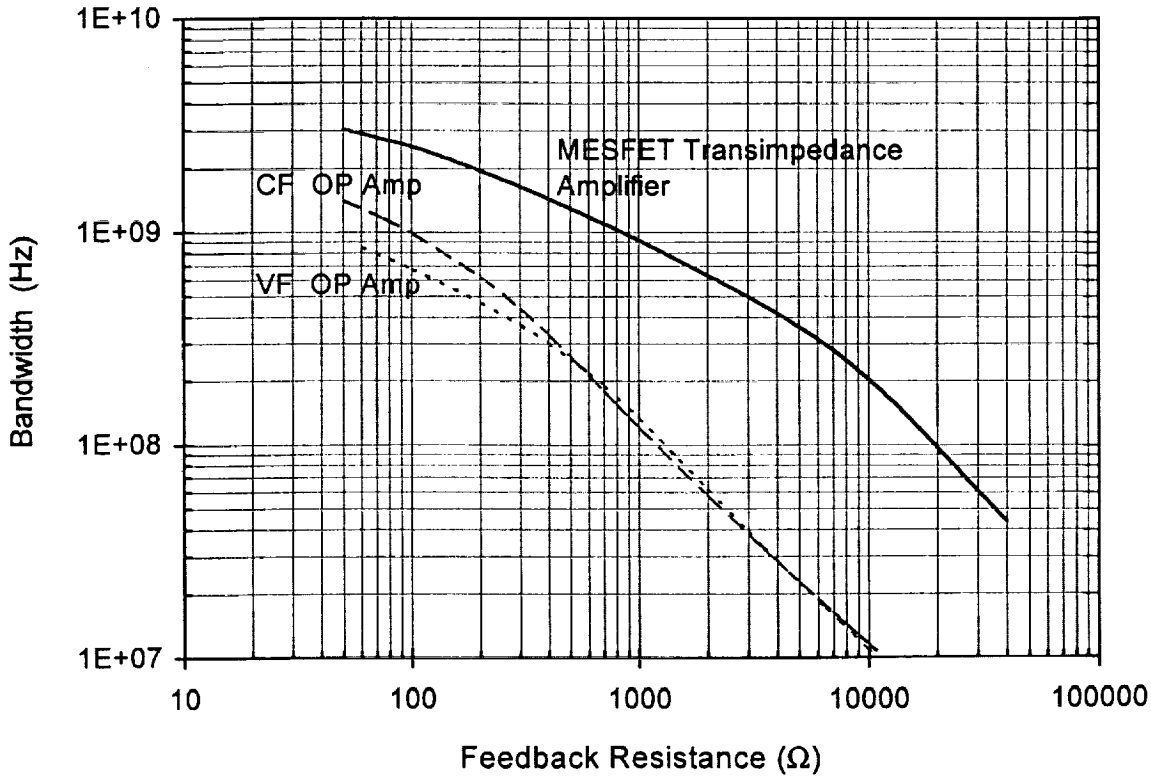

Figure 4. Receiver bandwidth as a function of feedback resistance.

3.2 NOISE ANALYSIS

The major noise sources for a heterodyne receiver are the detector shot noise, dark current noise, amplifier input noise voltage and input noise current, and amplifier feedback resistor thermal noise. The receiver noise model is shown in figure 5 with all the major noise sources specified.

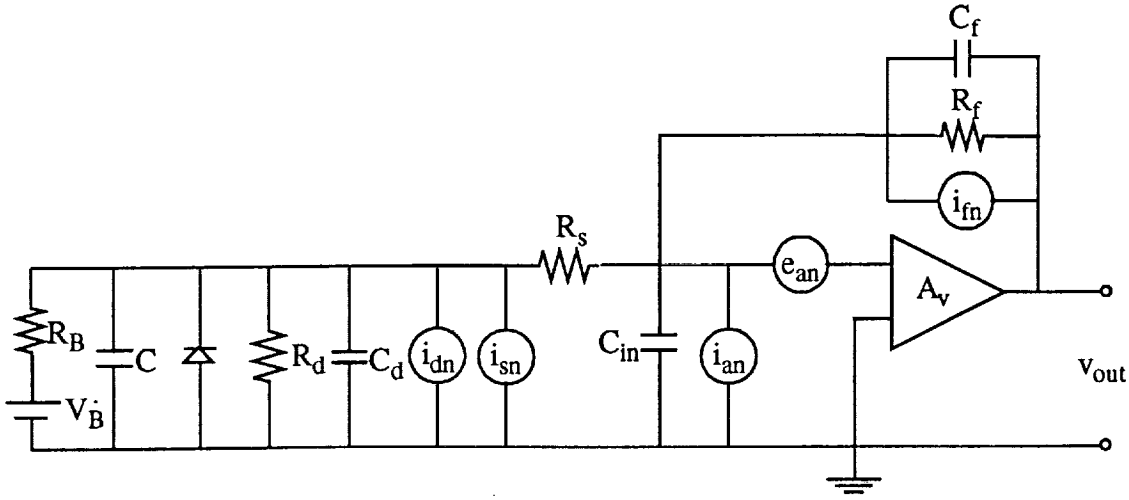

Figure 5. Receiver lumped parameter model with noise sources.

The detector shot (quantum) noise and dark current noise spectral densities are given by

$$\langle i_{sn}^2 \rangle = 2e\rho I_{LO} = 2e\rho P_{LO}(1 - \alpha P_{LO}) \tag{14}$$

$$\langle i_{dn}^2 \rangle = 2e\rho I_B \tag{15}$$

where ρ and α are the detector responsivity and nonlinearity coefficient, P_{LO} is the applied local oscillator power, and I_B is the detector bias current. The Johnson (thermal) noise contribution due to the amplifier feedback resistor is equal to

$$\langle i_{fn}^2 \rangle = \frac{4KT_e}{R_f} \tag{16}$$

where R_f is the feedback resistance, T_e is its effective temperature and K is Boltzmann's constant. For off-the-shelf amplifiers, the amplifier input current noise i_{an} and input voltage noise e_{an} are usually provided by the manufacturer, otherwise they can be either measured or determined analytically if the amplifier circuit parameters are known. The total spectral density of the input noise of the amplifier is given by

$$S_i(f) = \langle i_{sn}^2 \rangle + \langle i_{dn}^2 \rangle + \langle i_{fn}^2 \rangle + \langle i_{an}^2 \rangle + \langle e_{an}^2 \rangle \left| \frac{1 + j2\pi f R_f (C_{in} + C_f)}{R_f} \right|^2 \tag{17}$$

where the last term is the equivalent noise current spectral density of the amplifier input noise voltage. The total noise referred to the input is obtained by integrating the total current noise spectral over the normalized receiver TTF magnitude squared.

$$\langle i_N^2 \rangle = \int_0^\infty S_i(f) \frac{|H_T(f)|^2}{|H_T(0)|^2} df \tag{18}$$

Substituting Eq.(17) in Eq.(18), the total noise power is obtained to be

$$\langle i_N^2 \rangle = \left(2e\rho P_{LO}(1 - \alpha P_{LO}) + 2e\rho I_B + \frac{4KT_e B_e}{R_f} + \langle i_{an}^2 \rangle + \frac{\langle e_{an}^2 \rangle}{R_f} \right) \int_0^\infty \frac{|H_T(f)|^2}{|H_T(0)|^2} df$$
$$+ (2\pi)^2 (C_{in} + C_f)^2 \langle e_{an}^2 \rangle \int_0^\infty \frac{|H_T(f)|^2}{|H_T(0)|^2} f^2 df \tag{19}$$

Using complex contour integration and residue theory, the integrals over the transimpedance transfer function can be evaluated[10] and expressed as

$$\int_0^\infty \frac{|H_T(f)|^2}{|H_T(0)|^2} df = \frac{B}{4C} \tag{20}$$

$$\int_0^\infty \frac{|H_T(f)|^2}{|H_T(0)|^2} f^2 df = \frac{B^2}{16\pi^2 CD} \tag{21}$$

where B, C and D are provided in Eqs. (8) and (10). The first integral is proportional to the receiver bandwidth and the second integral increases almost as bandwidth to the third power.

As noted earlier, the amplifier input current noise and input voltage noise powers ($<i^2_{an}>$ and $<e^2_{an}>$) are usually provided by the manufacturer for more standard VF and CF operational amplifiers. They may also be measured using standard spectrum analyzers or digitizing

oscilloscopes. The input noise current can be measured by using a large source resistance and the input noise voltage can be measured by using a small source resistance. However for wide bandwidth applications which require a bipolar junction transistor or a field effect transistor amplifier optimized for interaction with a specific detector, it is necessary to express the input current and voltage noises in terms of the amplifier circuit parameters for optimizing the receiver design. For a FET front-end amplifier, the input current and voltage noise powers are given by[11,12]

$$\langle i_{an}^2 \rangle = 2eI_{gate} \tag{22}$$

$$\langle e_{an}^2 \rangle = \frac{4KT_e\Gamma}{g_m} + \frac{4KT_e}{g_m^2 R_L} \tag{23}$$

where I_{gate} is the FET gate current, Γ is the FET excess noise factor and R_L is the FET load resistance. For a GaAs MESFET amplifier, Γ is about 1.7. For most FET amplifiers, the FET channel noise, which is the first term in the voltage noise expression, dominates the other amplifier noise sources. For a Bipolar front-end amplifier, the input current and voltage noise powers are given by[11]

$$\langle i_{an}^2 \rangle = 2eI_b \tag{24}$$

$$\langle e_{an}^2 \rangle = \frac{2eI_c}{g_m^2} + 4KT_e r_{bb'} \tag{25}$$

where I_b and I_c are transistor base and collector currents and $r_{bb'}$ is the base-spreading resistance.

3.3 HETERODYNE RECEIVER SIGNAL-TO-NOISE RATIO

The heterodyne signal power, including the effect of the detector nonlinearity, is given by

$$\langle i_s^2 \rangle = 2F_0 [\rho (1 - 2\alpha P_{LO})]^2 P_{LO} P_s \tag{26}$$

where F_0 accounts for the signal power reduction due to speckle, turbulence, atmospheric transmission, misalignment and other systematic losses, and α is the detector nonlinearity coefficient. From Eq.(19), the receiver total noise power is equal to

$$\langle i_N^2\rangle = \left(2e\rho\,(1-\alpha P_{LO})\,P_{LO} + 2eI_d + \frac{4KT_eB_e}{R_f} + \langle i_{an}^2\rangle + \frac{\langle e_{an}^2\rangle}{R_f}\right)\left(\frac{B}{4C}\right) + (2\pi)^2 (C_{in}+C_f)^2 \langle e_{an}^2\rangle \left(\frac{B^2}{16\pi^2 CD}\right) \tag{27}$$

Using Eqs.(26) and (27), the receiver signal Signal-to-Noise Ratio (SNR) can be written in the following form.

$$\frac{S}{N} = \frac{2\rho^2 (1-2\alpha P_{LO})^2 P_{LO} P_s F_0}{\left(2e\rho\,(1-\alpha P_{LO})\,P_{LO} + 2eI_d + \frac{4KT_e}{R_f} + \langle i_{N_{amp}}^2\rangle\right) B_e} \tag{28}$$

Where B_e is the directly related to the receiver bandwidth and is given by

$$B_e = \int_0^\infty \frac{|H(f)|^2}{|H(0)|^2} df = \frac{B}{4C} \tag{29}$$

and $\langle i_{N_{amp}}^2\rangle B_e$ accounts for the amplifier total input noise power. From Eq.(27), the amplifier total noise power per unit frequency can be written as:

$$\langle i_{N_{amp}}^2\rangle = \langle i_{an}^2\rangle + \frac{\langle e_{an}^2\rangle}{R_f} + (C_{in}+C_f)^2 \langle e_{an}^2\rangle \frac{B}{D} \tag{30}$$

3.4 OPTIMUM LOCAL OSCILLATOR POWER LEVEL

The optimum local oscillator power can be obtained by setting the derivative of the SNR equation (28) to zero and solve for P_{LO}[5], that is

$$\frac{d(S/N)}{dP_{LO}} = 0 \tag{31}$$

After some simple mathematical manipulation, Eq.(31) simplifies to:

$$4e\rho\alpha^2 P_{LO}^3 - 6e\rho\alpha P_{LO}^2 - 6\alpha\langle i_{N_{amp}}^2\rangle P_{LO} + \langle i_{N_{amp}}^2\rangle = 0 \tag{32}$$

By numerical evaluation of above equation, the optimum local oscillator power can be obtained

for given detector responsivity and nonlinearity parameters, and the amplifier noise characteristics. As can be seen from Eq.(32), the optimum local oscillator power level is highly dependent on the amplifier noise power which in turn is a strong function of the receiver bandwidth.

3.5 OPTIMUM 2-MICRON HETERODYNE RECEIVER

The following describes the 2-micron heterodyne receiver design and its expected performance using three different amplifiers. The analyses described here are based on the experimental data on a 75 microns diameter, extended wavelength, InGaAs detector acquired from Sensors Unlimited Inc. The measured detector parameters at 2 microns wavelength are presented and discussed in detail in section 2.5 and summarized below in table 1 for 4.5 V applied bias voltage.

Table 1. 2-micron Detector Parameters

PARAMETER	SYMBOL	VALUE
Operating bias voltage	V_B	4.5 V
Responsivity	ρ	1.52 mA/mW
Nonlinearity coefficient	α	0.09 mW^{-1}
Small signal responsivity	ρ_0	1.35 mA/mW
Quantum efficiency	η	0.81
Junction capacitance	C_d	2.5 pF
Dark current	I_d	17.8 μA
Series resistance	R_s	24.7 Ω
Shunt resistance	R_d	280 kΩ

Two of the amplifiers selected for these analyses are standard operational amplifiers manufactured by Comlinear. These are the VF operational amplifier CLC425 and the CF operational amplifier CLC449. The third amplifier is a FET front-end transimpedance amplifier defined and analyzed by R. A. Minasian[12] for a 2 GHz photoreceiver and slightly modified for operation with the 2-micron detector. The Minasian amplifier design is for a detector with 0.15 pF junction capacitance, while the 2 micron detector used for this work has a measured capacitance of 2.5 pF at 4.5 V reverse bias voltage. Using Minasian's results, the front-end FET gate width was appropriately increased from 400 micron to 800 micron to match the 2-micron detector capacitance. Then, the FET parameters provided by Minasian for a typical GaAs MESFET with 1

mm gate length were used for the receiver noise analysis. The FET parameters are listed below with their values expressed as per unit gate width.

Table 2. MESFET Model Parameters

PARAMETER	SYMBOL	VALUE
Transconductance	g_m	80 mS/mm
Output resistance	R_0	140 W.mm
Gate source capacitance	C_{GS}	0.8 pF/mm
Gate drain capacitance	C_{GD}	0.08 pF/mm
Drain source capacitance	C_{DS}	0.2 pF/mm
Input resistance	R_i	1.2 W.mm
Transit time	t	6 ps
Source resistance	R_s	0.8 W.mm
Drain resistance	R_d	1 W.mm
Gate resistance	R_g	0.7 W.mm

It should be noted the MESFET amplifier has been optimized for a 2 GHz receiver and operating it at wider bandwidths by further decreasing its feedback resistance can result in less than optimum performance. On the other hand, the amplifier can operate at its optimum or close to its optimum level at shorter bandwidths by increasing its feedback resistance (Eq.(13)). Figure 4 shows the MESFET amplifier bandwidth as a function of feedback resistance. The Transimpedance Transfer Function (TTF) of this amplifier is shown in figure 3 (a) for two different feedback resistance values. The TTF's of figure3 (a) have been obtained by using the detector parameters given in table 1 and amplifier parameters of tables 2 in Eq.(8). Figure 6 illustrates the receiver performance as a function of applied local oscillator power for three different bandwidths. Figure 6 is the receiver SNR given by Eq. (28) normalized by the shot-noise limited SNR. Figure 6 also illustrates the effect of the detector nonlinearity on the receiver which causes the SNR decreases below its optimum value with increasing local oscillator power. By substituting the detector and amplifier parameters in Eqs. (30) and (32), the optimum local oscillator power for different feedback resistances were obtained and the results are shown in figures 7 as a function of operating bandwidth.

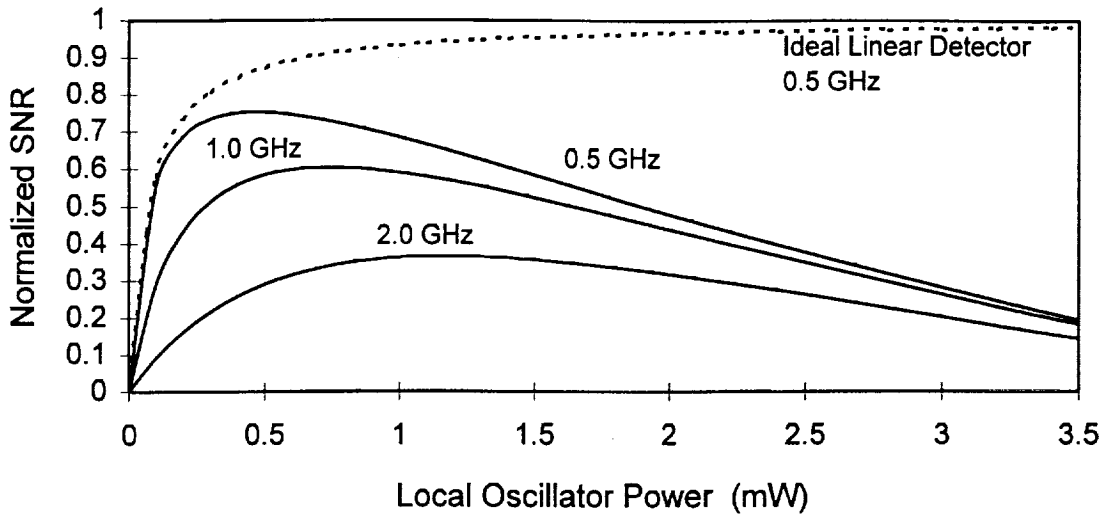

Figure 6. Normalized SNR as a function of applied local oscillator power for a 2-micron heterodyne receiver using MESFET transimpedance amplifier.

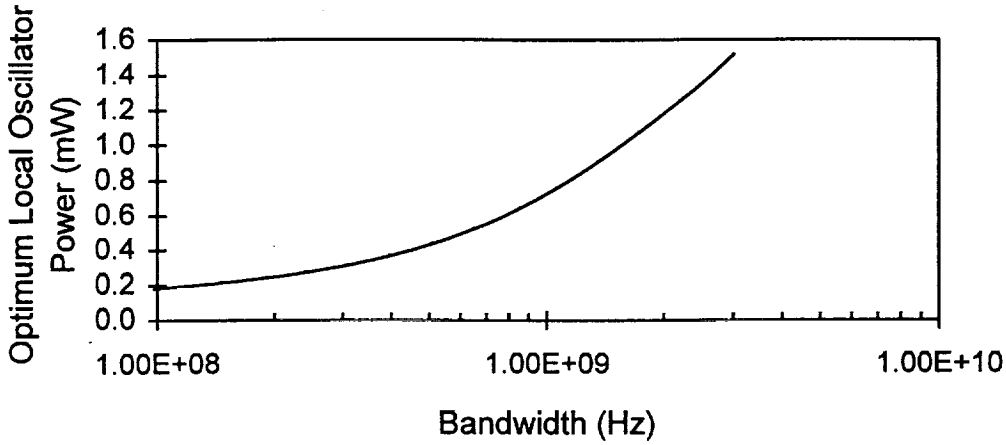

Figure 7. Optimum local oscillator power versus bandwidth for MESFET transimpedance amplifier

Substituting the numerical values of the optimum local oscillator power level for any given bandwidth in Eq.(27), the contribution of each noise source were computed and the result is shwon in figure 8. Figure 8 shows the level of noise powers due to each noise source and the total receiver noise power as a function of bandwidth. It can be seen from figure 8 that the detector shot noise is the dominating noise up to about 650 MHz. However, the amplifier input voltage noise and the feedback thermal noise powers increase faster with bandwidth than the shot noise with bandwith. The amplifier input voltage noise and feedback thermal noise increase approximately as B^3 while the shot noise increase approximately as B^2. For the receiver being

investigated here, consisting of a 75 micron diameter, 2-micron detector and a 2 GHz MESFET amplifier, the amplifier input voltage noise, also reffered to as the FET channel noise, starts to dominate all other noises at about 2 GHz.

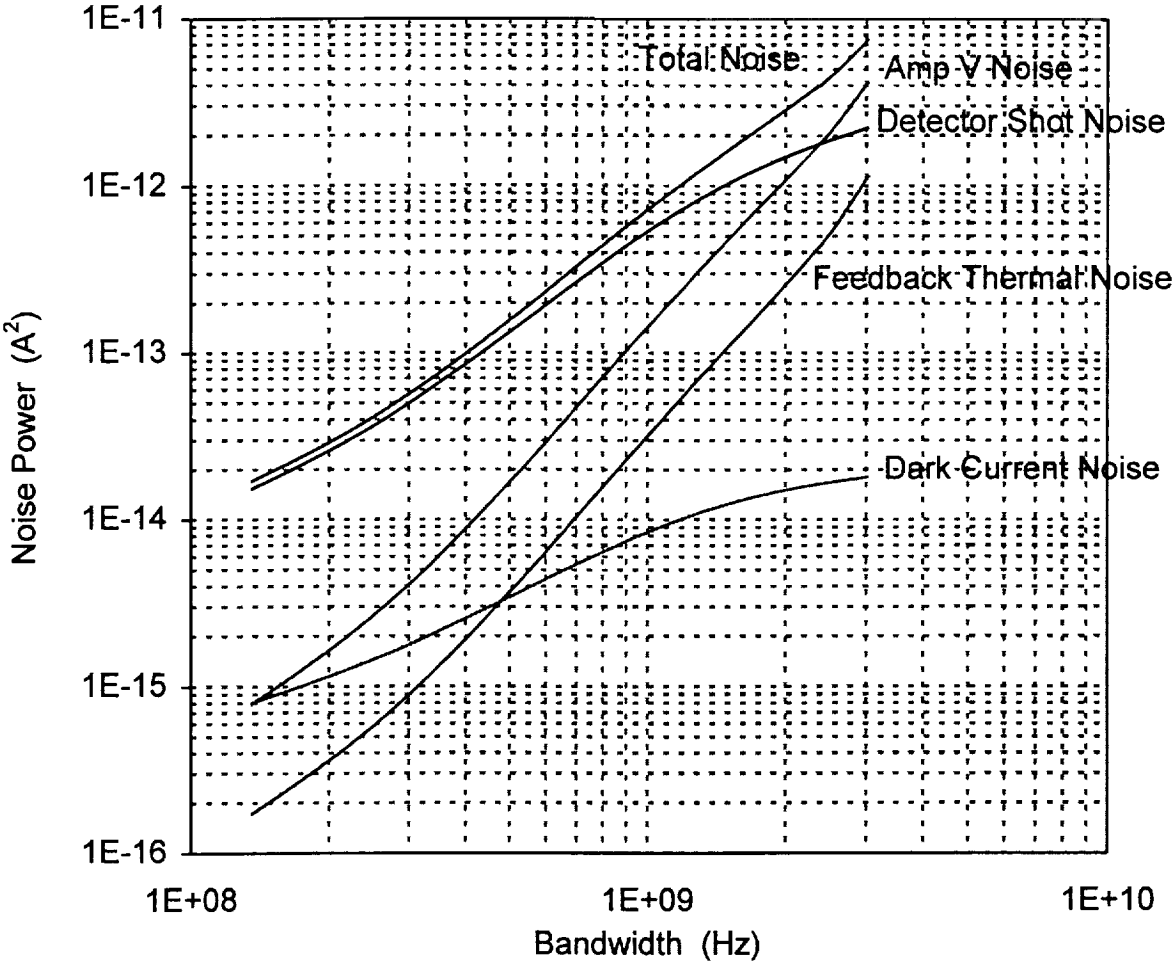

Figure 8. 2-micron heterodyne receiver noise power with MESFET Transimpedance amplifier.

The other two amplifiers considered for this work are a VF operational amplifier (CLC 425) and a CF operational amplifier (CLC 449). Both amplifiers are among the fastest off-the-shelf operational amplifiers manufactured by Comlinear with bandwidths greater than 1 GHz. Tables 3 and 4 provide selected parameters for these amplifiers that are necessary for design and analysis of a heterodyne receiver. The TTF for these amplifiers are shown in figure 3 (b) and (c). The TTF's have been obtained by using the detector parameters given in table 1 and amplifier parameters given in tables 3 and 4 in Eq.(8) for two different feedback resistances. The receiver bandwidths (Eq.(13)) for each of the amplifiers are shown in figure 4 as a function of feedback resistance.

Table 3. VF OP Amp CLC425 Parameters

PARAMETER	SYMBOL	VALUE
DC loop-gain	A_0	$2X10^4$
Loop-gain 3dB response	ω_0	$4X10^5$
Input capacitance	C_{in}	2.5 pF
Output capacitance	C_{out}	0.05 pF
Input resistance	R_{in}	2 MΩ
Output resistance	R_o	5 mΩ
Feedback capacitance	C_f	1.5 pF
Input current noise	$<i^2_{an}>$	$1.44X10^{-24}$ A^2/Hz
Input voltage noise	$<e^2_{an}>$	$1.96X10^{-18}$ V^2/Hz

Table 4. CF OP Amp CLC 449 Parameters

PARAMETER	SYMBOL	VALUE
DC loop-gain	Z_0	$1.4X10^5$
Loop-gain 3dB response	ω_0	$5X10^6$
Input capacitance	C_{in}	1.3 pF
Output capacitance	C_{out}	0.05 pF
Input resistance	R_{in}	45Ω
Output resistance	R_o	0.1Ω
Feedback capacitance	C_f	0.05 pF
Input current noise	$<i^2_{an}>$	$9X10^{-24}$ A^2/Hz
Input voltage noise	$<e^2_{an}>$	$4X10^{-18}$ V^2/Hz

As for the MESFET amplifier, the detector and amplifier parameters were substituted in Eq. (30) and (32) to determine the optimum local oscillator powers for each amplifier. The optimum local oscillator powers for these receivers are shown in figures 9 and 10 as a function of operating bandwidth. It worth mentioning again that the receivers bandwidths are established by selecting the appropraite feedback resistances using Eq.(13).

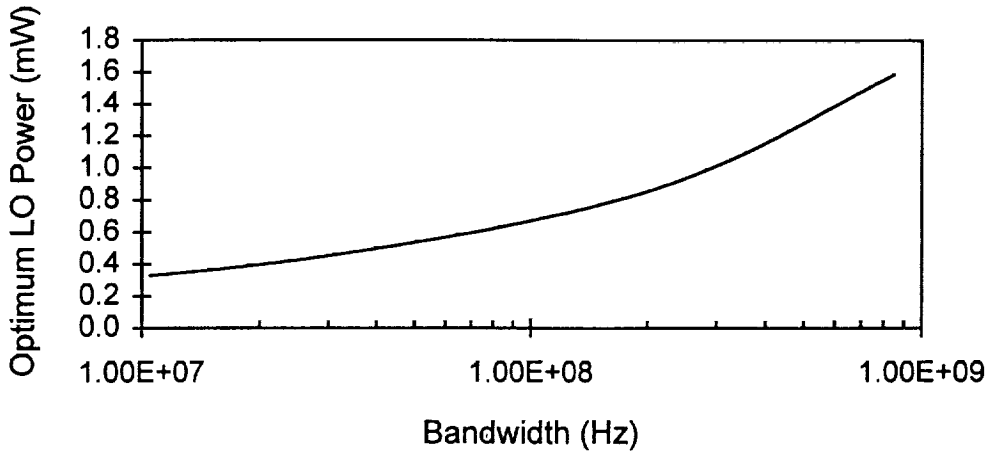

Figure 9. Optimum local oscillator power versus bandwidth for VF operational amplifier CLC425

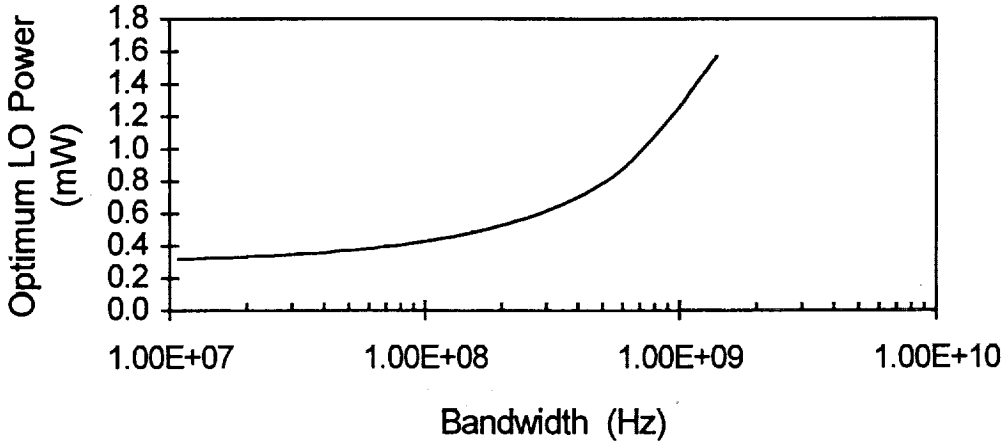

Figure 10. Optimum local oscillator power versus bandwidth for CF operational amplifier CLC449.

Using the detector and the amplifiers parameters and the optimum local oscillator powers in the Eq.(27), the contribution of each noise source for these operational amplifiers have been computed as a function of bandwidth. Figures 11 and 12 show the level of noise powers due to each noise source and the total receiver noise powers for these two receivers using VF and CF operational amplifiers CLC425 and CLC449.

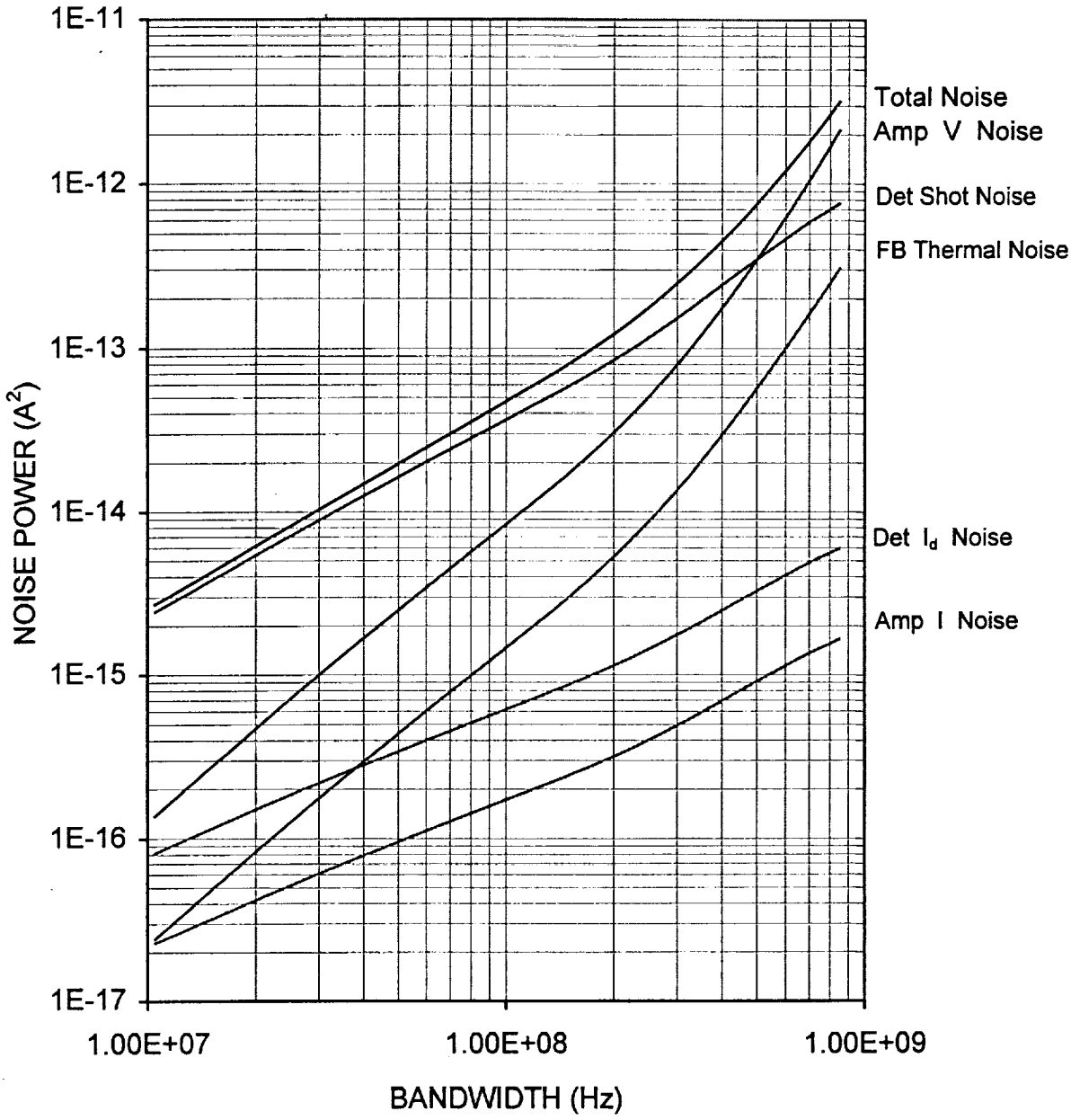

Figure 11. 2-micron heterodyne receiver noise power with VF operational amplifier CLC425.

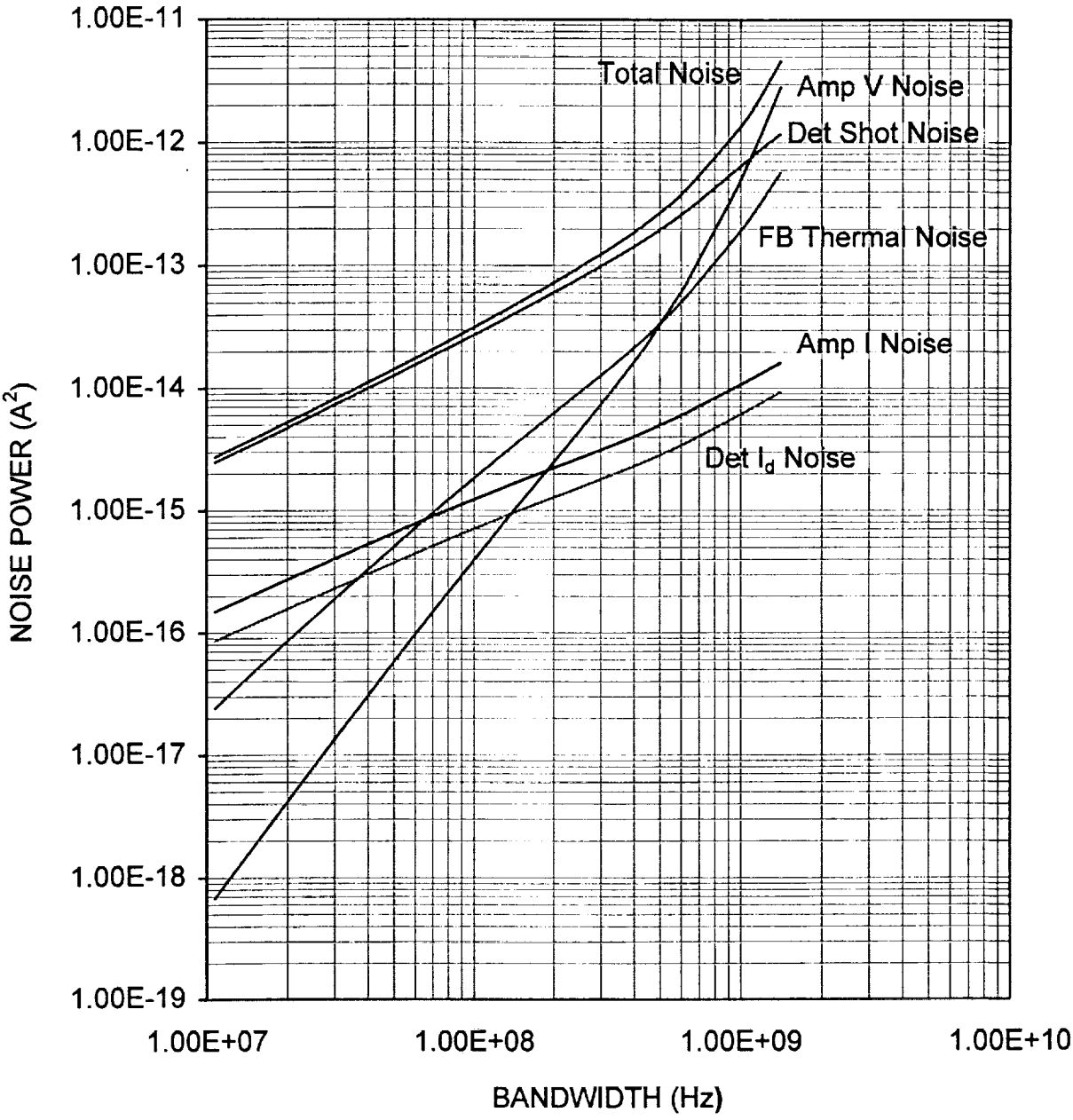

Figure 12. 2-micron heterodyne receiver noise power with CF operational amplifier CLC449.

The performance of the three receivers designed and analyzed in this work are summerized in figure 13 where the normalized SNR for each receiver is plotted versus the operating bandwidth. The SNR's in figure 13 have been has been normalized by the ideal shot noise-limited SNR that ignores the effects of the detector nonlinearity, detector series resistance and the amplifier feedback loading. In other words, the SNR for each receiver has been calculated using Eq.(28) as

a function of bandwidth and then normalized by the following SNR equation commonly used for predicting the performance of coherent lidars.

$$\left(\frac{S}{N}\right)_{ideal} = \frac{\rho_0 P_s F_0}{eB} \tag{33}$$

where ρ_0 is the detector small signal responsivity (see table 1). Therefore, figure 13 provides the deviation from ideal shot-noise-limited operation usually assumed by most workers.

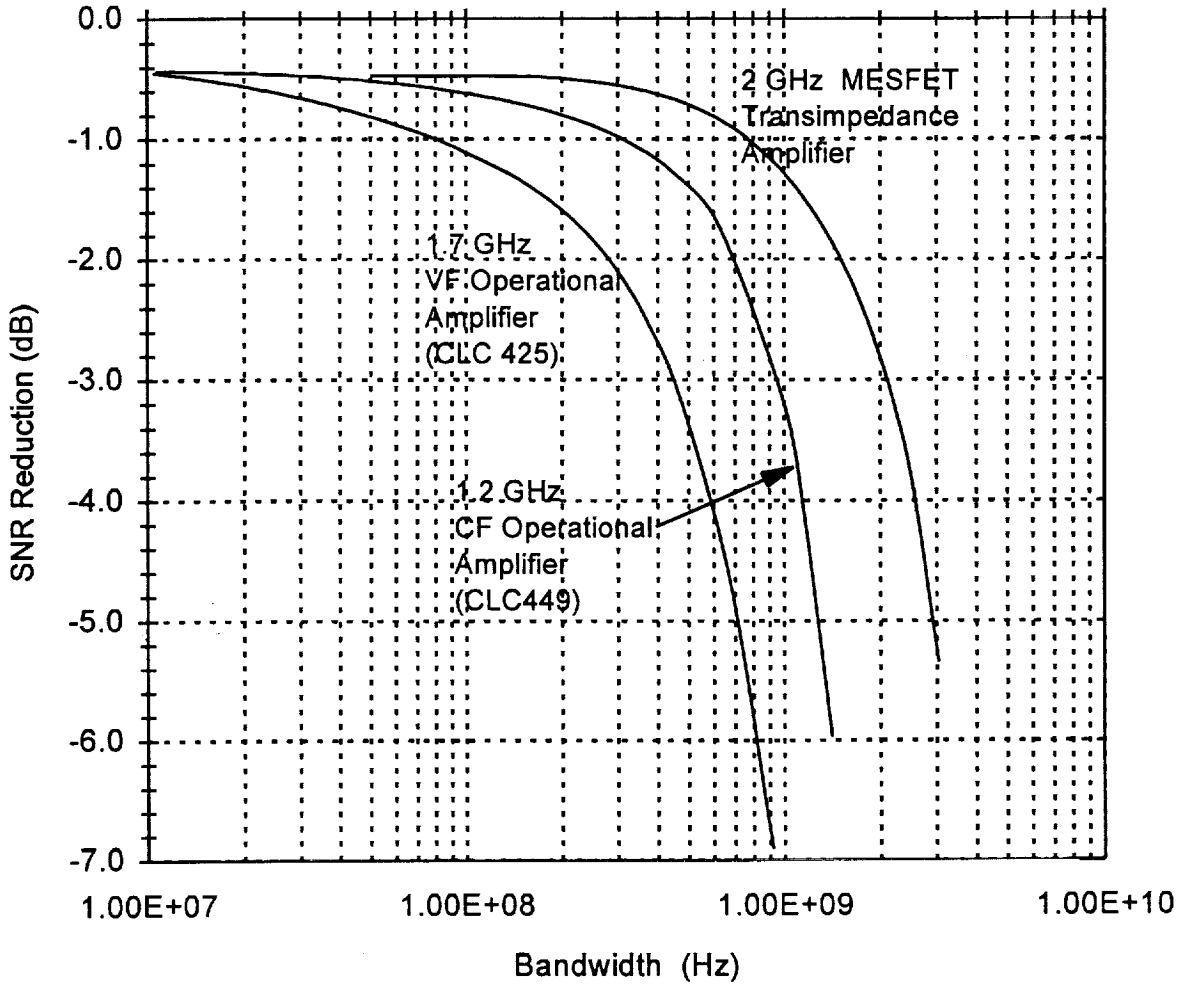

Figure 13. SNR diviation from ideal shot noise-limited operation for 2-micron heterodyne receivers using a 75 micron diameter InGaAs detector interfaced with a MESFET transimpedance amplifier, a VF operational amplifier, and a CF operational amplifier.

4.0 ADVANCED SOLID STATE COHERENT LIDAR TECHNOLOGIES

A preliminary solid state coherent lidar system design for demonstrating the technology readiness for global wind measurements from space was developed and the key technology areas needed to enable such missions were identified. A set of specifications for this demonstrator system was developed and the requirements for interfacing major lidar components and subsystems were established to serve as the basis for an integrated plan for the solid state coherent lidar technology development efforts at different NASA centers. Figure 1 illustrates the general design of the solid state coherent lidar system being considered for demonstrating the technology readiness for space missions and shows the key technologies that are needed to be developed. Some of these technologies are currently under developed at various NASA centers and the work on the remaining technologies are planned to begin in the near future. Figure 1 describes the lidar design and specifies its major components and subsystems.

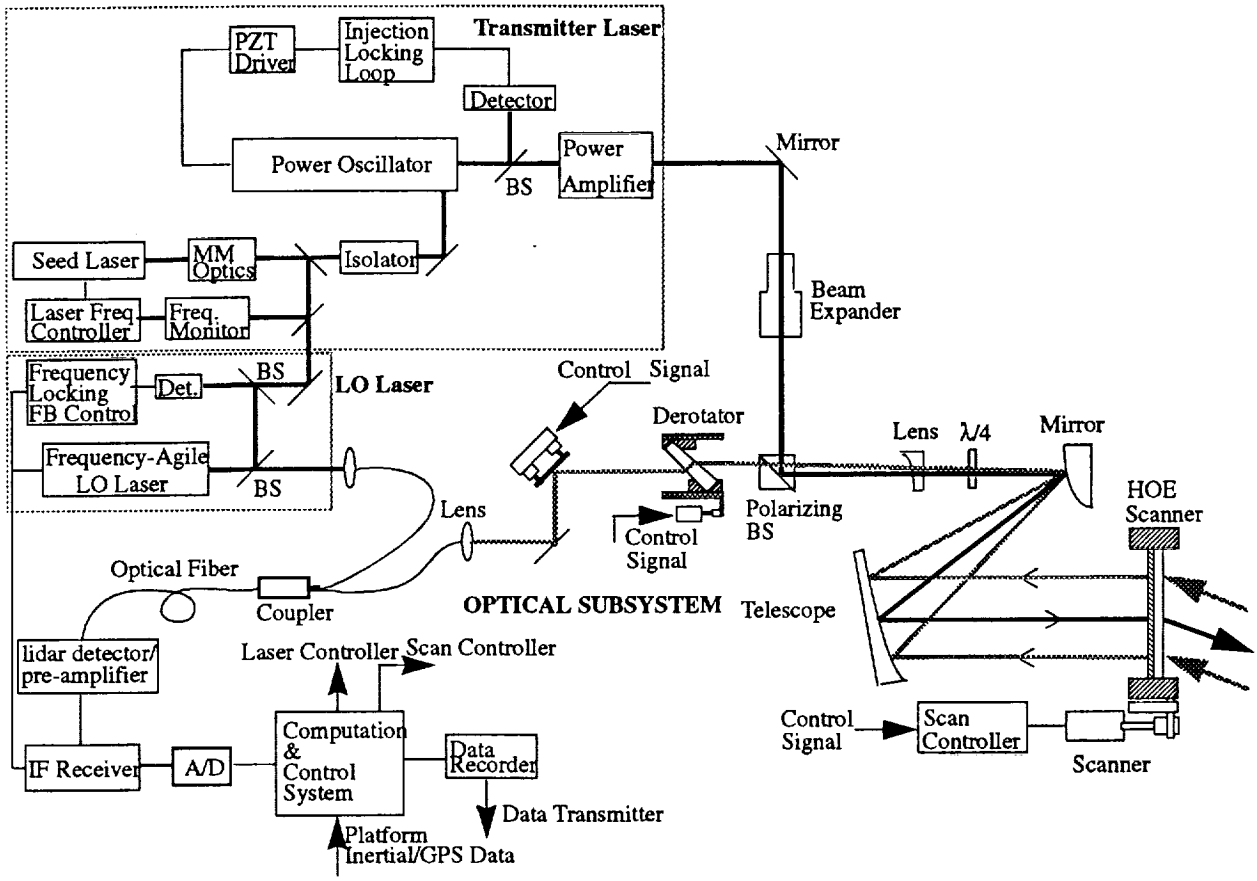

Figure 1. Solid state coherent lidar system for demonstrating technology readiness for space missions.

The lidar utilizes a relatively high power, pulsed laser as the transmitter and a low power, continuous-wave laser as the local oscillator source. The transmitter laser is injection locked to produce single frequency pulses using a highly stable, single frequency, continuous-wave, master

oscillator laser. Part of the master oscillator laser is also used for controlling the local oscillator laser frequency that varies with the scanner position. Variable local oscillator frequency compensates for gross spacecraft-induced Doppler shift. A simplified schematic of a CLR is shown in Figure 1. The pulsed laser output beam is expanded by an off-axis telescope to be transmitted to the atmosphere. The quarter-wave plate placed along the propagation path changes the polarization of the transmitted beam from vertical to circular. The return beam from the atmosphere is received by the same telescope and directed through the quarter-wave plate and a polarizing beamsplitter toward the detector. The derotator and lag angle compensator (LAC)[13,14] placed along the return signal path to correct for the boresight and wavefront errors caused by the scanner and spacecraft motions. At the detector the return radiation is mixed with the local oscillator beam for heterodyne detection. The detector in turn generates an electrical signal at the difference frequency between the signal and local oscillator frequencies. The output of the detector is then bandpass filtered and amplified to be digitized and processed for Doppler frequency shift due to the atmospheric winds.

A transmitter laser system is currently being developed at NASA Langley Research Center and a frequency-agile local oscillator laser is being developed at NASA Jet Propulsion Laboratory. UAH personnel has been working with the NASA/MSFC engineer and scientists towards the development of the other lidar subsystems including the lidar heterodyne receiver and the transmitter/receiver optical assembly. The work on the heterodyne receiver is described in chapters 2 and 3, and the work on the optical subsystem is described in this chapter and chapters 5 and 6.

The followings summarize the general lidar specifications and the requirements for the transmitter and local oscillator laser subsystems.

<u>Lidar</u>	
Telescope clear aperture diameter	25 cm
Scanning angle	30°
Scanning frequency	10 RPM
Total optical throughput	>90%
Detection bandwidth	1 GHz
Detector heterodyne quantum efficiency	>0.6
Heterodyne mixing efficiency	>0.3
IF signal frequency resolution	100KHz
Doppler signal bandwidth	100 MHz
<u>Transmitter Laser</u>	
Pulse energy	500 mJ
Pulse width	500 nsec
Pulse repetition rate	10 Hz
Wavelength	2065 nm
Output polarization	98% Linear
MO short term frequency jitter	<10 KHz/msec

MO long term frequency stability	<100 MHz/hr
Laser linewidth	<2.5 MHz
Pulse to pulse frequency stability	<10 MHz
MO power stability	<5% peak-to-peak, 1 sec
Pulse energy stability	5%
MO laser power available to LO laser	2 mW
Beam quality	<1.1XD.L.
Electrical to optical efficiency	5%
Frequency-agile local oscillator Laser	
Output power	25 mW
Power stability	<5% peak-to-peak, 1 sec
Output polarization	98%Linear
Short term frequency jitter	<100 KHz/msec
Continuous frequency tuning bandwidth	7.9 GHz
Average tuning speed	1.3 GHz/sec
Maximum tuning speed	8.2 GHz/sec
Beam quality	<1.1XD.L.

The NASA's plan is to developed a breadboard lidar based on these requirements to evaluate the advanced lidar technologies under development and to demonstrate the technology readiness of solid state coherent lidar for low-cost small satellite and shuttle missions.

The transmitter/receiver optical subsystem includes the transmitter/receiver telescope, the return signal de-rotator, the lag angle compensator, and the scanner. The design and analysis of an advanced monolithic signal beam de-rotator is described in the next chapter, the telescope design along with a complete tolerance and performance analyses is explained in chapter 5, and the effort on the low-mass scanner is explained in this chapter.

4.1 HOLOGRAPHIC AND DIFFRACTIVE OPTICAL ELEMENT SCANNERS

A study was initiated in this period to determine the feasibility of using Diffractive and Holographic Optical Elements (DOE and HOE) for scanning the lidar transmitter beam (see figure 1). The diffractive and holographic optical elements have the potential of substantially reducing the mass of the lidar systems and allowing for a much easier spacecraft accommodation design. The diffractive and holographic optical elements change the direction of a laser beam by diffraction, as opposed to the conventional scanning techniques that are based on refraction and reflection. The diffractive and holographic optical elements can potentially reduce the mass of the lidar scanner to less than one fourth of a wedge scanner with the same clear aperture diameter. Wedge scanners have frequently been used in the past for airborne lidar measurements and is now being considered for spaceborne measurements.

As part of this effort, an advanced holographic photopolymer material was experimentally evaluated at 2 microns wavelength. This holographic material, developed by Dupont, is

insensitive to environment and more rugged compared to more conventional dichromated gelatin (DCG) holographic material that is sensitive to moisture and need to sealed. To experimentally evaluate the holographic polymer material, a 10-micron thick film was recorded and its properties were measured. The recorded pattern was designed for deflecting a 2-micron beam by 30 degrees. Using the U.S. Army Missile Command laboratory facilities in Huntsville and an argon-ion laser, several holographic films were exposed by two 2 mW beams at normal and 10^{o} off normal over different time periods. The films were then measured at 633, 859, 1300 and 2067 nm wavelengths before and after baking the films at different temperature and over different time spans. The experimental data showed that both the refractive index depth of modulation and deflection efficiencies decrease with increasing wavelength. The change in refractive index with 20 seconds of exposure was measured to be about 0.014 and 0.007 at 633 nm and 2067 nm before baking, and 0.036 and 0.010 after baking the film at 120^{o}C for two hours. The corresponding deflection efficiencies were measured to be 0.94 at 633 nm and 0.04 at 2067 nm before baking, and 0.22 and 0.09 after baking the film. The results were consistent with the analytical predications, which shows that the deflection efficiency can be considerably improved by using a much thicker film of about 100 microns. Unfortunately, such thick holographic film was not available at the time of this work. The thickest film Dupont could provide was 50 microns which was acquired by MSFC to be processed and measured at a later time.

UAH also specified an experimental HOE scanner, using dichromated gelatin (DCG) holographic material, to be fabricated and measured for 2-micron operation. This scanner was fabricated by the Teledyne Brown Engineering (TBE) and delivered to MSFC. This scanner consists two 15 cm substrates with the holographic material sealed between them. The actual useful area has a 10 cm diameter. This scanner will be measured at 2 microns wavelength by the UAH personnel in the DCF at MSFC.

UAH recommends to continue this work by investigating, both analytically and experimentally, other HOE and DOE techniques such as diamond turning, photolithography and laser writing. The analytical work is to include the development of a model using the exact electromagnetic vector field theory to predict the performance of different technique and to optimize their designs. These designs can then be used to fabricate a number of experimental scanning elements. UAH personnel can then use the DCF and other MSFC optical laboratories to fully evaluate the properties of the experimental elements for use in 2-micron coherent lidars.

5.0 SIGNAL BEAM DE-ROTATOR

In principle, a coherent Doppler lidar uses naturally occurring atmospheric aerosols to scatter transmitted radiation from a laser back to a receiver where the Doppler frequency shift is used to measure the air motion radial velocity. The Doppler shift is extracted by utilizing heterodyne detection for which the frequency of the detectable signal is equal to the difference frequencies between the return radiation and a reference local oscillator beam. Since the Doppler lidars provide the wind velocity component along the line-of-sight of the transmitted beam, the wind vector velocity is determined by pointing the transmitted beam to at least three different directions[16-19]. The most conventional method of directing the laser beam to different directions and effectively measuring the atmospheric wind fields by a Doppler lidar, either from a ground, or airborne, or a spaceborne platform, is the conically-scanning technique which generates a circular pattern in the target plane[20-22]. However, the lidar performance is greatly affected by the motion of the scanner during the transmitted pulse round trip time. As the laser energy reflects off the atmospheric aerosols and travels back to the lidar telescope, the scanner continues to move causing signal beam to follow a different path through the telescope than that of the transmitted beam. Therefore as the scanner continues to rotate and the transmitted beam sweeps a conical pattern in the atmosphere, the received signal beam orbits about the optical axis that extends to the lidar photodetector and coincides with the local oscillator beam. In a Doppler lidar system, utilizing optical heterodyne detection, the relative alignment of the received signal with respect to the local oscillator beam is particularly critical. This is due to the fact that the mean power of the electronic signal generated by the photodetector decreases exponentially with the angle between the signal and local oscillator beams γ, that is $\bar{i}_s^2 \propto e^{-a\gamma^2}$. For ground-based and airborne applications, this effect limits the scanning frequency and consequently the lidar update rate. For spaceborne measurements of the earth's wind fields, the scanner motion must be compensated for any reasonable scanning frequency due to very long propagation path of several hundreds of kilometers. This invention provides a simple and robust mechanism for compensating the scanner motion and allowing for optimum laser radar operation.

Previously, a rotating periscope has been proposed for a spaceborne lidar system to maintain the received beam along a fixed axis to the laser radar detector as the scanner rotates about its axis[13,14]. Another approach is the stop-and-steer scanning technique that allows sufficient time for the signal beam to be received before the scanner begins to move to its next position[15]. A novel but simple signal de-rotator scheme has been developed under this work that provides a low mass, compact and robust alternative to rotating periscopes and stop-and-steer techniques. In addition to spaceborne applications, this scheme is also ideal for use in airborne systems for which the compactness and ruggedness are critical design issues.

5.1 PRINCIPLE OF OPERATION

The signal beam de-rotator that has been devised utilizes a monolithic optical element for maintaining the received signal beam with respect to the local oscillator beam along a fixed axis to

the lidar photodetector. The de-rotator performs two functions: changing the signal beam direction to be continuously parallel to the optical axis, and translating the signal beam to the optical axis that coincides with the local oscillator beam and extends to the photodetector. By synchronizing the rotation of the de-rotator about the optical axis with that of the scanner, the signal beam is then maintained along the optical axis and aligned with respect to the local oscillator beam

The de-rotator optical substrate has two plane surfaces that are inclined with respect to each other at a relatively small wedge angle. The de-rotator substrate is selected from the optical materials with relatively high optical transmission and high index of refraction at the operating wavelength to minimize the absorption losses of signal. For operation in near-infrared region, the optical substrate material may be Silica, Zinc Selenide, Zinc Sulfide, or Germanium. The de-rotator optical element is placed on the return signal beam path at 45 degrees angle with respect to the optical axis. The plane of the optical element, defined by the vectors normal to its surfaces, is set to be parallel to plane of the incident signal beam and the optical axis as shown in figures 1 and 3. Since the signal beam incident on the de-rotator substrate rotates about the optical axis with the scanner, as illustrated in figure 1, the de-rotator substrate must also rotate to sustain its relative orientation with respect to the signal beam. Since the de-rotator substrate has a different index of refraction than the free space, the signal beam translates in the plane of the optical element. This translation distance is directly related to the substrate thickness and refractive index. The de-rotator substrate also changes the signal beam direction by an angle that is directly related to its wedge angle and refractive index.

Figure 1 illustrates the operation of the de-rotator in a lidar system. The lidar transmitter/receiver telescope is an off-axis parabolic telescope and its scanner is an optical wedge. It should be noted that the optical wedge scanner may be replaced by a holographic or a diffractive optical element without loss of generality for the analysis and formulations described below. The purpose of the telescope is to expand the transmitter beam and collect the return signal scattered off the target. The off-axis telescope has the advantage of high isolation between the transmitter and return radiations. In figure1, the transmitted beam is reflected off a polarizing beamsplitter before being expanded by the telescope. The optical wedge deflect the beam in a plane defined by the normal vectors to its surfaces. As the optical wedge rotates along its axis, the transmitted beam scans a circular pattern at the target plane. The deflection angle for an optical wedge is given by:

$$\sin(\theta) = \sin(\alpha)\sqrt{n^2 - \sin^2(\alpha)} - \sin(\alpha)\cos(\alpha) \qquad (1)$$

where α is the scanner wedge angle and n is its index of refraction. For a given optical material with a known index of refraction, the wedge angle necessary for providing a desired scanning angle can be determined by:

$$\alpha = 2\tan^{-1}\left(\frac{1 - H + \sqrt{1 + n^2 - 2H}}{\sin(\theta)}\right) \qquad (2)$$

where $H = \sqrt{n^2 - \sin^2(\theta)}$

As an example, a germanium scanner requires a 9.12^{0} wedge angle to deflect a laser beam at 2 microns wavelength by 30^{0}.

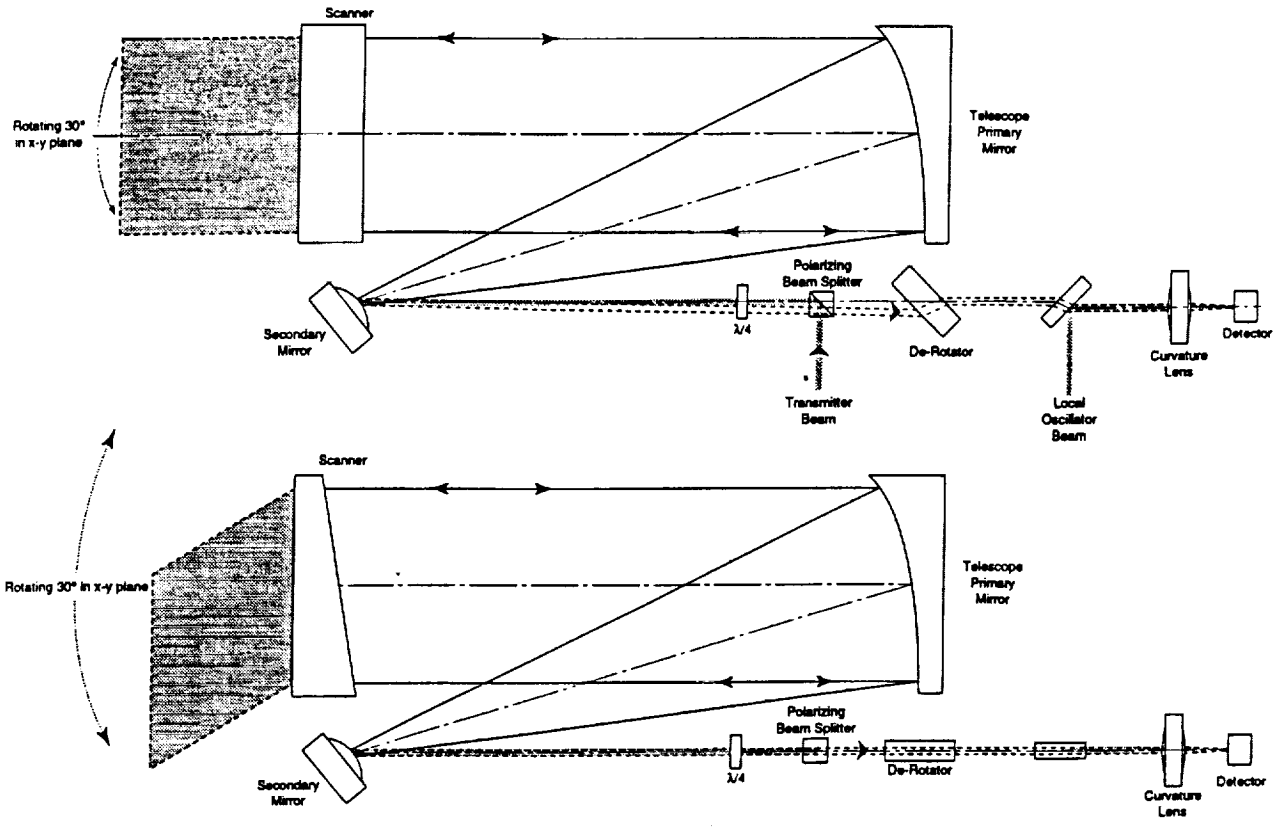

Figure 1. Transmitter/receiver optical subsystem for a scanning coherent Doppler lidar. Two orthogonal views are shown at time t when the scanner plane is parallel to the X-Y plane of the coordinate system.

A portion of the transmitted beam energy scatters off the atmospheric aerosols and travels back to the laser radar. The return signal at the scanner can be expressed by a unit vector parallel to its direction of propagation as

$$\vec{S}1\,(t) = \cos(\theta)\,\hat{\imath} + \sin(\theta)\cos(\omega_s t)\,\hat{\jmath} + \sin(\theta)\sin(\omega_s t)\,\hat{k} \qquad (3)$$

where $\hat{\imath}$, $\hat{\jmath}$, and $\hat{k}$ are unit vectors along X, Y, and Z axes of coordinate system.

Using the vector form of Snell's law, the signal beam direction after passing through the scanner can be written as

$$\vec{S}2(t) = [H + K\cos(\alpha)]\,\hat{i} + [\sin(\theta)\cos(\omega_s t) + K\sin(\alpha)\cos(\omega_s t + \delta)]\,\hat{j} + [\sin(\theta)\sin(\omega_s t) + K\sin(\alpha)\sin(\omega_s t + \delta)]\,\hat{k} \quad (4)$$

where

$$K = \sqrt{1 - n^2 + U^2} - U$$

$$U = H\cos(\alpha) + \sin(\theta)\sin(\alpha)\cos(\delta)$$

and d is the angular displacement of the scanner during the transmitter beam round trip time to the target. The scanner angular displacement during the transmitter round trip time is equal to:

$$\delta = \frac{2L}{c}\omega_s \quad (5)$$

where L is the lidar range, c is speed of light, and ω_s is the scanner angular velocity. The signal beam deviation angle from the optical axis at the scanner output is given by

$$\gamma = \cos^{-1}\left(\frac{S2_x(t)}{\sqrt{S2_x^2(t) + S2_y^2(t) + S2_z^2(t)}}\right) \quad (6)$$

where $S2_x(t)$, $S2_y(t)$, and $S2_z(t)$ are the three components of vector S2(t) along X, Y, and Z axes. Using the expression for the vector S2(t), it can be shown that the signal beam deviation angle simply equal to

$$\gamma = \delta\sin(\theta) \quad (7)$$

As the signal beam travels through the telescope, its size condenses and its deviation angle increases by a factor of g, the telescope magnification constant. Therefore, the unit vector that defines the direction of the signal beam at the telescope output (secondary mirror) can be written as

$$\vec{S}3(t) = \cos(g\gamma)\,\hat{i} + \frac{S2_y(t)}{\sqrt{S2_y^2(t) + S2_z^2(t)}}\sin(g\gamma)\,\hat{j} + \frac{S2_z(t)}{\sqrt{S2_y^2(t) + S2_z^2(t)}}\sin(g\gamma)\,\hat{k} \quad (8)$$

The transverse displacement of the signal beam at the telescope output is usually negligible compared with the beam diameter and can be ignored. However as the beam travels away from the telescope, its distance to the optical axis increases. Furthermore, as the scanner rotate about its axis, the signal beam orbits around the optical axis. These effects are illustrated in figure 2, which shows the signal beam as it exits the telescope secondary toward the photodetector.

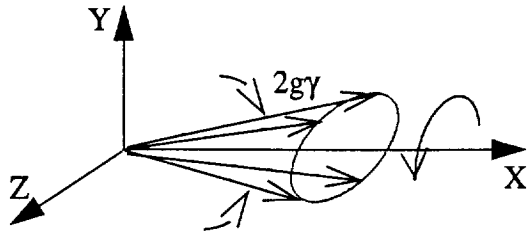

Figure 2. Illustration of the signal beam direction with the scanner motion at the telescope primary mirror.

The de-rotator placed at distance r from the telescope secondary will then deflect the signal beam direction by gγ radians and translates it in the photodetector plane by d=r tan(gγ). The operation of the de-rotator is illustrated in figure 3.

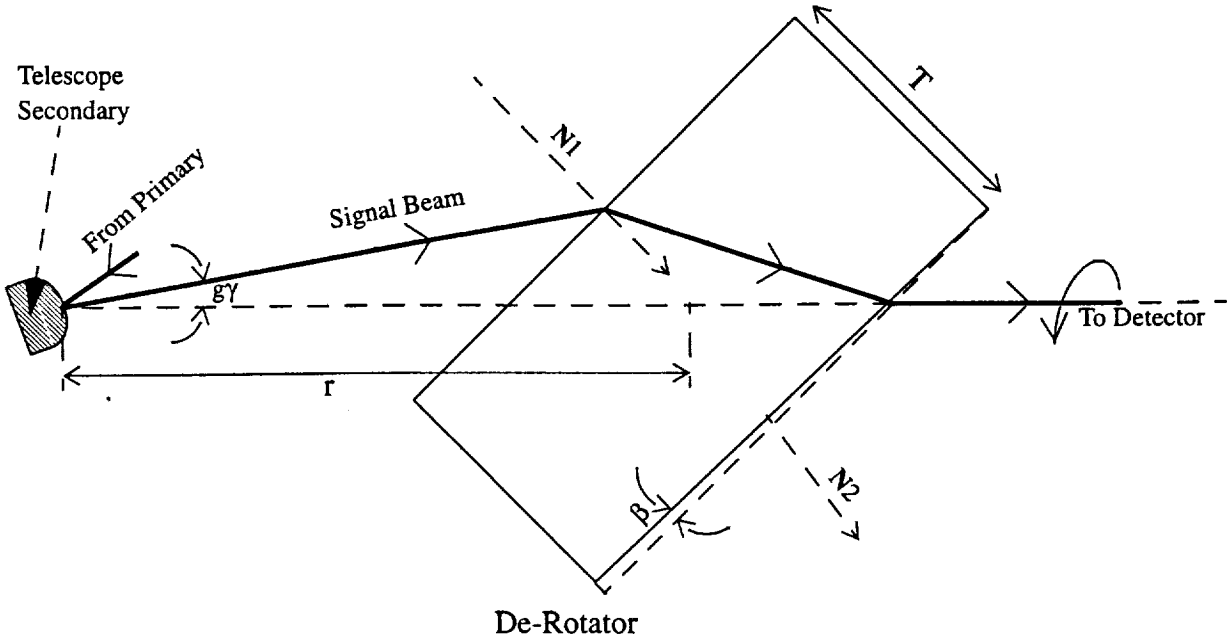

Figure 3. De-Rotator Principle of Operation.

The signal beam experiences a change of direction by both input and output surfaces of the de-rotator. The direction of the signal beam as it propagates through the de-rotator substrate, can be expressed as following.

$$\vec{S}4(t) = \frac{\vec{S}3(t)}{n_d} + \left(\sqrt{n_d{}^2 - 1 + (\vec{S}3(t) \cdot \vec{N}1(t))^2} - \vec{S}3(t) \cdot \vec{N}1(t) \right) \cdot \frac{\vec{N}1(t)}{n_d} \tag{9}$$

Where n_d is the index of refraction of the de-rotator substrate, and $\vec{N}1$ is the unit vector normal to the de-rotator input surface given by

$$\vec{N}1(t) = \frac{\sqrt{2}}{2}\left[\hat{\imath} - \frac{S2_y(t)}{\sqrt{S2_y^2(t) + S2_z^2(t)}}\hat{\jmath} - \frac{S2_z(t)}{\sqrt{S2_y^2(t) + S2_z^2(t)}}\hat{k} \right] \tag{10}$$

The signal beam, deflected by the input surface of the de-rotator, crosses the optical axis exactly at the de-rotator output surface. Therefore by using the above expression for the signal beam direction inside the de-rotator and performing some mathematical manipulations, a formulation for specifying the thickness of the de-rotator substrate was derived.

$$T = \frac{r \tan(g\gamma) \sqrt{2\left(n_d^2 - \sin^2\left(\frac{\pi}{4} + g\gamma\right)\right)}}{\sqrt{n_d^2 - \sin^2\left(\frac{\pi}{4} + g\gamma\right)} - \sin\left(\frac{\pi}{4} + g\gamma\right)(1 - \tan(g\gamma))} \tag{11}$$

where r is the distance from the telescope secondary to the center of the de-rotator.

The signal beam unit vector exiting the de-rotator output surface can be written in a similar fashion as

$$\vec{S}5(t) = n_d \cdot \vec{S}4(t) + \left[\sqrt{1 - n_d{}^2 + (n_d \cdot \vec{S}4(t) \cdot \vec{N}2(t))^2} - (n_d \cdot \vec{S}4(t) \cdot \vec{N}2(t)) \right] \cdot \vec{N}2(t) \tag{12}$$

where $\vec{N}2$ is the unit vector normal to the de-rotator output surface given by

$$\vec{N}2(t) = \cos\left(\frac{\pi}{4} + \beta\right)\hat{\imath} - \frac{\sin\left(\frac{\pi}{4} + \beta\right)}{\sqrt{S2_y^2(t) + S2_z^2(t)}}(S2_y(t)\hat{\jmath} + S2_z(t)\hat{k}) \tag{13}$$

where β is the wedge angle of the de-rotator substrate. By setting $\vec{S}5(t)$ equal to $\hat{\imath}$, an expression

for specifying the de-rotator wedge angle was derived.

$$\beta = \tan^{-1}\left[\frac{\sin(g\gamma) + \cos(g\gamma) - 1}{\sqrt{2n_d^2 - (\sin(g\gamma) + \cos(g\gamma))^2 - 1}}\right] \tag{14}$$

As can be seen from the de-rotator analytical description, the de-rotator orientation with respect to the optical axis and the scanner is defined by its normal unit vectors, $\vec{N}1(t)$ and $\vec{N}2(t)$, and its substrate is specified by the expressions for T and β.

5.2 De-Rotator Design For A Space-Based Coherent Lidar

The following represents a typical spaceborne coherent Doppler lidar design operating at 2 microns wavelength.

Scanner angular velocity	ω_s = 1.047 rad/sec (10 RPM)
Scanner full angle	$2\theta = 60^o$
Telescope magnification constant	g = 20
Target range	L = 404 km

The de-rotator substrate parameters for three different materials are provided in the table below, assuming that the distance between the telescope secondary and the center of the de-rotator is 20 cm.

Table 1. Examples of de-rotator substrates for a space-based coherent lidar.

	SILICA	ZINC SELENIDE	GERMANIUM
Index of refraction at 2 μm wavelength	1.437	2.445	4.143
Thickness	18.54 mm	11.44	9.65 mm
Wedge angle	2.11°	0.69°	0.33°

It should be noted that the monolithic de-rotator described here is not restricted to any particular telescope type and applies to all continuous motion conically-scanning systems including holographic and diffractive optical element scanners and rotating mirrors. It should also be mentioned that variations of this scheme as may be used with the scanners generating non-circular patterns such as line and semi-circle patterns.

6.0 PERFORMANCE MODELING AND ANALYSIS OF A SPACEBORNE LIDAR TELESCOPE

Space applications of coherent lidars continue to demand for more compact and robust designs with a higher degree of sensitivity [16]. For a space-based coherent lidar, the telescope and scanner along with their associated support structures and control units account for most of the weight and size budget of the system. Therefore, any reduction in their mass will have a major impact on the mission cost. This chapter describes the design and performance of a 500 mm telescope that can significantly reduce the size and weight of a space-based coherent lidar operating at 2 microns wavelength. The telescope design as described here can be readily scaled to smaller aperture diameters, suitable for airborne applications, with similar alignment and fabrication tolerances.

The LIDAR telescope consists of a large off-axis reflective telescope, a large-aperture diffractive scanner, a signal beam (image) de-rotator and a lag angle compensator. Due to the orbiting motion of the satellite and scanning, the boresight of the telescope shifts during the round trip time of the transmitter laser pulses to the target. In a coherent lidar system, utilizing optical heterodyne detection, the relative alignment of the received signal with respect to the local oscillator beam is particularly critical. The two compensators have been designed to correct the boresight errors as well as the wavefront errors caused by beam wandering due to the boresight changes. A complete description of the signal beam de-rotator is provided in previous chapter.

6.1 SYSTEM MODELING

The complete telescope optical system has been modeled which includes the primary mirror, secondary mirror, quarter wave plate, recollimating lens, beam splitter, beam derotator, and lag angle compensator. Figure 1 is a perspective view of the entire telescope optics. The analysis covers wavefront error, boresight, and polarization.

Because of a non-traditional design concept, the performance analysis has to address some special issues, such as the effect of the quarter wave plate and the performance changes due the off-axis nature of the design.

6.1.1 SYSTEM LAYOUT

A three-element catadiaoptric off-axis Galilean telescope has been designed to eliminate the central obscuration, reduce the back scattering, and lower the parametric sensitivities. The telescope has no real focus to prevent air breakdown. The mirrors and lens are general conical surface used in an off-axis configuration. One quarter wave plate is located in front of the lens to convert the circular polarized beam to a linear polarized beam. A beam splitter follows the telescope to reflect the output beam into the telescope and to transmit the input beam to a monolithic beam derotator. The pupil relay has been omitted to simplify the optical system.

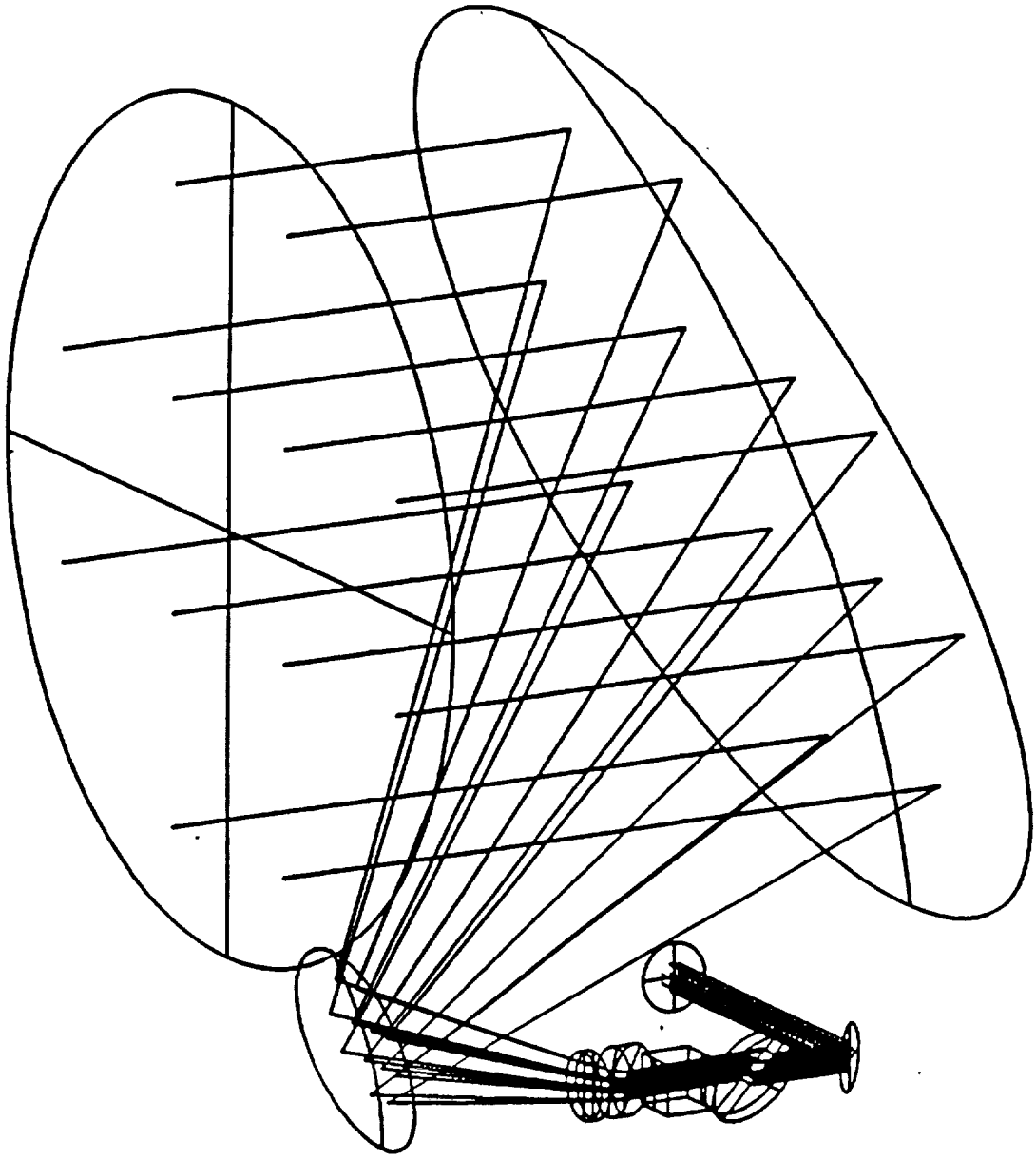

Figure 1. Optical System Layout

The beam derotator removes both the angular and linear displacements caused by the scanner and telescope. A single electro-mechanically controlled folding mirror has been used to perform the lag angle compensation.

The primary mirror, secondary mirror, and recollimating lens share the total optical power to lower the parametric sensitivity. The conical constants of the secondary mirror and two lens surfaces are also optimized to achieve the overall optical performance.

6.1.2 THE EFFECT OF THE QUARTER WAVE PLATE

The quarter wave plate is located in the convergent ray path. Any parallel plate in the non-collimated ray path will introduce aberrations. In the design, a fused silica plate has been added to model this effect. The telescope optics has to be re-optimized to obtain an acceptable performance. The surface shape of the mirrors as well as the lens changes slightly after introducing the quarter wave plate. The locations of the mirrors and the lens stay same.

The sensitivity analysis shows that the performance is not sensitive to the location of the quarter wave plate. The performance is sensitive to the thickness and wedge errors of the plate. The tilt of the element has little effect on the performance.

6.2 PERFORMANCE

The system specifications are as follows:

Magnification	25	X	(afocal)
Entrance aperture	500	mm	(diameter)
Exit pupil	20	mm	(diameter)
Overall axial length	400	mm	
Off-axis value	375	mm	
Wavelength	2.067	micron	
Field of view	0.0802	degree	(conical scan angle)

The performance analysis as well as the sensitivity analysis have not included the scanner effects. The conical scan field of view has been considered in the modeling and analysis.

6.2.1 WAVEFRONT PERFORMANCE

Wavefront error has been used to quantitatively describe the beam quality of the telescope. The RMS wavefront error of less 1/10 wave is required for the coherent operation. The design has been optimized to achieve much lower wavefront errors. This leaves enough margin for the fabrication and integration tolerances.

6.2.1.1 OFF-AXIS EFFECT

Because of the off-axis operation of the telescope, the field characteristics of the performance are not symmetric. The performance can not be simply checked only on-axis and at full field as in the traditional rotation symmetrical system. However, the field character is plano symmetrical. We have checked the performances at the (1) center of the field, (2) top most field, (3) lower most field, and (4) right most field. Left most field is mirror symmetrical to the right most field.

6.2.1.2 WAVEFRONT FOR THE EMITTING BEAM AND RETURNING BEAM AT DIFFERENT FIELD ANGLES

Figures 2 to 5 are the plots of the wavefront maps at different field angles. The RMS wavefront errors are:

0.0034 wave	(At the top most field shown in Figure 2)
0.0040 wave	(At the low most field shown in Figure 3)
0.0085 wave	(At the right most field shown in Figure 4)
0.0087 wave	(At the center of the field shown in Figure 5, output path)

The peak-to-valley errors are also well below requirements.

6.2.2 BORESIGHT

The boresight is the other most important performance parameter of the optical system for a coherent operation. An error of 1 micro-radians is required in the object space.

6.2.2.1 DISTORTION PROBLEM

The distortions of the off-axis optics are not axial symmetrical anymore. The beam with a conical scan motion will have slight ray angle changes at different scanning clock angles caused by the non-symmetrical distortions. It will be a nightmare to correct this kind of error. Therefore, distortion check has to be performed to ensure the ray angle uncertainty is within the boresight requirement.

6.2.2.2 BORESIGHT AT DIFFERENT BEAM ANGLE

The boresight error at different scanning positions are listed:

0.365	micro-radians	(At top most of the field)
0.365	micro-radians	(At low most of the field)
0.271	micro-radians	(At right most of the field)

The boresight error introduced by other parts, such as the beam derotator and lag angle compensator is controlled by the tolerances of these parts.

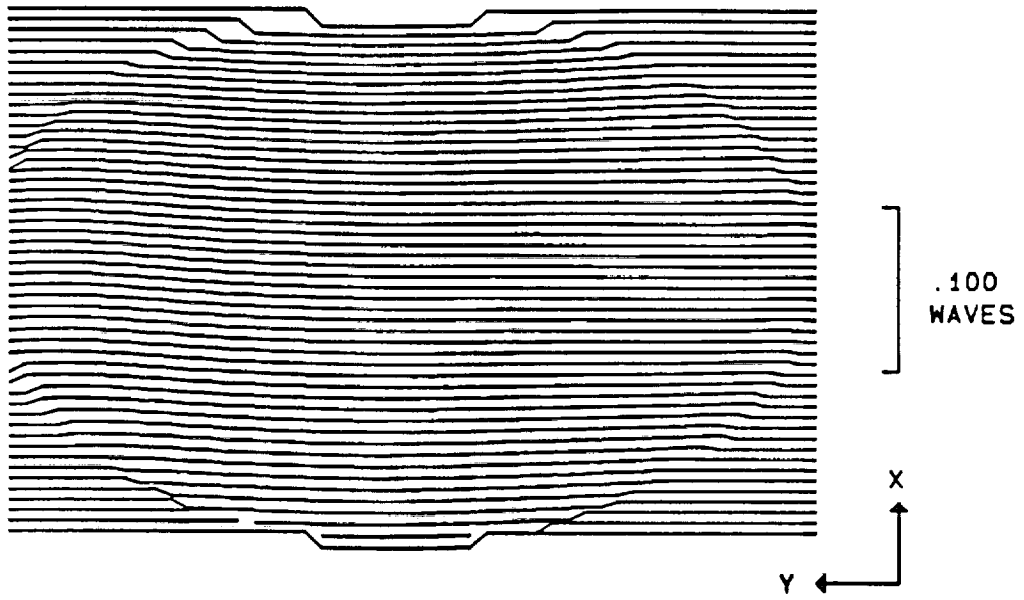

FRACTIONAL FIELD 1.0000 .0000 ID LID TELS QWAV BSPL DERO LAC LIDTQBDL1159
PUPIL 2 1. 0 .1 0 WAVELENGTH 2.06700

SEMI-FIELD = .0802 DEGREES SEMI-APERTURE = 250.0000 MM

Figure 2. Wavefront Error At The Top Most Field

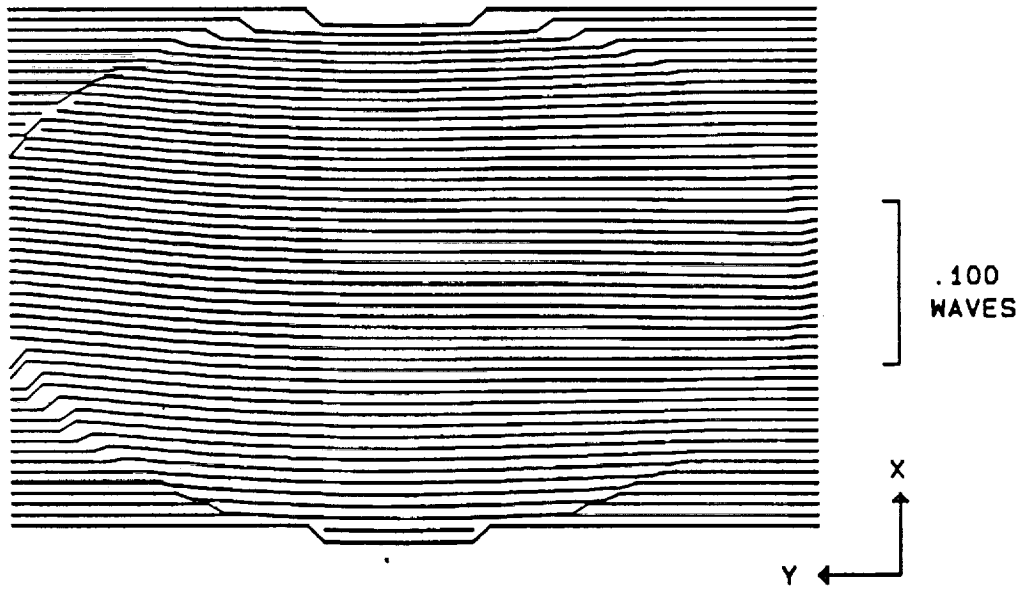

FRACTIONAL FIELD -1.0000 .0000 ID LID TELS QWAV BSPL DERO LAC LIDTQBDL1159
PUPIL 2 -1 0 .1 0 WAVELENGTH 2.06700

Figure 3. Wavefront Error At The Low Most Field

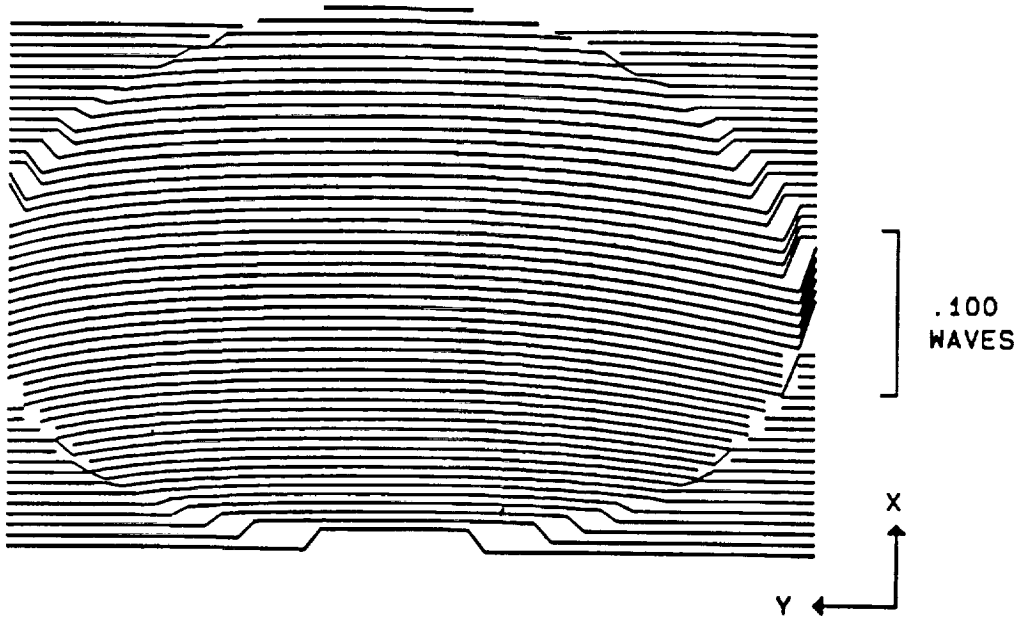

FRACTIONAL FIELD .0000 -1.0000 ID LID TELS QWAV BSPL DERO LAC LIDTQBDL1159
PUPIL 2 0 0 .1 -1 WAVELENGTH 2.06700

SEMI-FIELD = .0802 DEGREES SEMI-APERTURE = 250.0000 MM

Figure 4. Wavefront Error At The Right Most Field

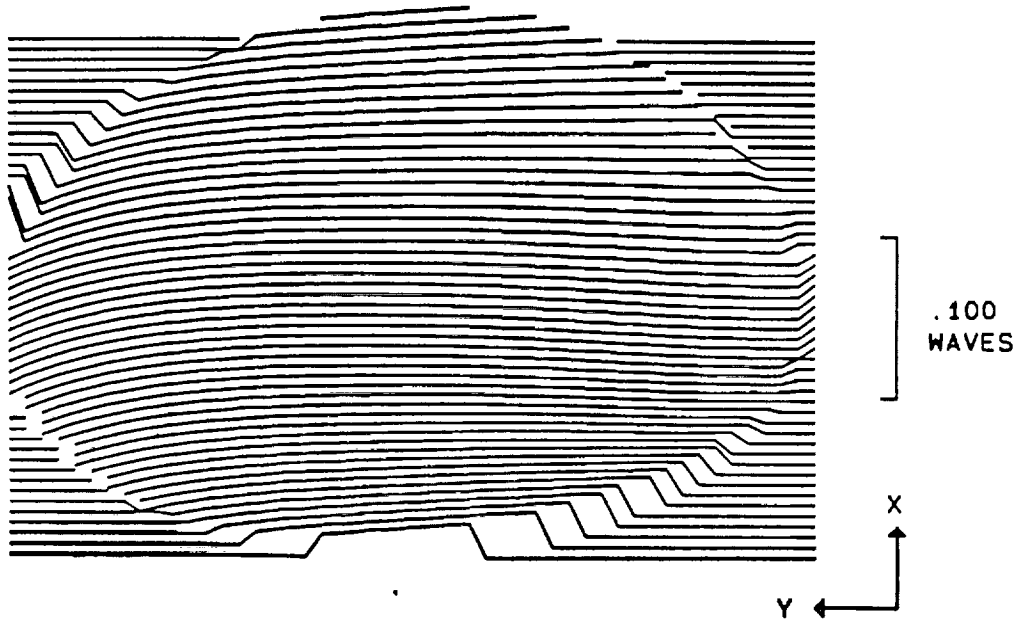

FRACTIONAL FIELD .0000 .0000 ID LID TELS QWAV BSPL DERO LAC LIDTQBDL1159
PUPIL 2 0 0 .1 0 WAVELENGTH 2.06700

Figure 5. Wavefront Error At The Center Of Field

6.2.2.3 BEAM POSITION SHIFT ON THE DETECTOR

The beam shift caused by the telescope distortions has been checked:

0.0166	mm	(At top most position of the field)
0.0173	mm	(At low most position of the field)
0.0119	mm	(At right most position of the field)

It can be seen that these shifts are negligible.

6.2.3 POLARIZATION

One common question to the off-axial telescope is the polarization. The high steep angle of incidence on the mirrors will introduce polarization changes. The polarization performance has also been checked for the telescope.

6.2.3.1 MIRROR COATING

An effective measure to solve the polarization problem is by using a suitable coating on the optics. The gold coating has been selected for the primary and secondary mirrors. Because of a very high reflectivity of the gold coating in the operating wavelength, the change in two components of the polarization must be within a few percent because the total reflectivity is the average of the two polarization components.

6.2.3.2 POLARIZATION ANALYSIS OF THE TELESCOPE

Figure 6 is the polarization map onto the field of the telescope mirrors. Figure 7 is the polarization map onto the entrance pupil for the telescope mirrors. The polarization ray trace shows the polarized throughputs for the mirror pair are:

Total	S-component	P-component
0.983	0.702	0.674

Table 1 is the polarization ray trace through the mirror pair.

Figure 8 is the polarization map onto the field for the complete telescope (mirror pairs, quarter wave plate and recollimating lens). Figure 9 is the polarization map onto the entrance pupil for the complete telescope. The polarized throughputs for the complete telescope are:

Total	S-component	P-component
0.366	0.423	0.433

Table 2 is the polarization ray trace trough the complete telescope. The reason for the low efficiency is because no coating has been considered on the quarter wave plate and recollimating lens at this time.

Table 1. Polarization ray trace through telescope mirrors.

pray 2 0 0 0 surf

SURF. NO.	MAGN.	X	Y	Z	PHASE
INCID. S 1	.707107E+00	.000000E+00	.707107E+00	.000000E+00	.000000E+00
INCID. P 1	.707107E+00	.707107E+00	.000000E+00	.000000E+00	.900000E+02
REFR. S 1	.707107E+00	.000000E+00	.707107E+00	.000000E+00	.000000E+00
REFR. P 1	.707107E+00	.707107E+00	.000000E+00	.000000E+00	.900000E+02
INCID. S 2	.707107E+00	.707107E+00	.000000E+00	.000000E+00	.900000E+02
INCID. P 2	.707107E+00	.000000E+00	.707107E+00	.000000E+00	.180000E+03
REFL. S 2	.704396E+00	.704396E+00	.000000E+00	.000000E+00	.884040E+02
REFL. P 2	.703837E+00	.000000E+00	.462439E+00	.530599E+00	.181926E+03
INCID. S 3	.704396E+00	.704396E+00	.000000E+00	.000000E+00	.884040E+02
INCID. P 3	.703837E+00	.000000E+00	.462439E+00	.530599E+00	.178074E+03
REFL. S 3	.701889E+00	.701889E+00	.000000E+00	.000000E+00	.266922E+03
REFL. P 3	.700333E+00	.000000E+00	.674395E+00	.188832E+00	.176000E+03
V1: (X,Y,Z),PHASE.	701889E+00	.000000E+00	.000000E+00	.266922E+03	
V2: (X,Y,Z),PHASE	.000000E+00	.674395E+00	.188832E+00	.176000E+03	
INTENSITY: APOD., POLAR., PROD.	.100000E+01	.983114E+00	.983114E+00		

Table 2. Polarization ray trace through telescope mirrors, quarter wave plate, and lens.
pray 2 0 0 0 surf

SURF. NO.	MAGN.	X	Y	Z	PHASE
INCID. S 1	.707107E+00	.000000E+00	.707107E+00	.000000E+00	.000000E+00
INCID. P 1	.707107E+00	.707107E+00	.000000E+00	.000000E+00	.900000E+02
REFR. S 1	.707107E+00	.000000E+00	.707107E+00	.000000E+00	.000000E+00
REFR. P 1	.707107E+00	.707107E+00	.000000E+00	.000000E+00	.900000E+02
INCID. S 2	.707107E+00	.707107E+00	.000000E+00	.000000E+00	.900000E+02
INCID. P 2	.707107E+00	.000000E+00	.707107E+00	.000000E+00	.180000E+03
REFL. S 2	.704396E+00	.704396E+00	.000000E+00	.000000E+00	.884040E+02
REFL. P 2	.703837E+00	.000000E+00	.462439E+00	.530599E+00	.181926E+03
INCID. S 3	.704396E+00	.704396E+00	.000000E+00	.000000E+00	.884040E+02
INCID. P 3	.703837E+00	.000000E+00	.462439E+00	.530599E+00	.178074E+03
REFL. S 3	.701889E+00	.701889E+00	.000000E+00	.000000E+00	.266922E+03
REFL. P 3	.700333E+00	.000000E+00	.674395E+00	.188832E+00	.176000E+03
INCID. S 4	.701889E+00	.701889E+00	.000000E+00	.000000E+00	.930783E+02
INCID. P 4	.700333E+00	.000000E+00	.674395E+00	.188832E+00	.176000E+03
REFR. S 4	.689244E+00	.689244E+00	.000000E+00	.000000E+00	.930783E+02
REFR. P 4	.690166E+00	.000000E+00	.677911E+00	.129483E+00	.176000E+03
INCID. S 5	.689244E+00	.689244E+00	.000000E+00	.000000E+00	.930783E+02
INCID. P 5	.690166E+00	.000000E+00	.677911E+00	.129483E+00	.176000E+03
REFR. S 5	.676828E+00	.676828E+00	.000000E+00	.000000E+00	.930783E+02
REFR. P 5	.680148E+00	.000000E+00	.654957E+00	.183390E+00	.176000E+03
INCID. S 6	.676828E+00	.676828E+00	.000000E+00	.000000E+00	.930783E+02
INCID. P 6	.680148E+00	.000000E+00	.654957E+00	.183390E+00	.176000E+03
REFR. S 6	.535197E+00	.535197E+00	.000000E+00	.000000E+00	.930783E+02
REFR. P 6	.542261E+00	.000000E+00	.536572E+00	.783381E 01	.176000E+03
INCID. S 7	.535197E+00	.535197E+00	.000000E+00	.000000E+00	.869217E+02
INCID. P 7	.542261E+00	.000000E+00	.536572E+00	.783381E 01	.400035E+01
REFR. S 7	.422707E+00	.422707E+00	.000000E+00	.000000E+00	.869217E+02
REFR. P 7	.432827E+00	.000000E+00	.432827E+00	.586503E 05	.400035E+01
V1: (X,Y,Z),PHASE		.422707E+00	.000000E+00	.000000E+00	.869217E+02
V2: (X,Y,Z),PHASE		.000000E+00	.432827E+00	.586503E 05	.400035E+01
INTENSITY: APOD., POLAR., PROD.		.100000E+01	.366021E+00	.366021E+00	

The coating design has not been completed for the rest of the optics.

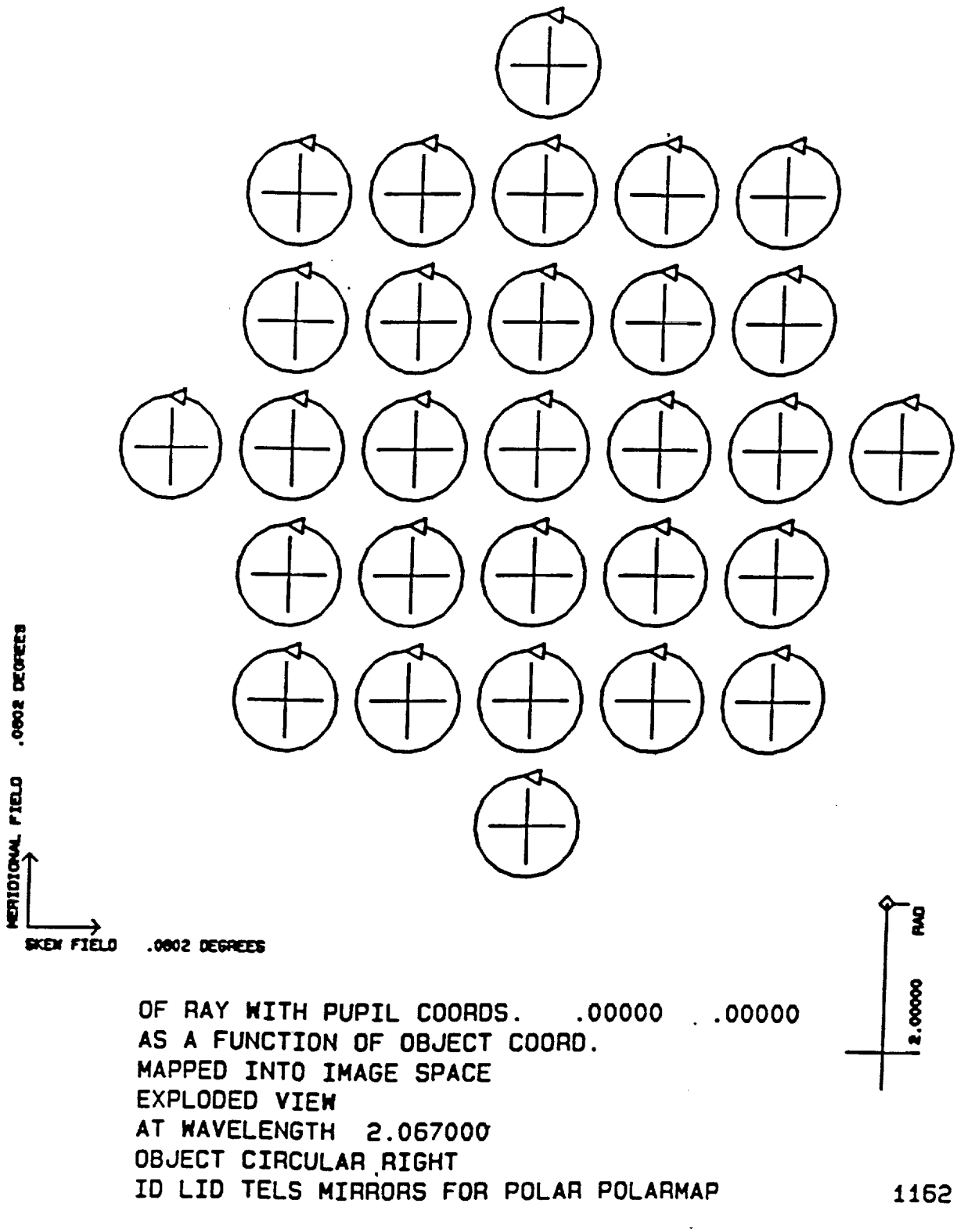

Figure 6. Polarization Map Over The Field For The Mirror Pair

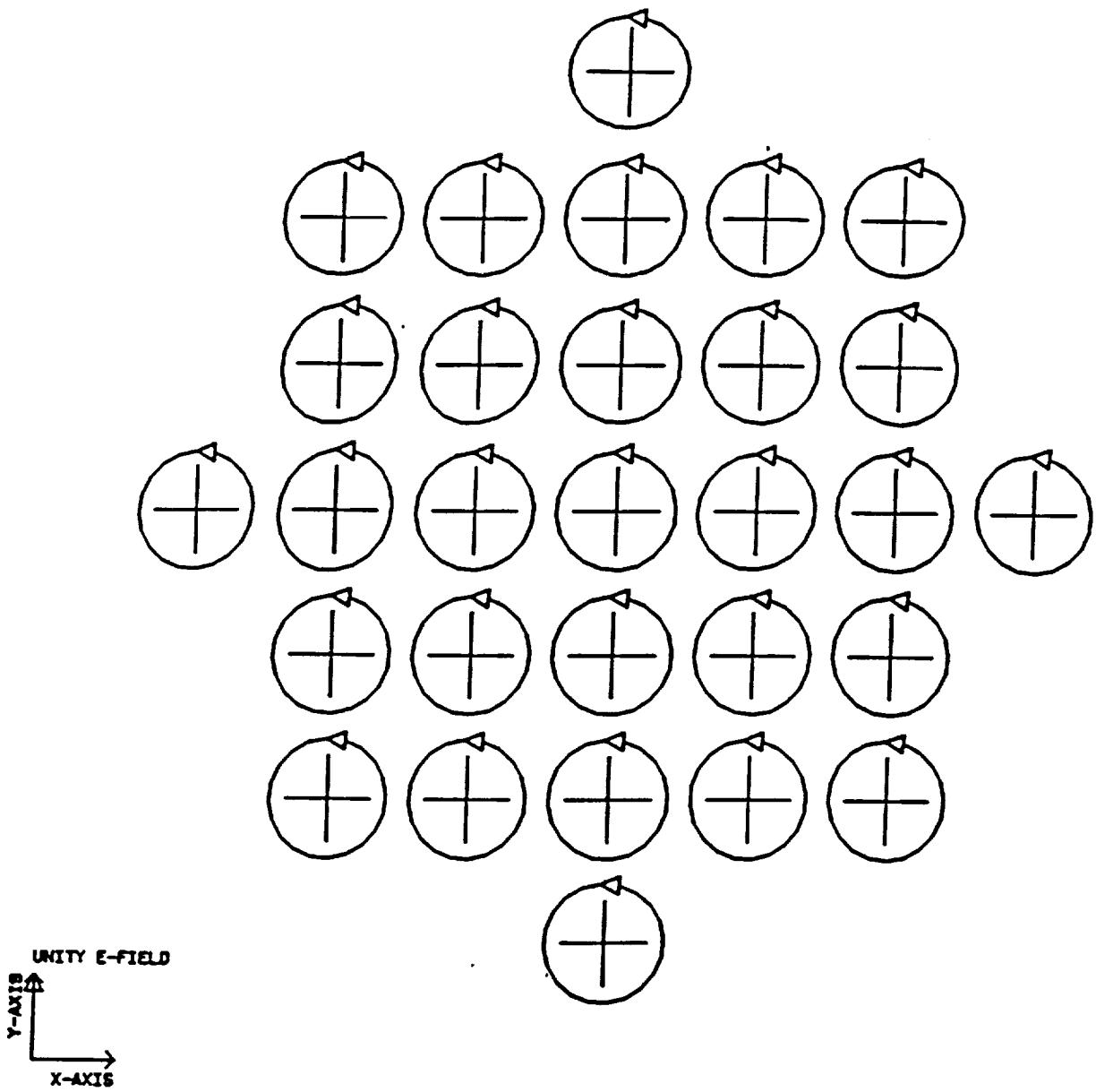

Figure 7. Polarization Map Over The Pupil For The Mirror Pair

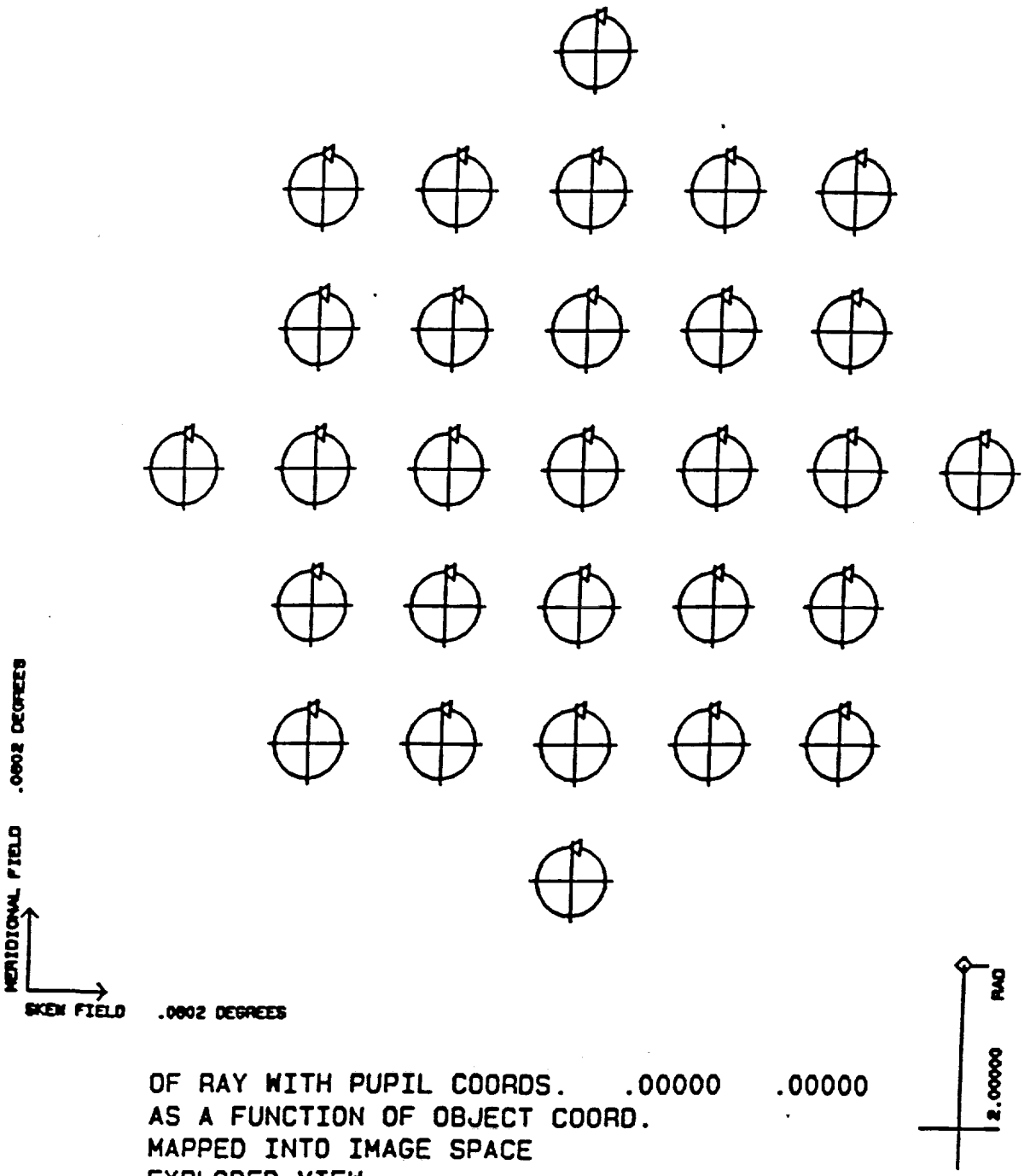

Figure 8. Polarization Map Over The Field For The Complete Telescope

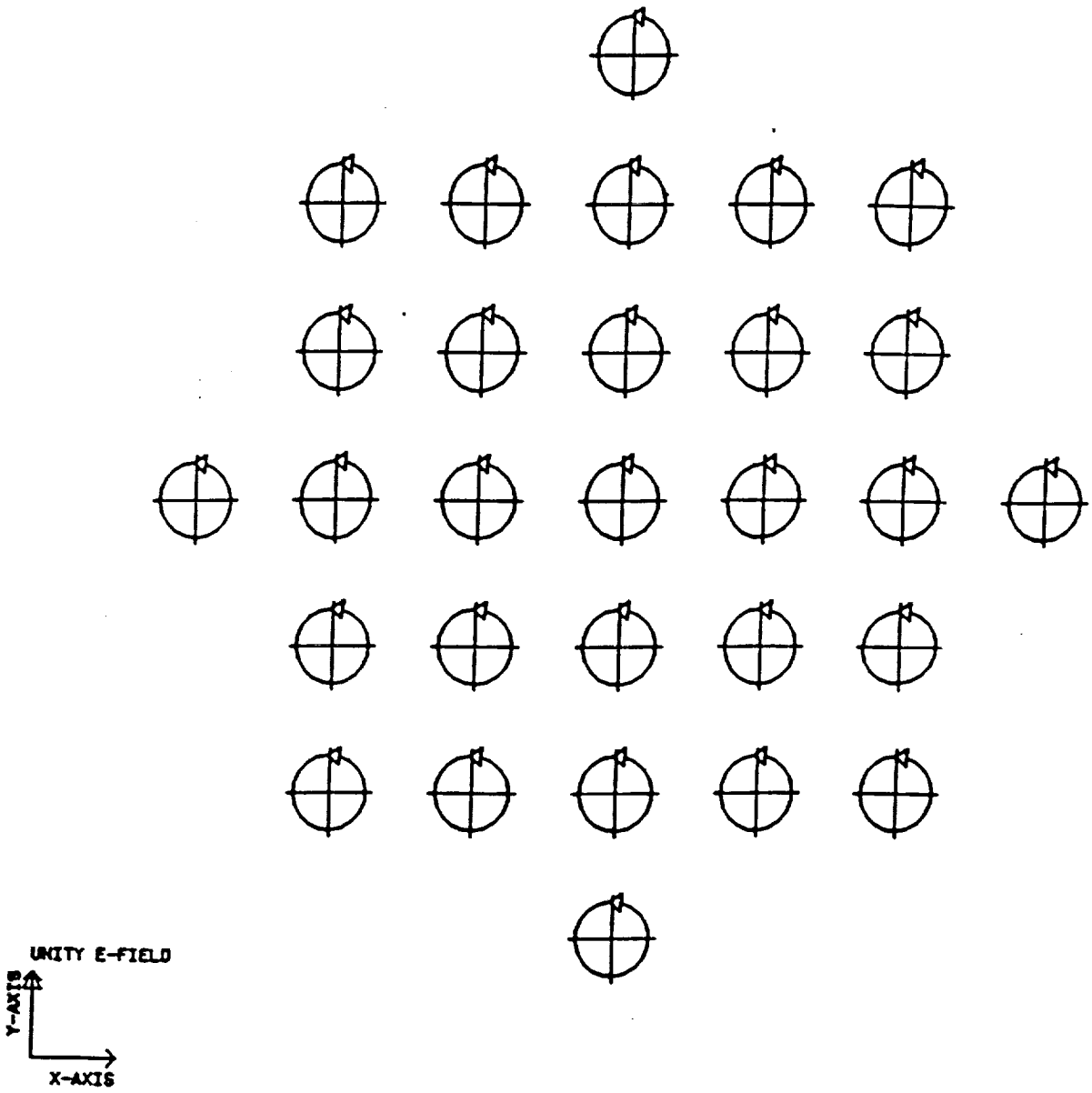

Figure 9. Polarization Map Over The Pupil For The Complete Telescope

6.3 SENSITIVITY ANALYSIS

Sensitivities for each part of the optical system have been checked by varying one parameter at a time in the complete system to evaluate its effect on the overall performance. The performance degradations are rms wave front error, boresight error, and beam shift on the detector. The wave front errors are in wave at 2.067 micron. The boresight errors are in micro-radians in the object space. The beam shift errors are in mm at the detector surface. The parametric errors are decenters, tilts, thickness error, and wedge error for each optical element. The decenter and thickness errors are in mm, while the tilt and wedge errors are in milli-radians.

Table 3 lists all the sensitivities with parametric errors and the corresponding performance errors. The sensitivities which are not listed are much looser than 1 mm in length and 1 milli-radians in angle.

6.3.1 PRIMARY AND SECONDARY MIRRORS

Because of the non-symmetrical nature of the off-axis telescope, all six parametric errors are independent for each mirror. The linear displacement errors are on the order of 0.01 mm and contribute a little over 1/10 wave rms wave front errors. The angular errors are on order of 0.01 milli-radians for the primary and 0.10 milli-radians for the secondary to introduce a little under 1/10 wave rms wave front errors. Some numbers are not symmetrical in sign. The most sensitive values are listed for these non-symmetrical parameters. The most sensitive displacement is the axial spacing. A 0.01 mm axial position change for the secondary mirror will introduce a 0.161 wave rms wave front error. The most sensitive tilt is the tilt around x-axis. A 0.01 milli-radians change in the primary mirror will introduce a 0.056 wave rms wavefront error.

The secondary mirror has been designed to have lower tilt sensitivities are lower because it is difficult to maintain the angular position to tight tolerances on a small mirror.

6.3.2 QUARTER WAVE PLATE

The quarter wave plate will introduce errors because it is located in the convergent ray path. The quarter wave plate is simply a plate with a symmetrical shape. Only tilt, thickness, and wedge errors have been checked. The thickness error of 0.01 mm will introduce a 0.079 wave rms wave front error. A 10.0 milli-radians of tilt and 1.0 milli-radians rotation will introduce 0.022 wave and 0.061 wave rms wave front error respectively.

The axial location of the quarter wave plate almost has no effect on the performance.

6.3.3 COLLIMATING LENS

The collimating lens is also working at off-axis. All six possible variations have been checked. As compared to the primary and secondary mirrors, the collimating lens has much lower sensitivities. The axial displacement of 0.01 mm will introduce a 0.023 wave rms wavefront error.

In real practice, this axial displacement can be used to fine tune the wavefront performance to compensate for the errors caused by the element fabrication, assembly and alignment. The in-plane location of the lens has a range of 0.1 mm. Tilts are of the order of 1.0 milli-radians. The in plane rotation can be 10.0 milli-radians. The wedge in two directions is 1.00 milli-radians. The reason for lower sensitivities of the lens as compared to the mirror is that the two surfaces of the lens are close a parallel surface. When both surfaces are displaced together, the effects are partly canceled.

6.3.4 CUBIC BEAMSPLITTER

A cubic beamsplitter is located in the collimated beam path. The effect on the wave front performance is very low just as for the rest of the optical parts. However, any changes in these parts will introduce a boresight error or a beam shift on the detector. A thickness change of 1.00 mm will introduce a 0.011 mm beam position on the final detector.

The effect of the beamsplitter position error is essentially none.

6.3.5 BEAM DEROTATOR

The axial position of the derotator will introduce a beam shift only. A 1.00 mm of axial displacement will create a 0.037 mm beam shift on the detector. The thickness of the derotator also introduces a beam shift. In real practice, the axial position of the derotator can be used to compensate for the fabrication error of the derotator thickness. A tilt change in the derotator only introduces a boresight error. The wedge angle also introduces a boresight error. Again, the tilt angle can be used to compensate for the fabrication error of the derotator wedge. The synchronous error (clocking angle) of 1.00 milli-radiance of the derotator will introduce a 1.400 micron radians of the boresight error in the object space. The center of the derotator should be on the center of the beam. Any error in the axis offset will cause a residual beam shift in the same amount.

6.3.6 LAG ANGLE COMPENSATOR

The lag angle compensator is a simple flat mirror. A change of 0.01 mm in the normal position of this mirror surface will introduce a 0.014 mm beam position on the detector. The two directional tilts will introduce a boresight change of 0.56 micron radians and 0.8 micron-radians respectively for a 0.01 milli-radians changes in the tilt angle. These two ratios are the angular transfer function of the lag angle compensator needed for programming of the lag angle compensator controller. All sensitivities are the effects of one parameter at a time. The combination of the errors needs a more detailed modeling. One simple estimate can be made based on statistically reducing the values by square root of the number of the dominant variables. The dominant variables are those which are hard to fabricate or align.

Table 3. Parametric Sensitivities

Primary mirror						
Decenter	X	0.01	mm	0.108	wave	rms wavefront
Decenter	Y	0.01	mm	0.148	wave	rms wavefront
Decenter	Z	0.01	mm	0.143	wave	rms wavefront
Tilt	X	0.01	mr	0.056	wave	rms wavefront
Tilt	Y	0.01	mr	0.035	wave	rms wavefront
Tilt	Z	0.01	mr	0.041	wave	rms wavefront
Secondary mirror						
Decenter	X	0.01	mm	0.104	wave	rms wavefront
Decenter	Y	0.01	mm	0.141	wave	rms wavefront
Decenter	Z	0.01	mm	0.161	wave	rms wavefront
Tilt	X	0.10	mr	0.098	wave	rms wavefront
Tilt	Y	0.10	mr	0.065	wave	rms wavefront
Tilt	Z	0.10	mr	0.063	wave	rms wavefront
Quart wave plate						
Tilt		10.0	mr	0.022	wave	rms wavefront
Thickness		0.01	mm	0.079	wave	rms wavefront
Wedge		1.00	mr	0.061	wave	rms wavefront
Collimating lens						
Decenter	X	0.10	mm	0.044	wave	rms wavefront
Decenter	Y	0.10	mm	0.074	wave	rms wavefront
Decenter	Z	0.01	mm	0.023	wave	rms wavefront
Tilt	X	1.00	mr	0.027	wave	rms wavefront
Tilt	Y	1.00	mr	0.021	wave	rms wavefront
Tilt	Z	10.0	mr	0.080	wave	rms wavefront
Thickness		0.01	mm	0.028	wave	rms wavefront
Wedge	X	1.00	mr	0.096	wave	rms wavefront
Wedge	Y	1.00	mr	0.027	wave	rms wavefront
Cubic beam splitter						
Thickness		1.00	mm	0.011	mm	shift on detector
Beam derotator						
Axial position		1.00	mm	0.037	mm	shift on detector

Tilt		1.00	mr	1.640	μr	boresight error
Synchronous		1.00	mr	1.400	μr	boresight error
Thickness		0.10	mm	0.058	mm	shift on detector
Wedge		0.01	mm	1.880	μr	boresight error
Lag angle compensator						
Normal position		0.01	mm	0.014	mm	shift on doctor
Tilt	X	0.01	mr	0.560	μr	boresight error
Tilt	Y	0.01	mr	0.800	μr	boresight error

6.4 SYSTEM DATA

Figures 10 and 11 are the side and top views of the telescope optics. Some dimensions are somewhat arbitrary, such as the distance between the derotator and the lag angle compensator, and the distance between lag angle compensator and detector. Table 4 lists the detailed prescription of the optical system.

Table 4. Optical System Prescription

SPECIFICATION
ID LID TELS QWAV BSPL DERO LAC LIDTQBDL 1163

OBJ. DIST.	INFINITE	FOCAL LENGTH	8546887.5629
OBJ. HEIGHT	INFINITE	BACK FOCAL DIST.	.0000
MARG. RAY HEIGHT	250.0000	PARAXIAL FOCAL P.	.0000
CHIEF RAY HEIGHT	.0000	OVERALL LENGTH	204.8175
MARG. RAY ANGLE	.0000	ENTR. PUPIL POS.	.0000
CHIEF RAY ANGLE	.0802	EXIT PUPIL POS.	374.5564
DIAM	20.0209	GAUSSIAN IM. HT.	.0350
X OBJ. HEIGHT	INFINITE	X CHIEF RAY HT.	.0000
X CHIEF RAY ANGLE	.0802	X MARG. RAY HT.	250.0000

WAVELENGTHS 2.07700 2.06700 2.05700
UNITS MM
STOP IS ON SURF. NO. 1
AFOCAL MAGNIFICATION 25.0013
GLOBAL OPTION IS ON

SURF. NO.	RADIUS	THICKNESS	MEDIUM
1	INFINITE	450.00000	AIR
2A	824.26305	350.00464	AIR

CONIC B	.824263E+13			
AXES A	.824263E+08	CC	.100000E+01	
3	177.98218	131.72514	AIR	
CONIC B	.717861E+02			
AXES A	.113034E+03	CC	.347934E+01	
4	INFINITE	6.00000	FUSILICA	1.43719T 1452.40 UNUSUAL
5	INFINITE	10.00000	AIR	
6	158.85656	10.00000	GE	4.10079T 1419.10 UNUSUAL
CONIC B	.607521E+03			
AXES A	.310658E+03	CC	.738517E+00	
7	78.05914	20.00000	AIR	
CONIC B	.176761E+03			
AXES A	.117464E+03	CC	.558392E+00	
8	INFINITE	30.00000	FUSILICA	1.43719T 1452.40 UNUSUAL
9	INFINITE	.00000	AIR	
10A	INFINITE	30.00000	AIR	
11A	INFINITE	7.09703	GE	4.10079T 1419.10 UNUSUAL
12A	INFINITE	.00000	AIR	
13	INFINITE	.00000	AIR	
14	INFINITE	60.0000	AIR	
15A	INFINITE	.00000	AIR	
16A	INFINITE	200.0000	AIR	
17	INFINITE	.00000	AIR	
18	INFINITE	.3422E+06	AIR	

NOTE: ITEMS MARKED "P" OR "S" ARE SUBJECT TO PICKUPS OR SOLVES

DEFORMATION COEFFICIENTS

TILTS AND DECENTERS ALPHA,BETA,GAMMA,AXIS
X DECN,YDECN,ZDECN

2 TDC 39 SURFACES			
.000000E+00	.000000E+00	.000000E+00	.000000E+00
.000000E+00	.375000E+03	.000000E+00	
10 TDC 29 SURFACES			
.000000E+00	.000000E+00	.000000E+00	.000000E+00
.000000E+00	.150000E+02	.000000E+00	
11 TDC 3 SURFACES			
.450000E+02	.000000E+00	.000000E+00	.000000E+00
.000000E+00	.000000E+00	.000000E+00	
12 TDC 1 SURFACES			

```
 .418911E+00   .000000E+00   .000000E+00   .000000E+00
 .000000E+00   .000000E+00   .000000E+00

SURFACE NO. 13 WILL UNDO TDC OF NO. 12
SURFACE NO. 14 WILL UNDO TDC OF NO. 11

 15   TDC  19 SURFACES
 .000000E+00   .450000E+02   .000000E+00   .000000E+00
 .000000E+00   .000000E+00   .000000E+00
 16   TDC   9 SURFACES
 .000000E+00   .450000E+02   .000000E+00   .000000E+00
 .000000E+00   .000000E+00   .000000E+00
```

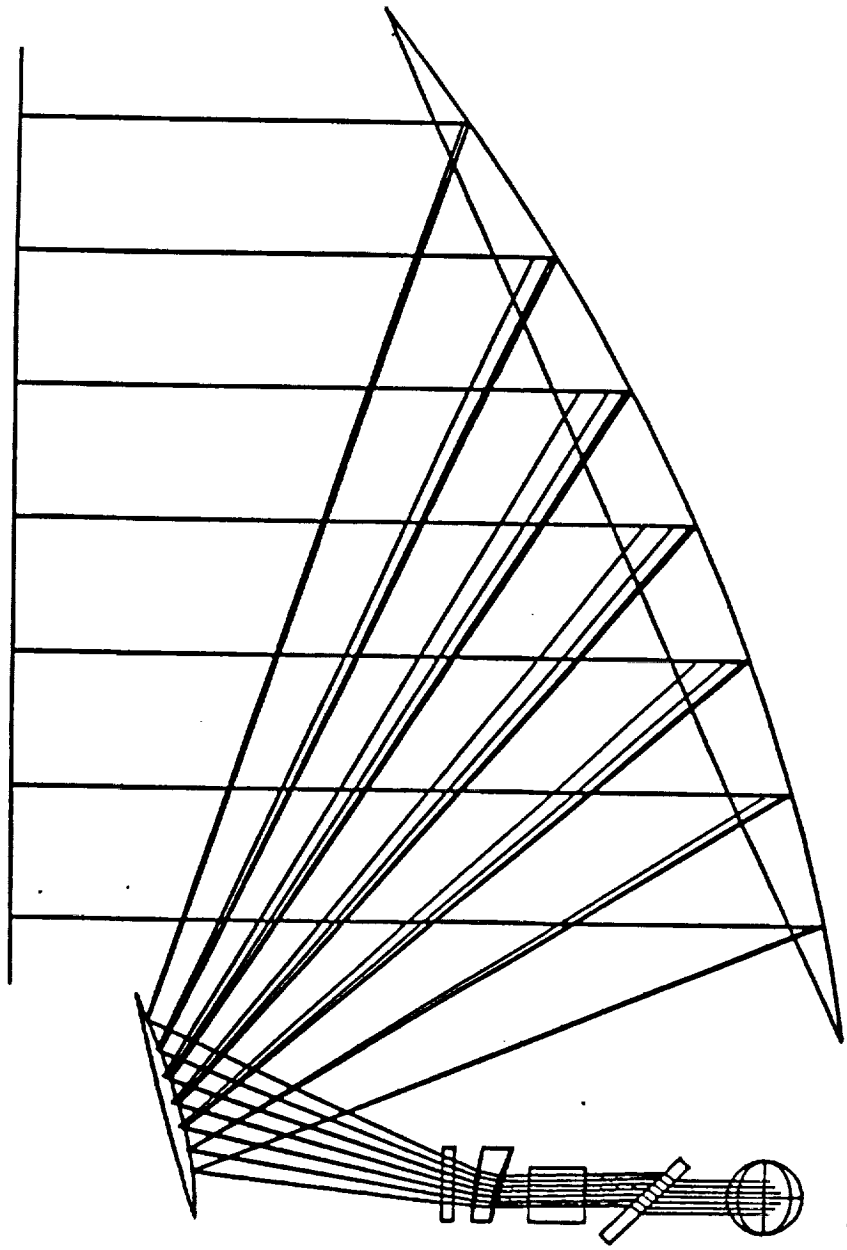

Figure 10. Optical System Side View

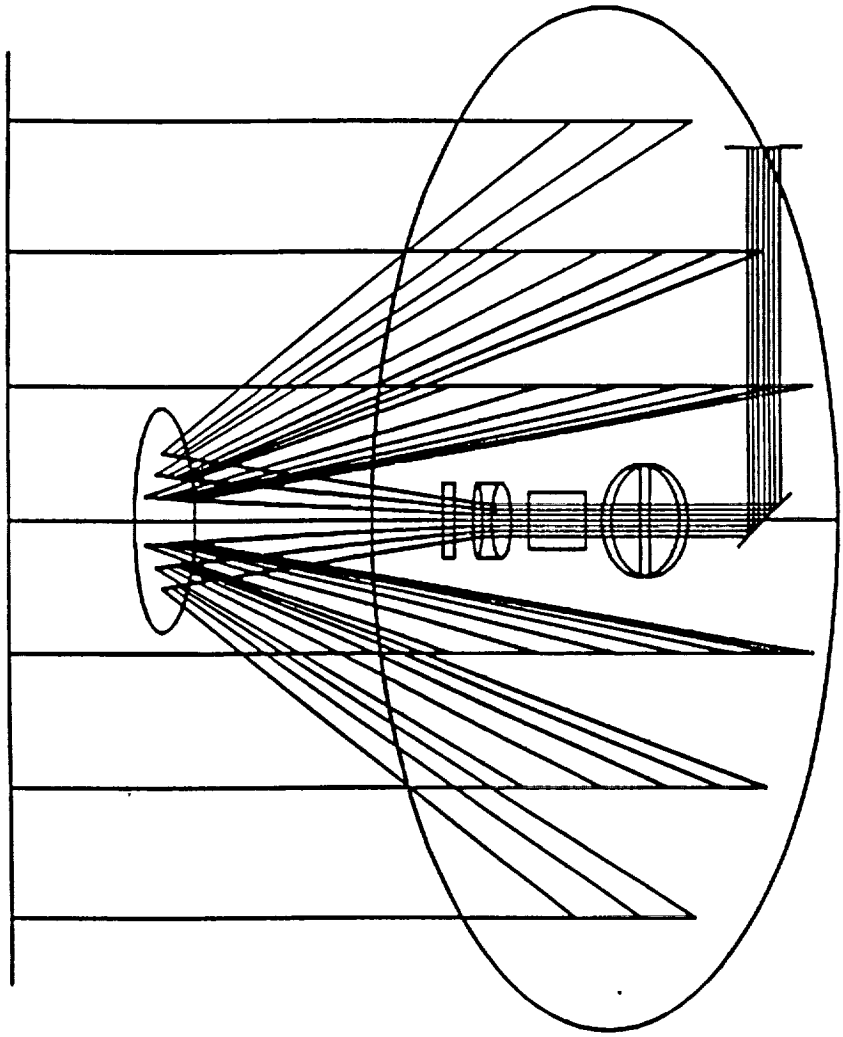

AZIMUTH .000 SCALE .250
ELEVATION 90.000 ID LID TELS QWAV BSPL DERO LAC LIDTQBDL 1157

Figure 11. Optical System Top View

6.4.1 TELESCOPE

The telescope consists of three optical elements with power:

Primary mirror

Radius of curvature	824.2631	mm	(Concave)
Conic constant	-1.0		(Paraboloid)

Secondary mirror

Radius of curvature	177.9822	mm	(Convex)
Conic constant	-3.47934		(Hyperboloid)

Recollimating lens

Radius of curvature 1	158.8566	mm	(Convex)
Conic constant	-0.7385		(Elliposoid)
Radius of curvature 2	78.0591	mm	(Concave)
Conical constant	-0.5584		(Elliposoid)
Central thickness	10.0000	mm	
Material		Germanium	

The fused silica quarter wave plate is located in front of the recollimating lens with a thickness of 6 mm. Figure 12 shows the telescope assembly and the support structure. A more detail description of the telescope mechanical design can be found in the SPIE Proceedings of the International Symposium on Optical Science, Engineering, and Instrumentation, V. 2540, P. 68-76. A copy of this paper is provided in section 8.2 of this report.

6.4.2 DE-ROTATOR

The monolithic beam derotator (see chapter 4.0) is made up of germanium. The tilt angle is 45 degrees (the angle between the normal of front surface and the rotational axis). The wedge angle is 4.1891 degrees, i.e. the angle between front and back surface. The central thickness is 7.0970 mm. The wedge angle error caused by fabrication can be compensated by adjusting the tilt angle. The thickness error can be compensated by adjusting the axial location of the derotator. However, the linear beam offset caused by thickness error will be very small compared to the system requirement. The axial adjustment may not be necessary. The angular offset caused by the wedge angle error must be compensated to satisfy the system boresight requirements. See the Sensitivity section for the details.

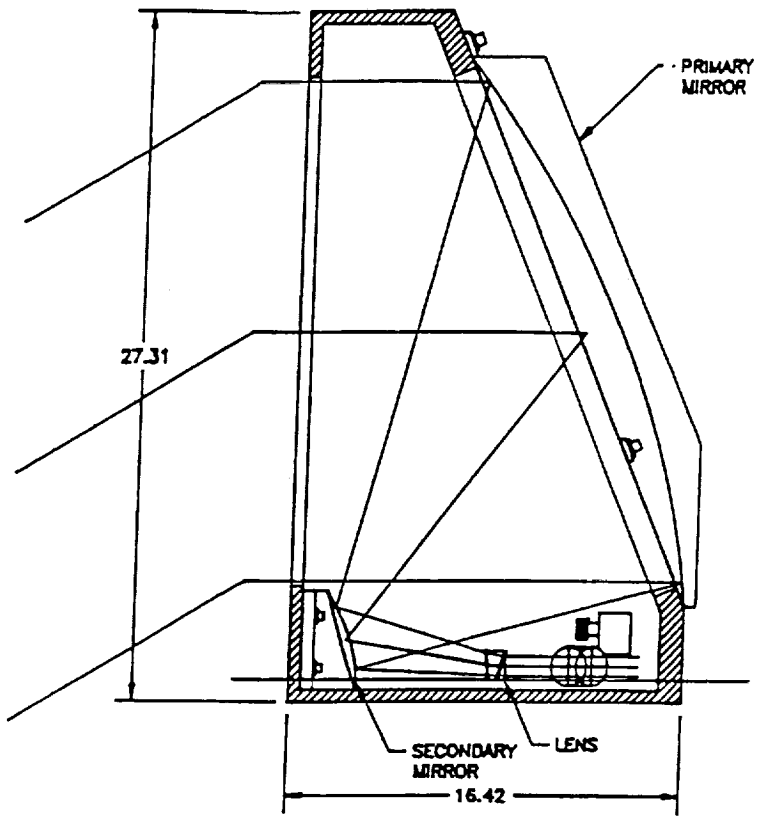

Figure 12. Telescope assembly showing the mirros, lens and the support structure.

6.4.3 LAG ANGLE COMPENSATOR

The lag angle compensator is a simple two-dimensional electro-mechanical addressable folding mirror. The angular beam offset caused by scanning and satellite motion can be compensated by correctly driving the mirror. The linear beam offset on the final detector by this mirror tilts is very small because the tilt angles are very small and the separation between the telescope exit pupil to the lag angle compensator is also small. The linear beam offset on the final detector is the product of lag angle and pupil distance. For the dynamic lag angle change of 80 micron-radians and pupil distance of 175 mm:

$$\text{Linear offset} = 80 \text{ X } 10^{-6} * 175 * 25 = 0.35 \text{ mm}$$

Where 25 is the telescope magnification. The linear bean offset is only 1.75 % of the 20 mm beam diameter.

The transfer functions of the lag angle compensator are linear factors of 0.71429 and 0.5 (ratio of mirror tilt and beam deviation) for the horizontal and vertical directions respectively. The tilt ranges for the 80 micro radians dynamic lag angle are:

Horizontal range = 0.71429 * 80 * 25 = 1.4286 milliradians

Vertical range = 0.5 * 80 * 25 = 1.0 milliradians

The accuracy of the mirror positions for the 1 micro radians of system boresight requirement are:

Horizontal range = 0.71429 * 1 * 25 = 17.8573 micro radians

Vertical range = 0.5 * 1 * 25 = 12.5 micro radians

The swing rates of the mirrors for the 160 microseconds pulse reception time are:

Horizontal rate = 0.001429 / 0.00016 = 8.931 radians/second

Vertical rate = 0.001 / 0.00016 = 6.25 radians/second

6.0 RECOMMENDED FURTHER WORK ON OPTICAL SUBSYSTEM

A preliminary analysis was performed on the performance and tolerances for a 250 mm version of the telescope described in this chapter. The results of this analysis indicate that a 250 mm telescope will have the same type of fabrication and alignment tolerances as the 500 mm telescope. For a 250 mm telescope, the decenter tolerances are basically identical to those of the 500 mm telescope. But the tilt tolerances mostly increase for the 250 mm telescope. To fully predict the 250 mm telescope performance and to determine its tolerances, some additional work is required.

Other recommended future work include a complete coating design is needed for all the elements. Upon completion of the coating design, a detail polarization analysis is necessary to accurately determine the effects of the optical subsystem on the lidar overall performance. Excess scattering of the transmitter beam off the optical components may disrupt the operation of the lidar detector. Therefore, a scattering analysis must be performed to determine the level of the scattered laser beam radiation that is collected by the heterodyne receiver. Finally, it is recommended to perform a complete system performance modeling and analysis to allow the lidar design optimization.

7.0 LIDAR COMPUTER DATABASE AND WORLD WIDE WEB SERVER

The NASA/MSFC lidar computer database, previously developed the UAH personnel, was upgraded and a large number (>400) of lidar related materials were added to the database. After completing the entry of all the lidar related materials in the MSFC/EO Branch into the database, the other sources of lidar materials within MSFC were identified. Most of these materials were added to the database bringing the total number of entries to more than 1750 items which include about 1230 journals, 460 reports and technical memorandums, and 60 books, theses and proposals. The database software was further enhanced by incorporating an automatic file folder label generator for all new database entries. In addition, a page scanner hardware and an Optical Character Recognition (OCR) software were installed to improve the data entry process. This scanner system will also support the World Wide Web (WWW) server development effort.

A WWW server was developed to familiarize the industry, academic and other government agencies with the MSFC coherent lidar activities and to provide them with an efficient means of accessing the E-O branch information base through computer networks. The Hyper Text Transfer Protocol (HTTP) server software, developed by the National Center for Supercomputing Applications (NCSA), was installed on a PC dedicated to the WWW. Both SUN PC-NFC and Novell LAN Workplace networking software were evaluated for interfacing with the internet. The Novell LAN Workplace was then selected and installed on the PC. The server was then tested using NCSA Mosaic on different SUN SPARC stations and a MacIntosh computer to ensure proper transfer of information through the internet and the document format compatibility with different computers. After some modifications, it was shown that the server can be run at near full capacity. A great deal of materials relating to the E-O branch and the coherent lidar field have been placed on the server. These materials were prepared specifically for the WWW by the members of E-O branch and the UAH personnel. The server documents, which include text, mathematical expressions and images, were first transferred to the PC and then edited and converted to the proper format for the server using HTML Assistant word processor. The documents that are presently available on the server include: tutorials on coherent lidar technique and its applications, some of the current activities and projects, past accomplishments, a recent review paper that appeared at a SPIE proceeding, and spin-off technologies. The breakdown of the MSFC electro-optics branch WWW server are as following:

- 84 HTML documents 205 KB
- 20 in-lined GIF images 315 KB
- 20 JPEG images 1.60 MB
- Total 2.10 MB

In order to accommodate for the increasing number accesses and links to other severs, and to allow the addition of more documents, and to provide a reliable and uninterrupted service, the server computer was upgraded from a 386SX25 machine with 4 MB of RAM to a 486DX66 with 16 MB of RAM. The server resource configuration was then modified to take advantage of more

available memory and to increase the speed of the server in responding to its users and fulfilling their requests. The UAH personnel also monitored the server traffic and maintained statistical record on the server usage on the daily basis. A backup procedure was also developed to regularly store the server documents to data tapes as an added precaution for uninterrupted service to the interested organizations throughout the world.

8.0 RELATED ACTIVITIES

8.1 NASA SENSOR AND NOAA SPACE-BASED LIDAR WORKING GROUP MEETINGS

UAH personnel attended the NASA Sensor Working Group Meeting on September 21-22, 1994 in New Carrollton, MD. In this meeting, the capabilities of the DCF and the status of its development was presented and the results of the measurements performed in the companion Laser Characterization Facility (LCF) on a 2-micron coherent lidar transceiver, developed by the U.S. Air Force, were described. UAH personnel also participated in a technical coordination meeting for the NASA solid state coherent lidar program at MSFC on November 15, 1994. In addition to MSFC and UAH, this meeting was attended by representatives from Jet Propulsion Laboratory and the Langley Research Center.

UAH personnel attended two Meetings of the NOAA Working Group on Space-Based Lidar Winds in Clearwater, Florida (January 31-February 2, 1995) and in Frisco, Colorado (July 19-21, 1995). The status of the NASA/MSFC and UAH 2-micron solid state coherent lidar efforts were described in these meetings.

8.2 CONFERENCES

Three conference papers, describing some of the work performed under this deliver order, were prepared and presented at the SPIE International Symposium on Optical Science, Engineering, and Instrumentation, in San Diego, California, July 9-14, 1995 AND the Coherent Laser Radar Topical Meeting in Keystone, Colorado, July 23-27, 1995. The followings provide the summaries of these papers.

SPIE Int. Symposium on Opt. Sci., Engin., and Instrumentation San Deigo, CA., July 9-14 1995

Design and analysis of a spaceborne lidar telescope

Chen Feng, Anees Ahmad and Farzin Amzajerdian

Center for Applied Optics
The University of Alabama in Huntsville
Huntsville, AL35899

ABSTRACT

A spaceborne telescope has been designed and analyzed for a 2-micron solid state coherent lidar system operating on a satellite. The optical system consists of a large off-axis reflective telescope, a large-aperture diffractive scanner, an image derotator and a lag angle compensator. Due to the orbiting motion of the satellite and scanning, the boresight of the telescope shifts during the round trip travel time of the laser pulses to the target. In a coherent lidar system utilizing optical heterodyne detection, the relative alignment of the received signal with respect to the local oscillator beam is particularly critical. Two compensators have been designed to correct the boresight errors as well as the wavefront errors caused by beam wandering due to the boresight changes. Several design approaches for the compensators have been investigated. The optical and optomechanical design issues for such a system are discussed. The results of optical performance, modeling and tolerance analysis for the telescope are also presented.

Keywords: optical design and modeling, large reflective optics, diffractive optics, tolerance analysis, boresight shift compensation, lidar, coherent laser radar, satellite

1. INTRODUCTION

Several studies have indicated that the optimum approach to measure atmospheric wind from space is a pulsed coherent lidar[1,2]. However, these studies recommended a pulsed CO_2 laser radar system, operating at 10 micron wavelength with a pulse energy of near 20 J, pulse repetition frequency (PRF) of about 5 Hz, optical aperture of approximately 1.6 m, and full-time operation (100% on- orbit duty cycle). These requirements are too expensive. The size, weight, and energy consumption for such a system are beyond the capability of small satellites. NASA's Marshall Space Flight Center (MSFC) has, therefore, initiated an investigation to address innovative designs of a space-based coherent lidar system, which are smaller, lighter, less expensive, and consume less power [3]. The Center for Applied Optics (CAO) has recently conducted an optical design of the telescope and its associated optical subsystems for the new compact coherent lidar.

The new lidar optical system consists of a holographic optical element (HOE) beam scanner, an off-axis beam expanding telescope, a wedge derotator, and a two-dimensional lag angle compensator. The size, weight and complexity of this new system are substantially reduced as compared to the optical systems previously proposed for a space-based coherent lidar[4,5]. In addition, the parametric sensitivities of this system design make its implementation achievable at a much reduced fabrication and integration cost.

When the various requirements of the mission that must be achieved simultaneously are considered from a system perspective, the sensor of choice for this mission is a solid state pulsed coherent lidar operating at 2-micron wavelength. The lidar utilizes a relatively high power, pulsed laser as the transmitter and a low power, continuous-wave laser as the local oscillator source. The transmitter laser is injection locked to produce single frequency pulses using a highly stable, single frequency, continuous-wave, master oscillator laser. Part of the master laser is also used for controlling the local oscillator laser frequency that varies with the scanner position to compensate the gross spacecraft-induced Doppler frequency shift. The use of a frequency-tunable local oscillator laser relaxes the bandwidth requirements of the lidar detector and the processing electronics.

A simplified schematic of a pulsed coherent lidar is shown in Figure 1. The pulsed laser output beam is expanded by an off-axis telescope to be transmitted to the atmosphere. The quarter-wave plate placed along the propagation path changes the

0-8194-1899-4/95/$6.00

polarization of the transmitted beam from vertical to circular. The return beam from the atmosphere is received by the same telescope and directed through the quarter-wave plate and a polarizing beamsplitter toward the detector. The derotator and lag angle compensator (LAC) are placed along the return signal path to correct for the boresight and wavefront errors caused by the scanner and spacecraft motions. At the detector, the return radiation is mixed with the local oscillator beam for heterodyne detection. The detector in turn generates an electrical signal at the difference frequency between the signal and local oscillator frequencies. The output of the detector is then bandpass filtered and amplified to be digitized and processed for Doppler frequency shift due to the atmospheric winds.

Previous work [3,6] has specified the optimum laser pulse width and repetition rate at 200 nano-seconds and 10 Hz respectively, and has selected a telescope aperture diameter of 500 mm, and a scanner half-angle of 30 degrees for the space-based coherent lidar operating at 2-micron wavelength. For the purposes of this work, it has further been assumed that the spacecraft has a sun-synchronous orbit at 350 km above the sea level. The measurement range has been assumed to be from the ground-level to 20 km altitude.

2. OPTICAL SYSTEM DESIGN

The overall function of the coherent lidar optical system is to expand the laser beam, and direct it towards the atmosphere in a conical scan, to receive the backscattered radiation, and compensate for the wavefront and boresight errors caused by the scanner and spacecraft motions. The major requirements are: (1) beam expanding aperture of 500 mm; (2) input laser beam diameter of 20 mm; (3) conical scan rate of 10 RPM; (4) nadir angle of 30 degrees; (5) no internal focal point to avoid air break down in ground system testing; (6) diffraction limited beam quality; (7) lag angle compensation to maintain the boresight to within 1 micro-radian.

2.1 Beam expanding telescope

The beam expanding telescope is an off-axis catadioptric system, which serves both as the transmitter laser beam expander and as the receiver collecting telescope. Various configurations for the telescope have been evaluated against the performance requirements. An off-axis configuration has been selected to eliminate the central obscuration of an on-axis design, which degrades the beam quality due to the diffraction pattern of the obscuration. The off-axis configuration also effectively reduces the backscattering of the transmitted pulses by the front surface of the telescope secondary. A Galilean type of telescope has been employed to eliminate the real focus of the Keplerian type of telescope. The beam wander problem of a Galilean telescope (because of no real exit pupil) can be solved by using additional corrective optics. A catadioptric design with a refractive exit lens has been proposed to provide enough back-relief space to accommodate the beamsplitter, derotator and lag angle compensator. Figure 2 is the layout of a compact two-mirror one lens off-axis telescope.

The two mirrors are a parabola and a hyperbola as in a standard Cassegrain type of telescope. An aspheric negative lens has been used to recollimate the beam. The telescope has: (1) a field of view 0.17 degree to cover the lag angle of the return beam; (2) afocal magnification of 25X to expand the 20 mm beam to a 500 mm diameter; (3) RMS wavefront error of 1/10 wave at the exit pupil for 2.067 micron wavelength; (4) zero obscuration and vignetting; (5) no internal real focus; and (6) a mirror spacing of only 350 mm. Figure 3 shows the wavefront error of this telescope for the transmitted and return beams, and Figure 4 shows the point spread function in the telescope exit space for both the beams.

The flat field characteristic of this telescope design eliminates the need for any additional optics to compensate for the return beam angular deviations from the telescope optical axis that are caused by the scanner motion and lag angle. Furthermore, the pupil relay optics can also be omitted since the beam wander is only a few millimeters at the derotator input, which is located about 150 mm from the telescope exit lens. Figure 5 illustrates the layout of the lidar optical system including the telescope, scanner, derotator, and lag angle compensator.

2.2 Beam scanner

A Holographic Optical Element (HOE) scanner is being considered as a lightweight alternative to a wedge or prism scanner. A germanium prism with about 9 degree wedge angle is required for deflecting the laser beam through an angle of 30 degrees. Such a prism will be quite expensive, heavy and difficult to fabricate for the required 500 mm optical aperture. Since this application requires a simple conical scan of a monochromatic and collimated beam with a fixed deflection angle, a HOE scanner may be a viable choice. Compared with the wedge scanners, a HOE scanner will allow for much easier spacecraft accommodation because of its lower mass and symmetrical structure. Furthermore, HOE scanners do not suffer from phase domain limitations associated with the large diameter wedge scanners required for this application.

2.3 Beam derotator

The lidar scanner and platform motions during the transmitted pulse round-trip time cause the return beam to deviate from the optical axis established by the transmitter beam. Therefore, additional optical assemblies are required to compensate for these motions and maintain the relative alignment of the return and local oscillator beams during the pulse reception time. The return beam angular deviation or lag angle can be divided into two components, a dominant static component and a much smaller dynamic component. The scanner and orbital motion contributions to the static component of the lag angle are about 1400 and 3 micro-radians, respectively, and their contributions to the dynamic component of the lag angle are 80 and 0.18 micro-radians. The static component of the lag angle is compensated by an optical subsystem, referred to as the derotator, and its dynamic component is corrected by the lag angle compensator (LAC) subsystem.

The derotator employed in the earlier designs utilized a two mirror periscope that rotates with the scanning telescope to maintain a fixed separation between the transmitted and return beams while eliminating the return beam motion. To further simplify the optical system design and improve its robustness, a single optical wedge has been utilized to perform as the signal beam derotator. The derotator wedge is placed about 150 mm from the telescope exit lens at 45 degrees with respect to the optical axis. The derotator rotation is synchronized, but 90 degrees out of phase, with respect to that of the scanner.

Since the telescope has a virtual exit pupil that is located between its secondary and exit lens, the scanner motion causes the return beam to rotate about the optical axis making a conical pattern with a half-angle of the order of a milli-radian at the telescope entrance pupil. The wedge derotator then deflects and translates the return beam in such a manner that its propagation path coincides with the optical axis established by the transmitted beam and extends to the center of the lidar detector.

2.4 Lag angle compensator

The return beam dynamic lag angle changes during the pulse reception time, which is about 160 microseconds. This will be compensated by a two-axis steering LAC mirror. The LAC mirror is driven by the pointing controller in a repeating pattern so that the return beam remains centered on the detector over the duration of the pulse reception. As opposed to the earlier proposed design that uses two active fold mirrors, the single mirror LAC allows certain beam wander at the telescope collecting aperture.

The lag angle compensator will take out the angular boresight error leaving the residual wavefront aberrations only. The fixed errors, such as fabrication errors, system misalignment, and parts and structure distortions, can be compensated by resetting the zero of LAC. The systematic errors, such as the telescope optical distortions and the residual lag due to the derotator, can be compensated by adding control contributions to LAC.

3. SENSITIVITY ANALYSIS

It is easy to design an optical system that can never be built because of its high parametric sensitivity, i.e. very tight fabrication and assembly tolerances. Parametric sensitivity of the telescope has been analyzed to determine its performance for real

fabrication and assembly tolerances. Table 1 lists the wavefront errors induced by tilts and decenters of individual elements. Table 2 lists the boresight errors induced due to all these tolerances. The most sensitive element is the primary mirror. To maintain 1/10 λ rms wavefront and 1 micro-radians boresight system performance, the decenters should be less than 0.01 mm and tilts should be less than 0.01 milli-radians.

4. POLARIZATION

The polarization requirements for a high heterodyne efficiency can be met by using very high efficiency reflective coatings to compensate for the phase shift caused by various coatings (particularly the dichroic beamsplitters), which will produce elliptical polarization. The metal-coated mirrors and transfer optics in the optical system will generally introduce a differential polarization phase change, introducing an ellipticity in the polarization state at the detector. It is important to bear in mind that the coating designs for the mirrors offer very high reflectivity values (>98%). The reflectivity is the average of the p- and s-states. It is obvious, then, that the amplitudes of the two polarization states will not differ by more than a percent. Therefore, the coating design specifications should be aimed at controlling the relative phase of the two polarization components.

Since the polarization problem is deterministic, a solution is feasible, although many specific details of the coatings must wait until the detailed design (including coating design) of all optical elements in the system has been completed. Polarization has been checked for the telescope with gold coated primary and secondary mirrors. Figure 6 shows the polarization mapped onto the pupil space for a circular input beam. Circular polarization is well maintained in this fast compact off-axis telescope.

5. OPTOMECHANICAL DESIGN

Optomechanical design and analysis is a very critical step in the development of an optical system. The objective of a good design is to ensure that the optical elements are mounted securely with minimum distortions. Moreover, the relative position and alignment of the optical elements must be maintained under real operating conditions (shock, vibration, temperature change) to ensure long term stability for a reliable operation. All these design objectives must be achieved within the lidar system constraints of size, weight and cost. Some of the critical optomechanical design issues and concepts for the lidar telescope are addressed in the following sections.

5.1 Material selection considerations

Most space applications require lightweight and extremely stable optics, which must perform reliably under the adverse space environment. The material selection for any optical system is dictated by the optical performance requirements, the environmental conditions under which the system is required to operate, and the cost of fabrication. Most space-based optical systems must maintain alignment under the launch loads and vibrations . Therefore, it is imperative that the microyield limit not be exceeded for the selected material. A high microyield stress is characteristic of a brittle material such as silicon carbide, Zerodur, or quartz. Such materials are often completely amorphous and also usually have a low thermal expansion. However, these materials are not suitable for large off-axis mirrors such as the primary mirror of the telescope due to their high fabrication cost and weight.

The space-based optical systems are also generally subjected to very large temperature excursions during operation in orbit. Therefore, it is highly desirable to make the optics and the associated mounting structure from the same material to minimize the misalignments caused by differential thermal expansions. Therefore, metal mirrors make a good choice for large and off-axis configurations because these can be lightweighted and can be produced economically by employing single-point diamond machining. For metal mirrors, the optical surface, in general, is obtained by diamond machining a thin layer of nickel-phosphorous plated on the substrate material. Therefore, another desirable material property is that the CTE of the substrate material be compatible with the CTE of electroless nickel (8.4 ppm/°F).

5.2 Mirror and structure design

Minimizing the weight and size are important considerations for the lidar telescope to lower the overall cost of the system. A significant reduction in weight can be achieved by using either sandwich or open-back mirrors instead of solid mirrors. A sandwich mirror consists of two faceplates separated by a structured core. An open-back mirror has a single faceplate with a light-weighted core. For both designs, the stiffness of the mirror depends on the thickness of the core, the web thickness, and the shape of the core cells. Once a material is selected for the mirrors, it is an iterative process to select the proper core height, web thickness, and faceplate thickness in order to optimize the weight while maintaining dimensional stability. Triangular core cells provide the most isotropic structural properties, and are also fairly easy to machine. Therefore, an open-back triangular cell design will be used for both the primary and secondary mirrors to optimize their weight and stiffness.

A box type of design will be utilized for the support structure, which provides mounting for the telescope components and the scanner. A common structure will be used to support most of the optical components, so that the resulting system will be compact and stable, and will require a minimum of assembly and alignment. A preliminary layout of the telescope is shown in Figure 7.

6. CONCLUSIONS

The innovative design of the lidar telescope and its associated optical assemblies presented in this paper provides an alternative to more conventional lidar optical designs for the development of a compact and lightweight coherent lidar system that can meet the physical requirements of small satellites. Compared with the earlier designs, the optical system discussed here has a fewer number of optical components and is more robust allowing for a much easier spacecraft accommodation design. However, additional work is required to further optimize the proposed optical design and experimentally evaluate its performance as a coherent lidar subsystem.

This work was supported by NASA Marshall Space Flight Center.

7. REFERENCE

1. R. T. Menzies, "Doppler lidar atmospheric wind sensors: a comparative performance evaluation for global measurement applications from earth orbit," Appl. Opt. 25(15), 2546-2553, August 1986.

2. R. G. Beranek, J. W. Bilbro, D. E. Fitzjarrald, W. D. Jones, V. W. Keller, B. S. Perrine, "Laser atmospheric wind sounder(LAWS)," Proc. SPIE 1062, Laser Applications in Meteorology and Earth and Atmospheric Remote Sensing, 234-248, 1989.

3. Michael J. Kavaya, G. D. Spiers, E. S. Lobl, J. Rothermel, and V. W. Keller, "Direct global measurements of tropospheric winds employing a simplified coherent laser radar using fully scalable technology and technique," Proc. of SPIE International Symposium on Optical Engineering in Aerospace Sensing, Technical Conference on Space Instrumentation and Dual-use Technologies, 2214-31, April 6, 1994.

4. W. E. Jones, D. J. Wilson, W. W. Montgomery, C. Robert, S. C. Kursius, S. Ghoshroy, R. E. Joyce, C. Buczek, Z. S. Karu, G. R. Power, "Final Report: Laser Atmospheric Wind Sounder (LAWS) Phase II," NASA Contract No. NAS8-37590, Lockheed Report No. F320789-II, June 1992.

5. "Definition and preliminary design of the LAWS (Laser Atmospheric Wind Sounder) Phase II Final Report Volume II," NASA Contract No. NAS8-37589, GE Astro Space Division, September 1992.

6. R. G. Frehlich and M. J. Yadlowsky, "Performance of mean-frequency estimators for Doppler radar/lidar," J. Atmospheric and Oceanic Technology 11, October 1994.

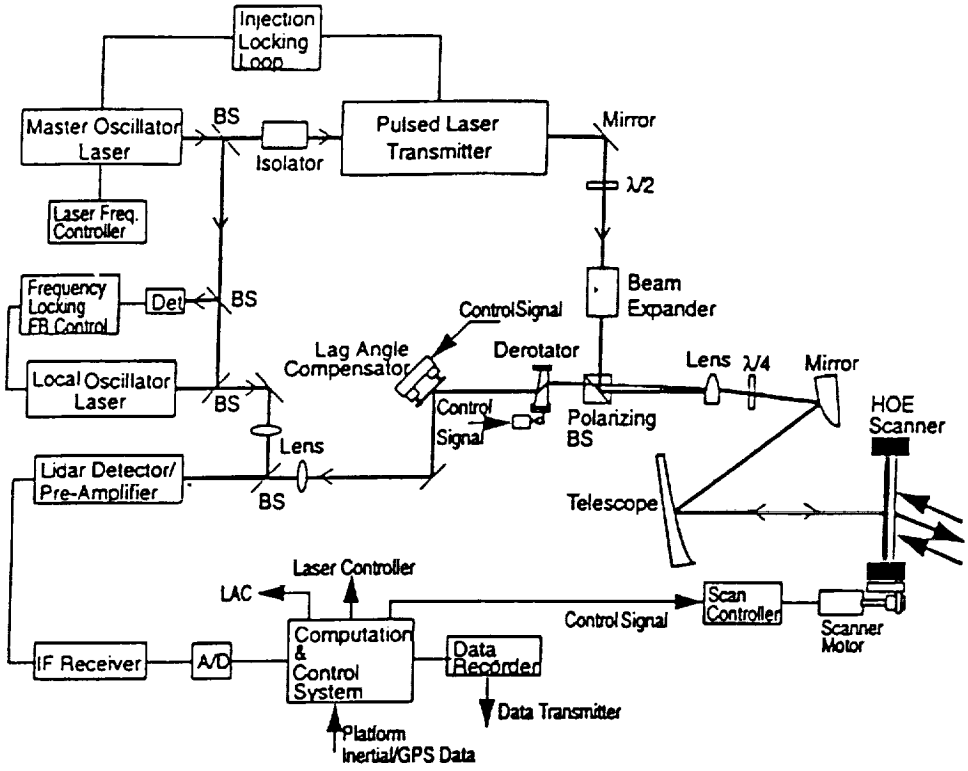

Figure 1 Schematic of a pulsed coherent laser lidar

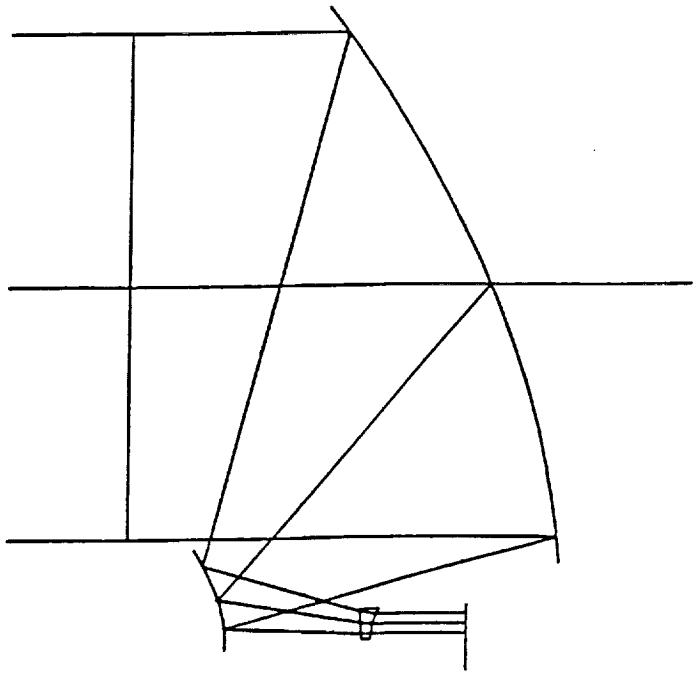

Figure 2 Optical layout of the off-axis telescope

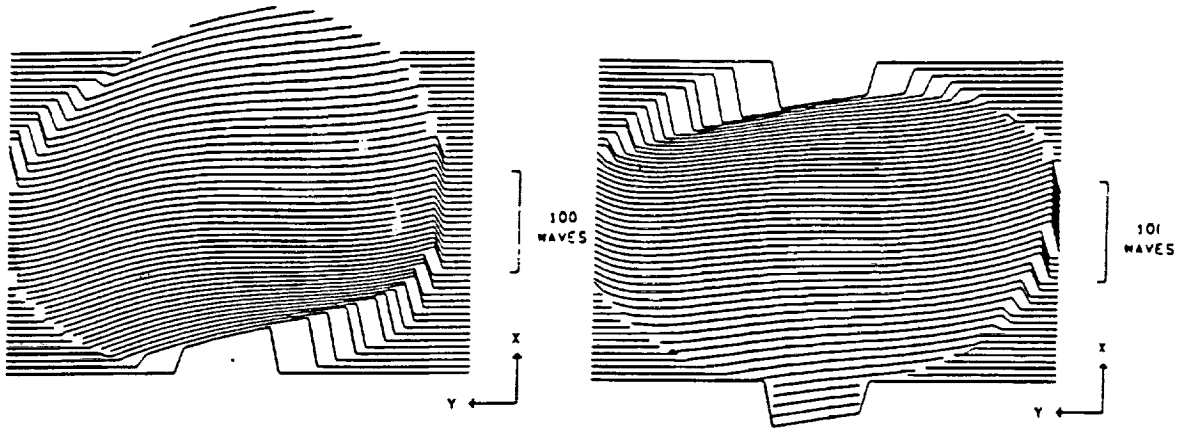

(a) (b)

Figure 3 Wavefront errors for the transmitted(a) and return beams(b)

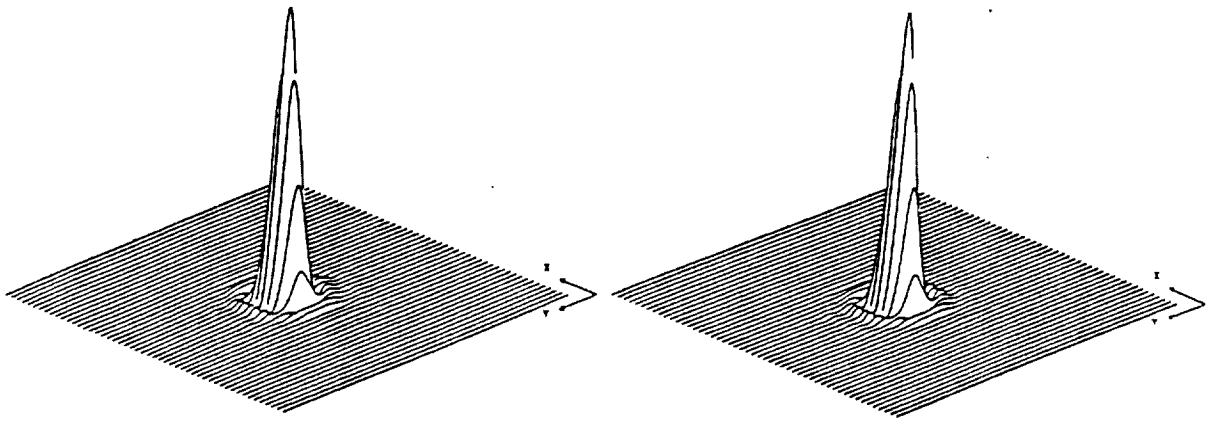

(a) (b)

Figure 4 Point spread functions for the transmitted(a) and return beams(b)

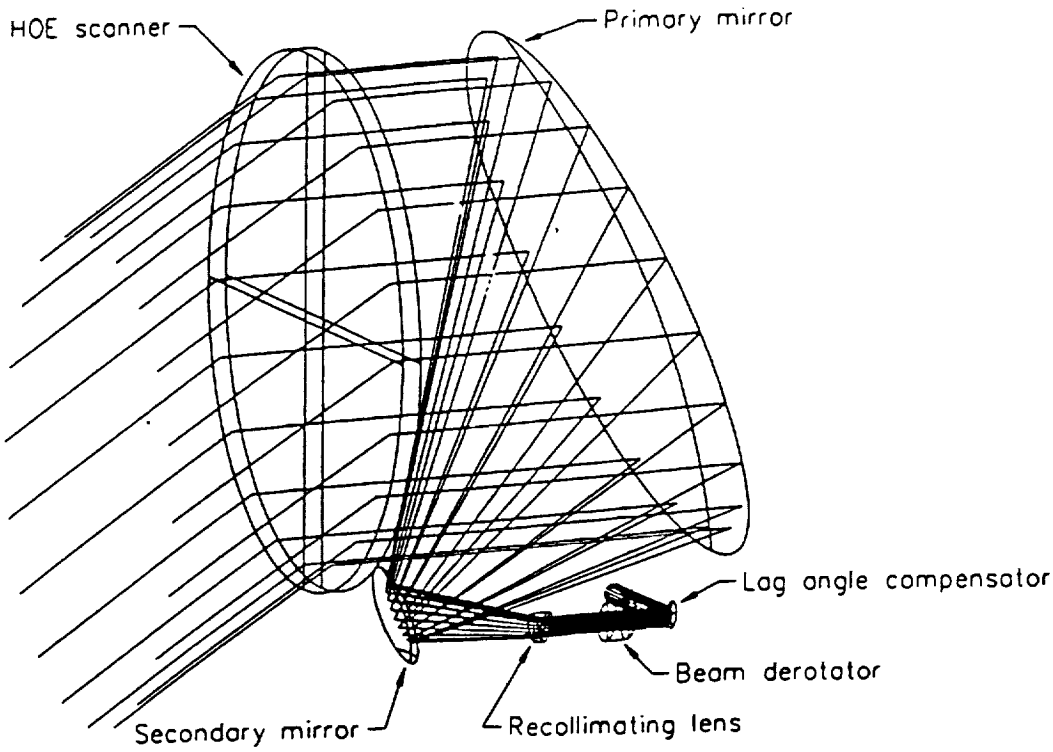

Figure 5 The layout of the optical system for the lidar

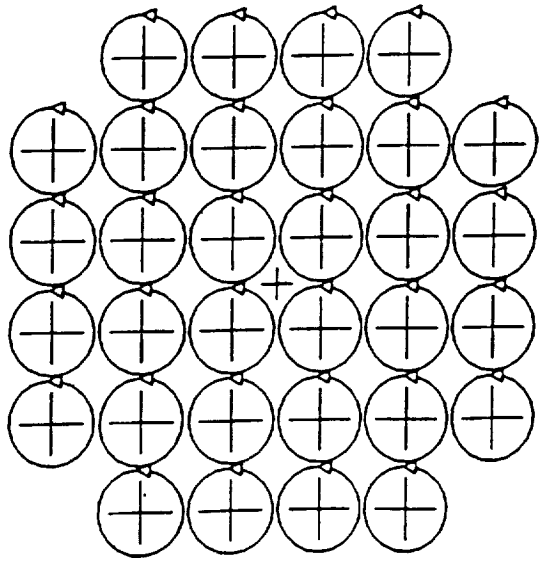

Figure 6 The polarization mapped onto the pupil space

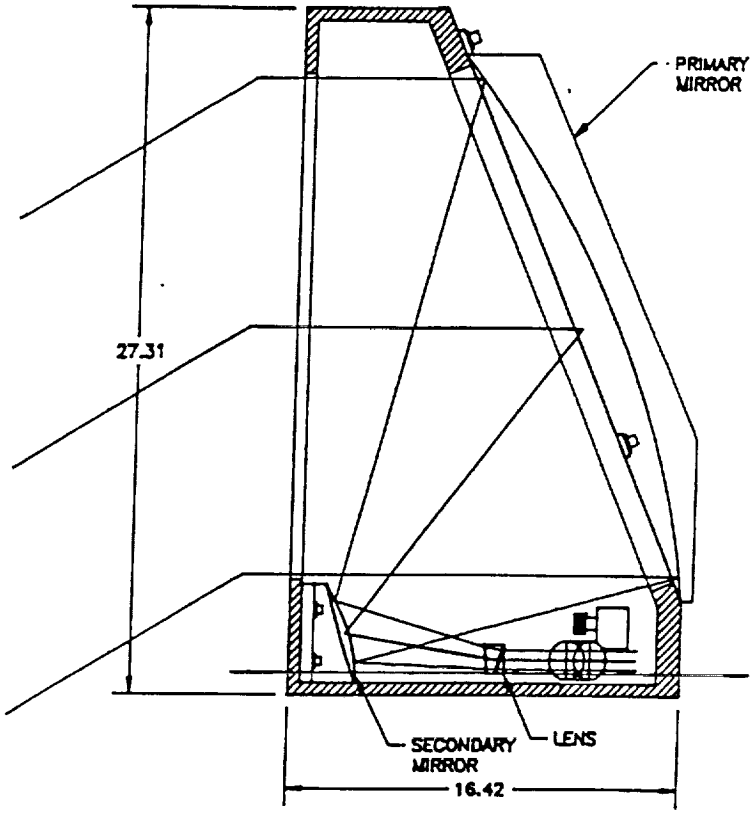

Figure 7 The telescope assembly showing the mirrors, lens and the support structure

Table 1. The telescope wavefront sensitivity

Element	Parameter	Diviation	RMS error
Primary mirror	X decenter	0.01	0.11
	Y decenter	0.01	0.15
	Z decenter	0.01	0.14
	X tilt	0.01	0.04
	Y tilt	0.01	0.04
	Z tilt	0.01	0.03
Secondary mirror	X decenter	0.01	0.10
	Y decenter	0.01	0.14
	Z decenter	0.01	0.16
	X tilt	0.01	0.07
	Y tilt	0.10	0.04
	Z tilt	0.10	0.04
Collimating lens	X decenter	0.10	0.01
	Y decenter	0.10	0.01
	Z decenter	0.10	0.08
	X tilt	1.00	-
	Y tilt	1.00	0.01
	Z tilt	1.00	-

Units: mm for decenter, mrad for tilt, λ for wavefront error.

Table 2. The telescope boresight sensitivity

Element	Parameter	Diviation	Error
Primary mirror	X decenter	0.01	0.10
	Y decenter	0.01	0.01
	Z decenter	0.01	0.13
	X tilt	0.01	0.05
	Y tilt	0.01	0.04
	Z tilt	0.01	0.04
Secondary mirror	X decenter	0.01	0.10
	Y decenter	0.01	0.01
	Z decenter	0.01	0.13
	X tilt	0.01	0.06
	Y tilt	0.10	0.05
	Z tilt	0.10	0.04
Collimating lens	X decenter	0.10	0.01
	Y decenter	0.10	0.01
	Z decenter	0.10	0.02
	X tilt	1.00	0.01
	Y tilt	1.00	0.01
	Z tilt	1.00	

Units: mm for decenter, mrad for tilt, μrad for boresight error

Characterization of Semiconductor Detectors For Operation in 2-micron Coherent Lidars

Farzin Amzajerdian
The University Of Alabama in Huntsville
Center for Applied Optics
Huntsville, Alabama 35899
(205) 895-6030 Ext. 452

Brian F. Jones and Michael J. Kavaya
NASA Marshall Space Flight Center
Electro-Optical Branch
MSFC, Alabama 35812

Abstract

The heterodyne detection characteristics of room-temperature semiconductor detectors operating at 2-micron wavelength region have been investigated. A detector characterization system has been designed and developed to quantify the performance of these detection devices and to provide their optimum operating parameters in a coherent lidar system.

Summary

Most earlier work on optical heterodyne receivers has concentrated on detection devices operating in the 10-micron region[1-4]. In view of the growing interest in eye-safe, solid state coherent laser radars using Thulium and Holmium based lasers, we have investigated the heterodyne detection characteristics of room-temperature semiconductor detectors operating in the 2-micron wavelength region. A detector characterization system has been designed and developed at NASA/MSFC that enables the accurate characterization of 2-micron detection devices for evaluating their performance as heterodyne detectors and determining their optimum operating parameters. The measured quantities will provide all the necessary detector parameters for specifying the optimum optical local oscillator power incident on the detector, the detector optimum bias voltage, and the parameters of the detector interface electronics. The detector characterization system is also capable of direct measurement of the detector heterodyne quantum efficiency η_{HQE} as a function of the IF signal frequency. In a coherent lidar, the signal-to-noise ratio is directly proportional to the detector heterodyne quantum efficiency, therefore knowledge of the detector heterodyne quantum efficiency is necessary for initial calibration of coherent lidars and predicting their performance.

The detector characterization set-up and measurement technique are illustrated in figures 1 and 2. The measurement system uses two diode-pumped, single mode, continuous wave, Tm, Ho:YLF (Thulium, Holmium:YLF) lasers developed by Coherent Technologies, Inc. Both lasers can be

tuned using an intra-cavity etalon over a wide range of about 22 nm or 1500 GHz centered at 2060 nm. The frequency of one of the lasers can be further controlled by adjusting its resonator length using a piezoelectric (PZT) translation stage. This laser can be continuously tuned over a frequency range of about 1 GHz by applying the appropriate voltage to the PZT stage. Both lasers can produce about 100 mW of single frequency power.

The detector measurement system as shown in figure 1, can operate the detector in both direct and heterodyne detection modes. When operating in the direct detection mode, the output of the continuously tunable laser is focused by a short focal length lens (~25 mm) to a spot size considerably smaller than the detector effective area to avoid introducing any truncation error in the measurements. The detector output is then amplified by an electronic receiver and recorded by the signal processing instrument. The electronic receiver performs three functions: amplifying detector signal output current, interfacing the detector and the measurement/recording instrument, and providing bias voltage to the detector. The receiver is capable of operating in either DC or AC-coupled mode using a manual switch and an in-line relay (figure 2). Both amplifiers operate in current-mode (transimpedance) and have input impedances that are much smaller than the typical shunt resistance of semiconductor detectors operating at the 2-micron wavelength. For the direct detection measurements, the receiver is set to operate in the DC-coupled mode. By relating the optical power incident on the detector to the measured receiver output voltage, the detector DC Quantum Efficiency η_{DC}, nonlinearity, and I-V family of curves are obtained. The InAs detectors are used to monitor the power of each laser during the measurement procedures.

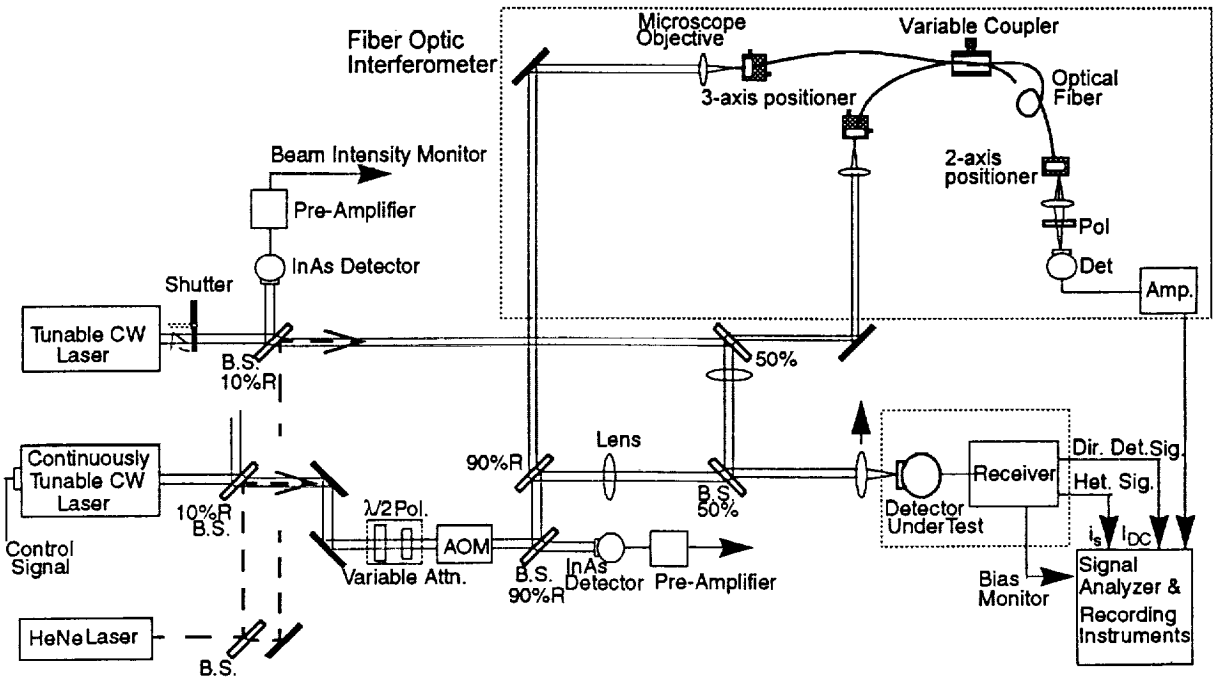

Figure 1. Detector Measurement System.

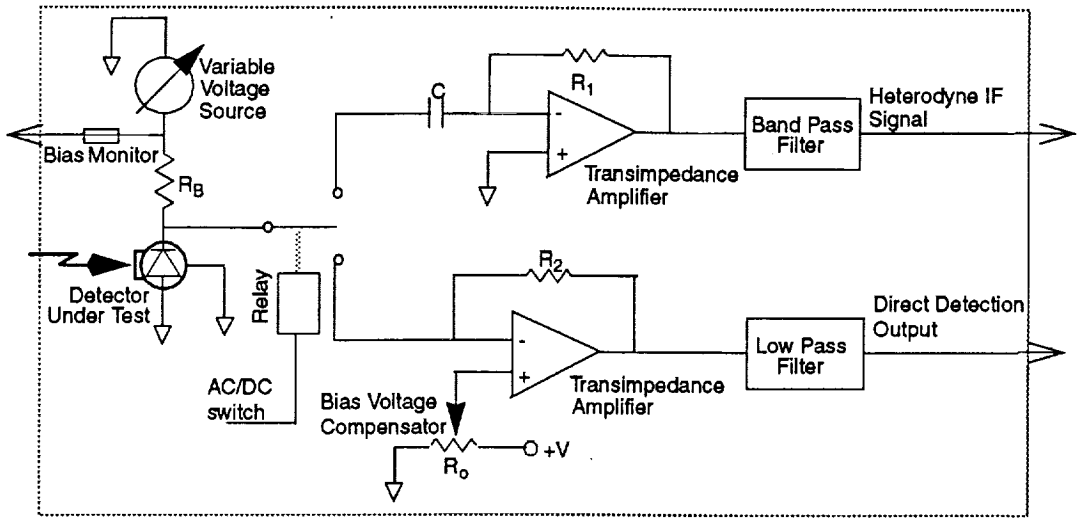

Figure 2. Electronic Receiver Design.

For the heterodyne detection measurements, the short focal lens immediately in front of the detector is removed from the optical path. Initially, the detector DC output currents corresponding to each laser beam are measured individually. Then the receiver is switched to the AC-coupled amplifier and both laser beams are allowed to illuminate the detector. The two laser beams are combined and directed toward the detector by a 50% beamsplitter. The detector generates a current that has three components, two DC components corresponding to each individual beam and an AC component at the difference frequency between the two lasers. The AC component of the detector output is separated and amplified by the receiver to be measured. The detector's heterodyne quantum efficiency can simply be obtained by using the measured detector currents in the expression below

$$\eta_{HQE}(f) = \frac{\overline{i_{AC}^2(f)}}{2I_{DC1}I_{DC2}}(\eta_{DC}/F_0)$$

where f is the difference frequency between the two lasers and F_0 is the signal power reduction factor that accounts for any loss of signal power due to imperfect wavefronts matching and optical misalignment. By varying the frequency of the continuously tunable laser, the detector heterodyne quantum efficiency can then be determined as a function of the heterodyne signal IF frequency. The AC-coupled amplifier has a very low input capacitance of less than 0.8 pF and an input resistance of about 60 Ω which together allow the detector heterodyne signal to be measured over the amplifier full bandwidth of about 2 GHz.

Since the beams are focused on the detector by two relatively long focal length (75 cm) lenses, the signal power reduction factor F_0 will be essentially equal to unity. This is because of the fact that each beam has a spot size (~1 mm^2) considerably larger than the detector active area (~10^{-2} mm^2) as well as a very long Rayleigh range of about 70 cm. Consequantly, the heterodyne detection measurements are very insensitive to defocusing or depositioning along the optical path and

tolerant of beam pointing errors and transverse depositioning. Figure 3 shows the signal power reduction factor, derived for the measurement system of figure 1, as a function of the angular and position misalignments. The results of figure 3 indicate that the angular and position misalignment tolerances of the measurement, for which F_0 is greater 0.99, are about 1 mrad and 1 mm, respectively.

In addition to the detector measurements, the design of the detector characterization system allows the evaluation of different optical heterodyne receiver schemes such as the fiber optic interferometer shown in figure 1. Compared with the more conventional technique of mixing the signal and local oscillator beams using beamsplitters, fiber optic heterodyne receivers allow for a less alignment-sensitive design. The other advantage of the fiber optic heterodyne receivers is that their modular design can provide considerable flexibility in positioning the lidar receiver assembly independently from the rest of the lidar system. The detector characterization system is capable of measuring the optical fiber transmission properties and the coherent mixing efficiency of fiber optic couplers.

In this paper, the detector characterization procedure will be described and the results of the measurements on different InGaAs detectors will be discussed and their optimum operating parameters for use as a heterodyne detector will be presented. The preliminary results of the fiber optic heterodyne receiver characterization for operation in a 2-micron coherent lidar will also be reported.

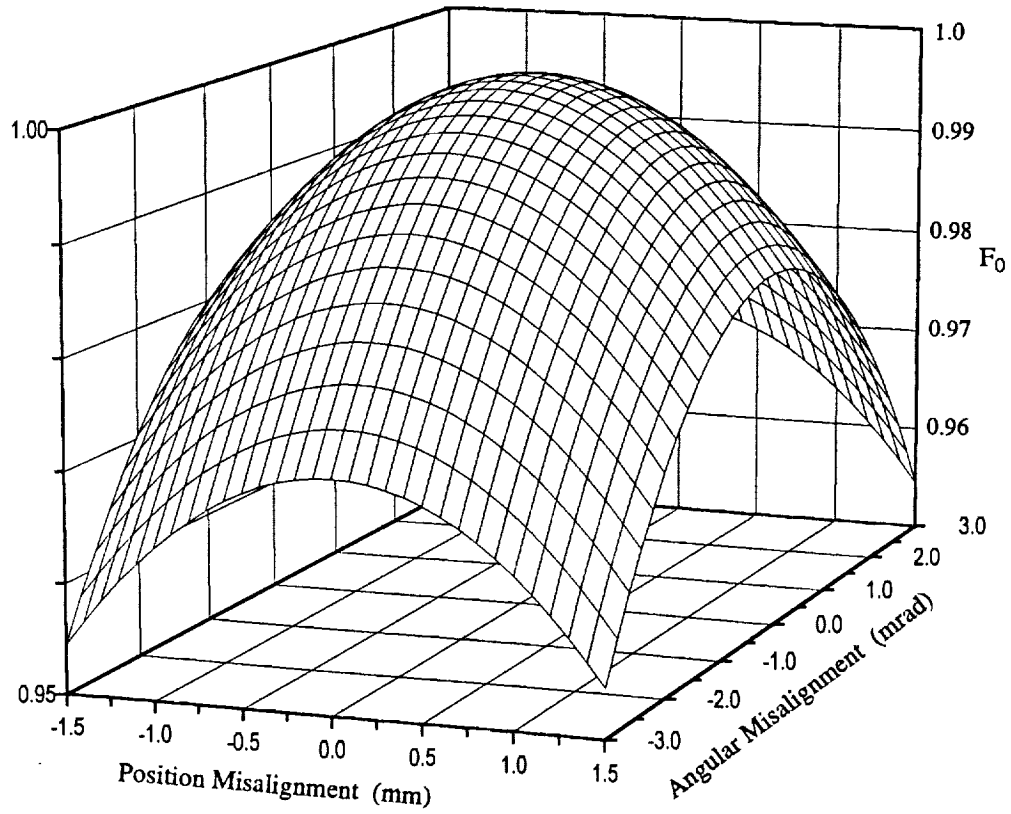

Figure 3. Signal Reduction Factor as a function of position and angular misalignments.

References

1. T. G. Blaney, "Signal-to-noise ratio and other characteristics of heterodyne radiation receivers," Space Science Reviews 17, 1975

2. D. L. Spears, "Long-wavelength photodiode development," NASA report no. NAS-5-25717, August 1983

3. J. M. Hunt, J. F. Holmes, and F. Amzajerdian, "Optimum local oscillator levels for coherent detection using photoconductors," Appl. Opt. 27, August 1988

4. J. F. Holmes and B. J. Rask, "Optimum optical local-oscillator power levels for coherent detection with photodiodes," Appl. Opt. 34, February 1995

Design Considerations for a Receiver for a Space Based Coherent Doppler Lidar Operating in the Two Micron Wavelength Region.

Gary D. Spiers and Farzin Amzajerdian
Center for Applied Optics
University of Alabama in Huntsville
Huntsville, AL 35899
(205) 895 6030

Steve C. Johnson
Electro-Optics Branch, EB54
NASA Marshall Space Flight Center
Huntsville, AL 35812
(205) 544 3478

A space-based coherent Doppler lidar, such as the AEOLUS[1] instrument under investigation at NASA, will probably employ some form of scan geometry and will consequently see an azimuth angle dependent Doppler shift due to components of the spacecraft velocity and earth rotational velocity. The two micron wavelength region currently being considered for this instrument means that this varying Doppler shift will be large. Figure (1) shows this Doppler shift as a function of azimuth angle for an instrument with a 30 deg. nadir angle and a 350 km high orbit.

The dotted lines represent the bandwidth (~1.3 GHz) of commercially available InGaAs detectors. The gross Doppler shift due to the component of the spacecraft velocity can be removed by using a frequency tunable local oscillator. An idealised frequency tuning curve for such a local oscillator is also shown in Figure (1) together with the residual frequency shift seen by the detector - the frequency shift for both positive and negative maximum horizontal wind velocities (± 100 m/s for the case considered here). Also present in the residual frequency shift is the component of the earth's rotation which causes the center frequency to vary as a function of azimuth angle. At each azimuth angle this component due to the earth's rotation varies as a function of the satellite orbit location and is most easily removed electronically using a frequency synthesised local oscillator (Figure (2)). In the example here it has been assumed that the mean frequency of the local oscillator is offset from the frequency of the transmitted pulse by 300 MHz. The use of this offset avoids any ambiguity in the signal. Figure (3) shows the resultant frequencies when no offset between the local oscillator

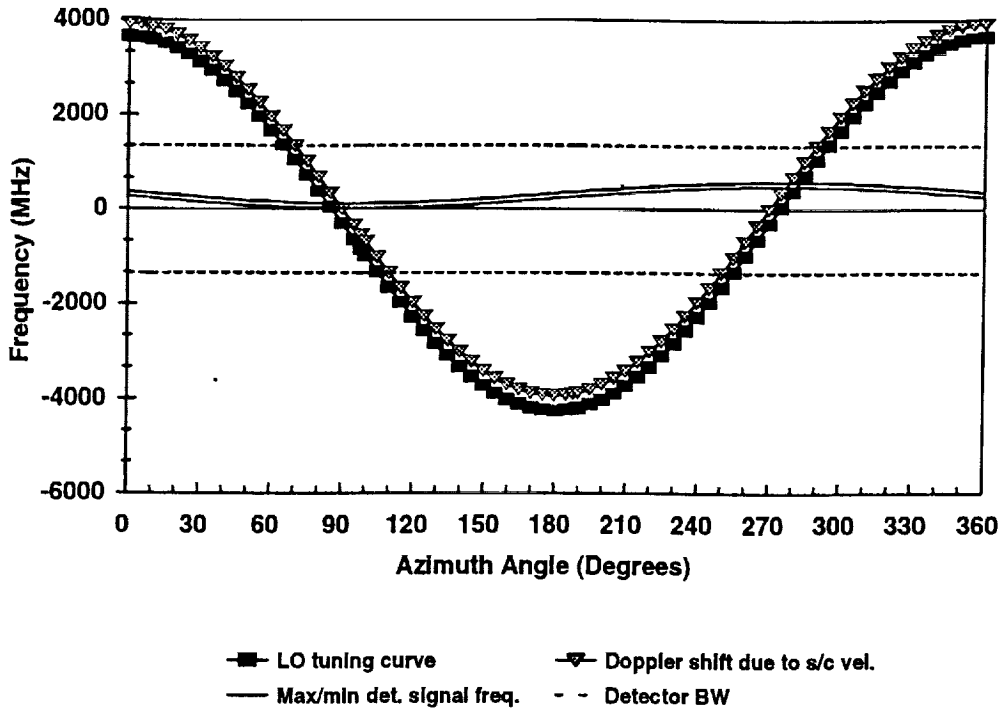

Figure (1) Doppler frequency shifts due to the component of the spacecraft velocity seen by the satellite, typical detector bandwidths, an idealised local oscillator tuning range and the resultant signal bandwidth as a function of telescope azimuth angle.

and transmitter laser exists. The highlighted region between ~170 and ~200 degrees together with a similar region between ~350 and ~380 degrees are areas where a frequency can represent two different wind velocities depending on the sign of the frequency. The sign of the frequency can not be determined from the detected signal and so an ambiguity in determining the wind velocity arises. In principle it may be possible to use contextual information from other neighbouring data points to undertake an educated guess as to the sign of the frequency however this approach would be highly dependent on sampling patterns and local atmospheric conditions and is best avoided.

From Figure (1) it can be seen that after the local oscillator has removed the gross Doppler shift due to the spacecraft's velocity the signal frequency varies from ~14 MHz to ~600 MHz which is within the bandwidth of the detector. The only problem with this scheme is that the local oscillator is now required to tune ±3.95 GHz about a frequency offset 300 MHz from line center of the transmitter frequency. In addition to the tuning requirement, the frequency error in the local oscillator should be less than ~ 1 MHz in order to achieve a velocity measurement accuracy of ~ 1 m/s or less for the whole instrument. This combination of requirements puts severe demands on the local oscillator design and performance. One possible method of relieving these demands is to adjust the local oscillator tuning so that full

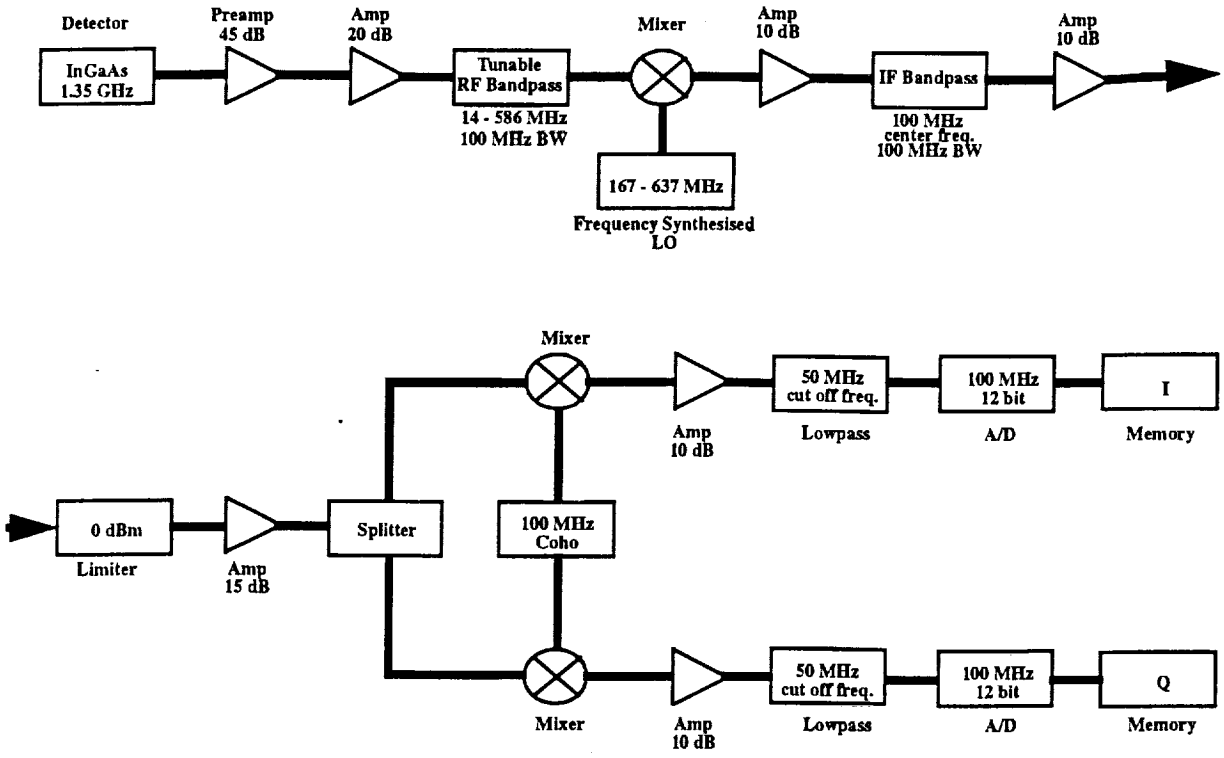

Figure (2) A Representative Receiver design

advantage is taken of the detector bandwidth.

Figure (4) shows the trade-off between local oscillator tuning range and detector bandwidth. Also shown on the figure is the detector shot noise and Johnson noise assuming a detector capacitance of ~ 1 pF and a local oscillator optical power of ~ 1 mW. It can be seen that for detector bandwidths above ~ 250 MHz the detector is no longer shot noise limited, even with full local oscillator tuning to compensate for the satellite velocity component the detector bandwidth remains above this value. This implies that the design presented here, which is the design that has generally been considered for an orbiting 2 μm Doppler lidar is inadequate. This paper will consider various trades and design options to obtain a satisfactory receiver design.

[1] Kavaya,M.J., G.D. Spiers, E.S. Lobl, J. Rothermel and V.W. Keller; "Direct global measurements of tropospheric winds employing a simplified coherent laser radar using fully scalable technology and technique", Proc. SPIE:- Space Instrumentation and Dual-Use Technologies, **2214**, 237 - 249 (1994).

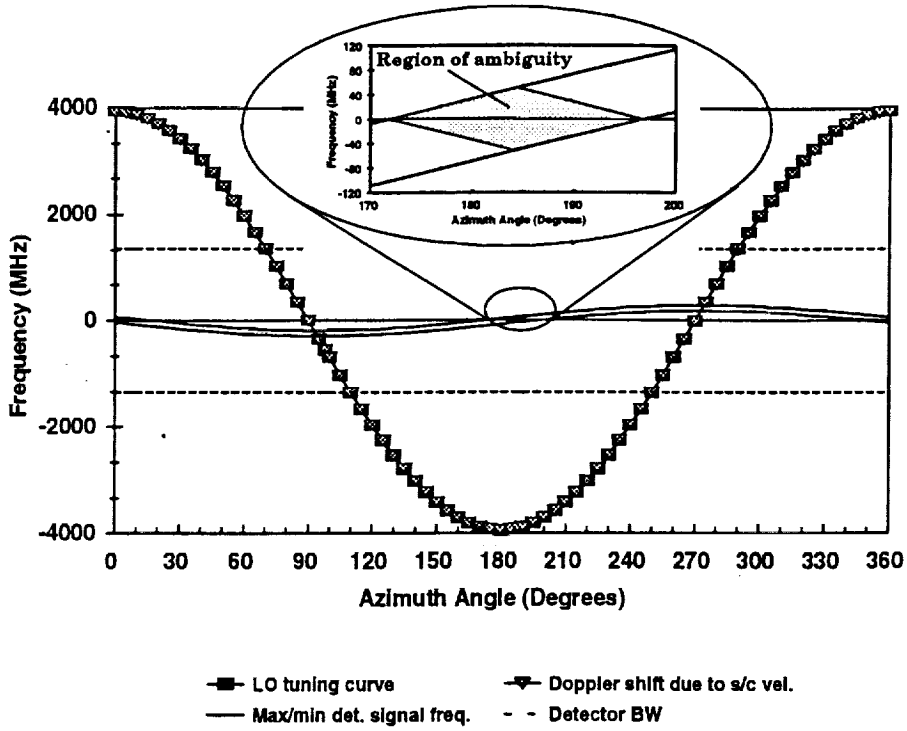

Figure (3) As Figure (1) but without an offset frequency between the local oscillator and transmitter frequencies.

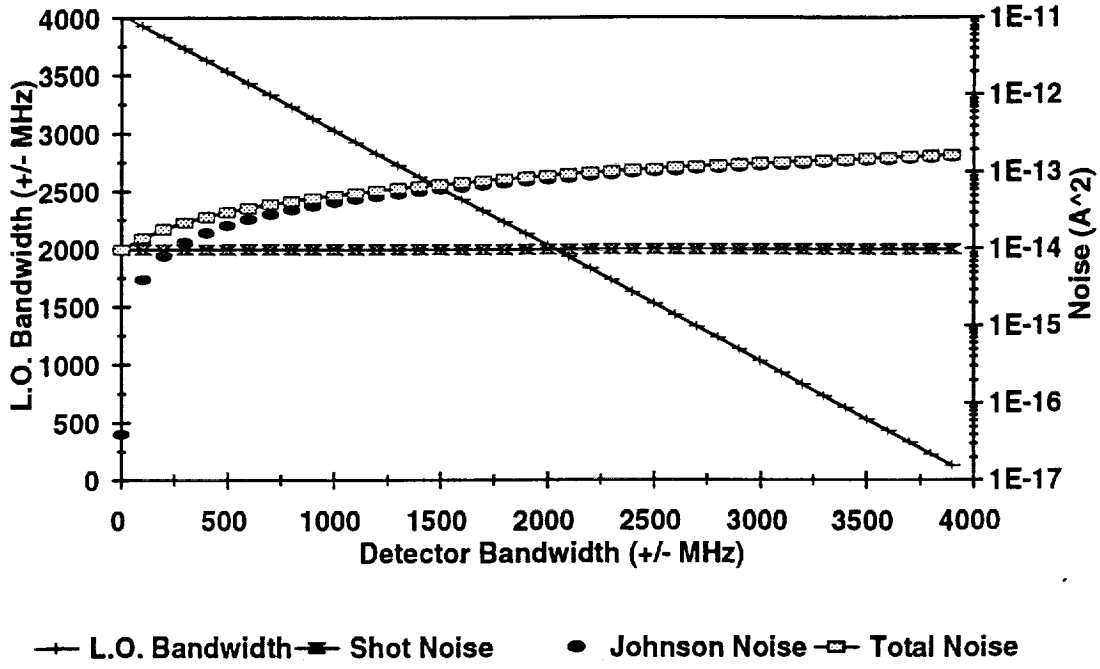

Figure (4) Receiver design trade-offs (see text).

REFERENCES

1. D.L. Spears and R.H. Kingston, "Anomalous noise behavior in wide-bandwidth photodiodes in heterodyne and background-limited operation," Appl. Phys. Lett. 34, May 1979.

2. R. G. Frehlich and M. J. Kavaya, "Coherent laser radar performance for general atmospheric refractive turbulence," Appl. 30, December 1991

3. R.T. Ku and D.L. Spears, "High-sensitivity infrared heterodyne radiometer using a tunable-diode-laser local oscillator," Opt. Lett. 1, September 1977.

4. R. G. Frehlich, "Estimation of the nonlinearity of a photodetector," Appl. Opt. 31, October 1992.

5. J. F. Holmes and B. J. Rask, "Optimum optical local-oscillator power levels for coherent detection with photodiodes," Appl. Opt. 34, February 1995

6. J. M. Hunt, J. F. Holmes, and F. amzajerdian, "Optimum local oscillator levels for coherent detection using photoconductors," Appl. Opt. 27, August 1988

7. Farzin Amzajerdian, "Analysis of measurements for solid state laser remote lidar system," Final Report, Contract No. NAS8-38609/D.O. 77, September 31, 1994

8. M.J. Post and R.E. Cupp, "Optimizing a pulsed Doppler lidar," Appl. Opt. 29, October 1990.

9. H. van de Stadt, "Heterodyne detection at a wavelength of 3.39 μm for astronomical purposes," Astron. and Astrophys. 36, 341-348, 1974.

10. J. J. Morikuni, A. Dharchoudhury, Y. Leblebici, and S. M. Kang, "Improvements to the standard theory for photoreceiver noise," IEEE J. Lightwave Technol., v. 12, July 1994.

11. B. L. Kasper and J. C. Campbell, "Multigigabit-per-second avalanche photodiode lightwave receivers," IEEE J. Lightwave Technol., v. 5, October 1987.

12. R. A. Minasian, "Optimum Design of a4-Gbit/s GaAs MESFET optical preamplifier," IEEE J. Lightwave Technol., v. 5, March 1987.

13. "Definition and Preliminary Design of the LAWS (Laser Atmospheric Wind Sounder) Phase II Final Report Volume II," NASA Contract No. NAS8-37589, GE Astro Space Division, September 1992.

14. "Design Definition of the Laser Atmospheric Wind Sounder (LAWS)", Lockheed Missiles & Space Company, Huntsville, AL, Phase II Final Report, Contract No. NAS8-37590, November 1992. Pages from 3-60 to 3-70.

15. J. Bilbro, G. Fichtl, D. Fitzjarrald, M. Krause, and R. Lee, "Airborne Doppler lidar wind field measurements", Am. Met. Soc. 65, April 1984.

16. M.J. Kavaya, G.D. Spiers, E.S. Lobl, J. Rothermel, and V.W. Keller, "Direct global measurements of tropospheric winds employing a simplified coherent laser radar using fully scalable technology and technique," Proc. Of SPIE International Symposium on Optical Engineering in Aerospace Sensing, Technical Conference on Space Instrumentation and Dual-Use Technologies, 2214-31, Apr 6, 1994.

17. J.G. Hawley, R. Targ, S.W. Henderson, C.P. Hale, M.J. Kavaya, and D. Moerder, "Coherent launch-site atmospheric wind sounder: theory and experiment" Appl. Opt. 32, August 1993.

18. R.T. Menzies, "Doppler lidar atmospheric wind sensor: a comparative performance evaluations for global measurement applications from earth orbit," Appl. Opt. 25, August 1986.

19. W.E. Baker, G.D. Emmitt, P. Robertson, R.M. Atlas, J.E. Molinari, D.A. Bowdle, J. Paegle, R.M. Hardesty, R.T. Menzies, T.N. Krishnamurti, R.A. Brown, M.J. Post, J.R. Anderson, A. C. Lorenc, T.L. Miller, and J. McElroy, "Lidar measured winds from space: An essential component for weather and climate prediction," To be published in the Bulletin of American Meteorological Society, 1995.

20. L. Kristensen and D.H. Lenschow, "The spectral velocity tensor for homogeneous boundary-layer turbulence," Boundary-Layer Meteorology 47, 149-193, Kluwer Academic Publishers, Netherlands, 1989.

21. L. Kristensen and J.E. Gaynor, "Errors in second moments estimated from monostatic Doppler sodar winds. Part I: Theoretical Description," J. Atm and Oceanic Tech. 3, September 1986.

22. L. Kristensen and D.H. Lenschow, "An airborne laser air motion sensing system, Part II: Design criteria and measurement possibilities," J. Atm and Oceanic Tech. 4, 1987.

NASA
National Aeronautical and Space Agency

Report Document Page EM11/Doris W. Hipp

1. Report No.	2. Government Accession No.	3. Recipient's Catalog No.

4. Title and Subtitle

Analysis of Measurements for Solid State Lidar Development

5. Report Due

December 1995

6. Performing Organization Code

University of Alabama in Huntsville

7. Aurthor(s)

Farzin Amzajerdian

8. Performing Organization Report No.

10. Work Unit No.

9. Performing Organization Name and Address

University of Alabama in Huntsville
Huntsville, Alabama 35899

11. Contract or Grant No.

NAS8-38609 D.O. 118

12. Sponsoring Agency Name and Address

National Aeronautics and Space Administration
Washington, D.C. 20546-001
Marshall Space Flight Center, AL 35812

13. Type of report and Period covered

Final - 8/8/94 - 12/7/95

14. Sponsoring Agency Code

15. Supplementary Notes

16.Abstract

17. Key Words (Suggested by Author(s))	18. Distribution Statement

19. Security Class. (of this report)	20. Security Class. (of this page)	21. No. of pages	22. Price
Unclassified	Unclassified		

NASA FORM 1626 OCT 86